UNIVERSIDADE DE SÃO PAULO
INSTITUTO DE FÍSICA DE SÃO CARLOS

Vitor Dantas Meireles

Disorder, low-energy excitations, and topology in the Kitaev spin-liquid

São Carlos

2022

Vitor Dantas Meireles

Disorder, low-energy excitations, and topology in the Kitaev spin-liquid

Dissertation presented to the Graduate Program in Physics at Instituto de Física de São Carlos, Universidade de São Paulo, to obtain the degree of Master of Science.

Concentration area: Basic Physics

Advisor: Prof. Dr. Eric de Castro e Andrade

Corrected version
(Original version available on the Program Unit)

São Carlos
2022

Meireles, Vitor Dantas
Disorder, low-energy excitations, and topology in the Kitaev spin-liquid / Vitor Dantas Meireles; advisor Eric de Castro e Andrade - corrected version -- São Carlos 2022.
111 p.

Dissertation (Master's degree - Graduate Program in Theoretical and Experimental Physics) -- Instituto de Física de São Carlos, Universidade de São Paulo - Brasil , 2022.

1. Frustrated magnetism. 2. Quantum spin liquids. 3. Kitaev model. 4. Griffiths phase. 5. Topological phases. I. Andrade, Eric de Castro e, advisor. II. Title.

ACKNOWLEDGEMENTS

"No man is an island, entire of itself; every man is a piece of the continent, a part of the main..."

– John Donne, *Devotions upon Emergent Occasions, no. 17, 1624.*

No one is truly self-sufficient, everyone must rely on the help and support of others to thrive. Such reflection does not apply only to the collective process of scientific research, but to life as a whole. In this way, I would like to express my deepest gratitude to the people who not only contributed in many ways to the completion of this dissertation, but who also made me feel truly alive, in a dark time when just being alive is a privilege.

That said, I would like to first acknowledge the people in my life who have had the most impact, indirect yet momentous, on my work. Without the trust, understanding, and love provided by my family, none of this would have been possible. I am deeply grateful to my parents, Benedito and Cleide, for letting me make my choices, but even more to have supported them, never leaving me alone. I am especially grateful for the company and understanding of my little sister, Ana Clara. Thank you for always making my day brighter.

My development as a scientist has been influenced by many people, and a special place is deserved to my advisor, Prof. Eric de Castro e Andrade. It has been a great privilege to be advised by him. I am extremely grateful for his guidance, incredible patience, meticulous observations, and for always treating me with trust and respect, both as a scientist and as a person. His ability to provide simple and enlightening explanations will continue to be an inspiration to me. I am also indebted a lot to his countless availability in whatever circumstances, which has greatly helped to mitigate the challenges of remote work.

A special thanks is devoted to my dear friend and colleague, João Augusto. I could never imagine how to get through these tough times without his support and company. I am very grateful for our numerous and stimulating discussions, which provided me with a fresh perspective on many things, both in physics and in life. Also, I feel obligated to give a proper response to *his* acknowledgments, so here it is: *Cheers, to here and our future collaborations in life!*

I am also indebted to the many friends who made my life much more enjoyable, before and during the making of this work. Every one of them has played an important role in my life, in different degrees and circumstances, and each of them knows how important they are to me. Therefore, I think it is fair to just run a Python code to randomly sort all

their names. Here is the array of people who essentially became my second family:

`[Felipe, Juliana, Lettieri, Tabata, Lud, Igor, Pedro, Mari, Vava, Machado, Miguel, Caio, Paulo, Ranier, Deborah, Leandro, Lorena]`

I owe a lot to all of you guys, for assistance and distraction whenever needed. Despite the distance which separates us, the echo of your affect and support have always made my day better. True friendship never fades away with distance.

I want to acknowledge Prof. Luiz Agostinho Ferreira for the inspiring lectures as well as the fruitful discussions after class. Furthermore, I would like to thank Prof. Viktor Dodonov and Prof. José Hoyos for the letters of recommendation, which helped me a lot to continue pursuing my career through my PhD studies. I also want to thank Prof. Matthias Vojta, Prof. José Hoyos, and Prof. Kedar Damle for helpful comments in different stages of this work. Finally, I acknowledge the São Carlos Institute of Physics (IFSC) for funding my studies, through the teaching assistantship program.

Despite the best efforts, there may be many significant people who, due to the rush to the filing deadline, did not get appropriately thanked or acknowledged; I offer my sincere apologies in advance for any omissions or mistakes.

ABSTRACT

MEIRELES, V.D. **Disorder, low-energy excitations, and topology in the Kitaev spin-liquid**. 2022. 111p. Dissertation (Master of Science) - Instituto de Física de São Carlos, Universidade de São Paulo, São Carlos, 2022.

Frustrated magnetism is a very active research topic in condensed matter physics. The competition between different ground states often leads to a suppression of the ordering temperature and opens up the possibility that novel states emerge. One state of particular interest are the spin liquids, for which we find no broken symmetry down to $T \to 0$, where T is the temperature. Moreover, theses states show topological order and are notable for their peculiar features, such as long-range entanglement and the emergence of fractionalized excitations. The Kitaev model is a fascinating example of an exactly solvable model displaying a spin-liquid ground state in two dimensions. In real materials, however, deviations from the original Kitaev model are expected to appear, and we discuss relevant perturbations here. In this work, we investigate the fate of Kitaev's spin-liquid in the presence of disorder – bond defects or vacancies – for an extended version of the model. Considering static flux backgrounds, we observe a power-law divergence in the low-energy limit of the density of states, with a non-universal exponent. We link this power-law distribution of energy scales to weakly coupled droplets inside the bulk, in an uncanny similarity to the Griffiths phase often present in the vicinity of disordered quantum phase transitions. If time-reversal symmetry is broken, we find that power-law singularities are tied to the destruction of the topological phase of the Kitaev model in the presence of bond disorder alone. For weak to moderate site dilution, there is a transition from this topologically trivial phase with power-law singularities to a topologically non-trivial one. Therefore, diluted Kitaev materials are potential candidates to host Kitaev's chiral spin-liquid phase.

Keywords: Frustrated magnetism. Quantum spin liquids. Kitaev model. Griffiths phase. Topological phases.

RESUMO

MEIRELES, V.D. **Desordem, excitações de baixas energias, e topologia no líquido de spin de Kitaev**. 2022. 111p. Dissertação (Mestrado em Ciências) - Instituto de Física de São Carlos, Universidade de São Paulo, São Carlos, 2022.

Magnetismo frustrado é um tópico de pesquisa muito ativo em física da matéria condensada. A competição entre diferentes estados fundamentais muitas vezes leva a uma supressão da temperatura de ordenamento e abre a possibilidade para a emergência de novos estados da matéria. Um estado de particular interesse são os líquidos de spin, para os quais não encontramos quebra de simetria em $T \to 0$, onde T é a temperatura. Além disso, esses estados apresentam ordem topológica e são notáveis por suas características peculiares, como o emaranhamento de longo alcance e o surgimento de excitações fracionalizadas. O modelo Kitaev é um exemplo fascinante de um modelo exatamente solúvel que exibe um estado fundamental de líquido de spin em duas dimensões. Em materiais reais, no entanto, espera-se que surjam desvios do modelo original de Kitaev. Neste trabalho, investigamos o destino do líquido de spin de Kitaev na presença de desordem – defeitos nas ligações ou vacâncias – para uma versão estendida do modelo. Considerando configurações de fluxo estáticas, observamos uma divergência do tipo lei de potência no limite de baixas energias da densidade de estados, com um expoente não universal. Associamos essa distribuição da lei de potência nas escalas de energia à regiões fracamente acopladas dentro do sistema, em uma surpreendente semelhança com a fase de Griffiths, frequentemente encontrada nas redondezas de transições de fase quânticas desordenadas. No caso em que a simetria de reversão temporal é quebrada, descobrimos que as singularidades do tipo lei de potência estão ligadas à destruição da fase topológica do modelo de Kitaev, na presença de desordem nas ligações apenas. Para uma diluição de sítios fraca a moderada, há uma transição desta fase topologicamente trivial com singularidades de lei de potência para uma fase topologicamente não trivial. Portanto, materiais de Kitaev diluídos são potenciais candidatos para hospedar a fase de líquido de spin quiral de Kitaev.

Palavras-Chave: Magnetismo frustrado. Líquidos de spin quânticos. Modelo de Kitaev. Fases de Griffiths. Fases topológicas.

LIST OF FIGURES

LIST OF ABBREVIATIONS AND ACRONYMS

AF	Antiferromagnetic
APBC	Anti-periodic boundary conditions
BZ	Brillouin zone
DOS	Density of states
FM	Ferromagnetic
GUE	Gaussian unitary ensemble
HBZ	Half-Brillouin zone
INS	Inelastic neutron scattering
NMR	Nuclear magnetic resonance
NN	Nearest neighbors
NNN	Next-nearest neighbors
OBC	Open boundary conditions
PBC	Periodic boundary conditions
QSL	Quantum spin liquid
SOC	Spin-orbit coupling
TRS	Time-reversal symmetry

CONTENTS

1 INTRODUCTION

Over the past decades, strong spin-orbit coupling (SOC) has been recognized as a key ingredient to generate unconventional phases in condensed matter systems. In the weakly correlated regime, for instance, it is now recognized that SOC plays a crucial role in the realization of topologically non-trivial phases of matter, with time-reversal symmetric (TRS) topological insulators as one of the most prominent examples.[2,3] Towards the regime of strong electronic correlations, a plethora of novel magnetic phases of matter can arise from the interplay between the Coulomb interaction and SOC, such as spin-nematic orders and quantum spin liquids (QSL).[2,4] The latter was first theorized by Anderson in 1973,[5] and consists of an exotic state of matter described by topological order, which can display peculiar features, such as long-range entanglement and the emergence of fractionalized excitations.[6]

At the forefront of this rapidly growing field is the search, and potential synthesis, of compounds capable of displaying these novel phases of matter. Among a myriad of possibilities, a special class of materials, the $4d$ and $5d$ transition metal compounds, has played a central role in the search for the QSL phase. In these spin-orbital Mott insulators, the combination of both strong spin-orbit coupling and strong electronic interactions generate bond-dependent interactions between the local moments which introduces, or enhances, magnetic frustration, giving rise to novel magnetic properties.[2,7–12] Of primary interest are the so-called Kitaev materials, which are systems hosting dominant Ising-like bond-dependent interactions for local effective moments $j_{\text{eff}} = 1/2$ in stacked honeycomb planes,[4,13–19] making $4d$ and $5d$ compounds strong candidates to the physical realization of the much-celebrated Kitaev's Honeycomb model.

As proposed by Kitaev in 2006,[13] this model consists of a system of spin-1/2 degrees of freedom on the honeycomb lattice, with bond-dependent exchanges. Notably, despite the frustrated nature of the spin interactions, this model admits an exact solution. More specifically, Kitaev exactly established the existence of a quantum spin liquid[6,20,21] of gapless Majorana fermions moving in a static $\mathbb{Z}_2$ flux background. Remarkably, an infinitesimally small external magnetic field can open a gap in the Majorana spectrum, which generates chiral Majorana edge modes with half-quantized thermal Hall conductance.[13,22]

The incredibly rich phenomenology associated with the Kitev model has motivated an intensive search for Kitaev materials in recent years. Two relevant classes of materials showing strong Kitaev interaction are the honeycomb iridates[23,24] $A_2\text{IrO}_3$ ($A = \text{Li}, \text{Na}$) and α-RuCl_3.[25–27] However, these compounds display long-ranged magnetic order at low–T, suggesting the presence of further magnetic interactions beyond Kitaev's.[28,29] Remarkably, in α-RuCl_3, this magnetic state can be suppressed by an external magnetic field.[30–35]

It is replaced by an intermediary phase, sandwiched between the ordered state at low fields and the high-field polarized state, which exhibits a half-quantized thermal Hall conductance,[36,37] as predicted by the pure Kitaev model.

Another relevant Kitaev material is $H_3LiIr_2O_6$.[1] Unlike the Li and Na iridates, this material shows no magnetic order down to 50 mK, making it a prominent candidate to realize the Kitaev spin-liquid phase. However, the experimental observations are at the odds with the thermodynamic behavior of the Kitaev model:[38–40] (i) the specific heat diverges at low temperatures as $C/T \propto T^{-1/2}$, while the pure model predicts $C/T \propto T$; (ii) the uniform magnetic susceptibility shows a similar divergence $\chi \sim T^{-1/2}$, where the expected behavior is a constant at low-T; (iii) the $1/T_1$ NMR spin-relaxation rate has a non-vanishing contribution down to low-temperatures, while the pure model displays an exponential decay with the temperature. These observations indicate the existence of considerable low-energy magnetic excitations. Recent studies suggests they can be understood within Kitaev's model if one takes into account the presence of defects in $H_3LiIr_2O_6$.[41,42]

In this context, our main goal in this work is to expand the current understanding of the effects of disorder in the Kitaev spin liquid phase. This is mainly motivated by the aforementioned $H_3LiIr_2O_6$ phenomenology, where microscopic sources of disorder include stacking faults[43] and the random position of the H ions. Moreover, these motivations can also be applied to diluted α-$RuCl_3$. To study the effects of uncorrelated quenched disorder in this model in a controlled fashion, we address separately the role of bond disorder and site dilution (vacancies). In this investigation, we will be interested in analyzing the disordered model from the perspective of the thermodynamic and dynamical quantities, as well as the interplay between topology and disorder in the presence of an external magnetic field. In this way, we organize this dissertation as follows:

- In Chapter 2 we present a review on the foundations and realizations of the Kitaev Honeycomb model. We begin with the model's exact solution, where some basic notation and terminology are introduced. After discussing some key physical features in the pure model, we move to a brief review on the topological features in the presence of an external magnetic field. Next, we discuss the physical mechanism responsible to the realization of the Kitaev model in real materials. In this context, we argue that a realistic description of Kitaev materials should consider extensions to the pure Kitaev exchange. We then finish by introducing an exactly solvable minimal model intended to capture the effects of further spin exchanges.

- Chapter 3 is devoted to establish the methodology implemented to extract the physical quantities in the disordered system, where the exact diagonalization method is utilized. First, we present the calculation of the density of states (DOS), and its

relation to the specific heat. In addition to the thermodynamics, we also calculate the dynamic quantities, within adiabatic approximation. Finally, we show the methods adopted to probe topology in the disordered system. Specifically, we choose the Bott index formula to compute the topological invariant, which is complemented by an analysis on the spectrum statistics to characterize the in-gap zero modes.

- In Chapter 4 we present our results for the extended model in the presence of bond disorder. We show that strong disorder leads to a power-law divergence in the low-energy density of states (DOS). Here, we link this important result with the existence of rare regions in the sample.[44] This key observation allows us to naturally account for this power-law distribution of energy scales in terms of Griffiths-like singularities[45–49] without evoking the presence of random singlets.[50–56] Finally, we discuss the topological properties of the model in the presence of an external magnetic field, where the presence of a robust power-law distribution at low fields is linked to the destruction of the topological phase.

- In Chapter 5 we present the results for the diluted extended model. The power-law behavior in the thermodynamic quantities is discussed again, where the Griffiths-like argument is linked with the presence of unpaired spins. As we shall see, the topological index is robust up to a critical value of dilution, depending on the flux background. We discuss how this scenario suggests that the topological phase could be detected experimentally in diluted samples.

- We conclude in Chapter 6 with a summary of our findings and a brief discussion on possible future directions.

2 THE KITAEV HONEYCOMB MODEL AND ITS EXTENSIONS TO REAL MATERIALS

2.1 The Kitaev honeycomb model

The Kitaev Honeycomb model[13] consists of a system of spin-1/2 degrees of freedom placed at the vertices of a honeycomb lattice, interacting via a Ising-like exchange between the nearest-neighbors (NN). The special feature is that the model is designed to have a *bond-dependent* structure, i.e., the relevant spin component in the exchange between NN sites is determined by the connecting bond orientation. In the honeycomb lattice there are 3 distinct orientations, labeled as $\alpha = (x, y, z)$, as illustrated in Fig.1(a). In this notation, the Kitaev Hamiltonian is written as

$$\mathcal{H}_K = \sum_{\alpha=(x,y,z)} \sum_{\langle ij \rangle} K_\alpha \sigma_i^\alpha \sigma_j^\alpha, \tag{2.1}$$

where K_α is the exchange energy along the α direction, and σ^α are Pauli matrices. Because of this directional dependence, each spin has 3 competing interactions, which cannot be simultaneously minimized in energy. For classical spins, such an *exchange frustration* leads to a massive degenerate ground state,[57] whereas in the quantum version, the ground state is given by a single, highly entangled wave-function, constituting a *quantum spin-liquid*.[6]

Arguably, the most remarkable feature this model presents is the existence of an exact solution. This is due to an extensive number of conserved quantities, as noted by Kitaev.[13] For every plaquette (hexagon) p on the lattice, one can construct the operator W_p, defined as the product of all spins along the plaquette corners, as shown in Fig.1(b). In the honeycomb lattice, the plaquette operator is written as

$$W_p = \sigma_i^x \sigma_2^y \sigma_3^z \sigma_4^x \sigma_5^y \sigma_6^z. \tag{2.2}$$

Using the spin algebra, it is straightforward to show that, for all plaquettes, we have:

$$[W_p, W_{p'}] = 0 \quad \text{and} \quad [\mathcal{H}_K, W_p] = 0 \tag{2.3}$$

Then, we have a set of non-dynamical, commuting operators defined on each plaquette. In addition, the operator W_p is Hermitian and unitary, as can be easily show by using the algebra of Pauli matrices and noting that $\sigma_i^\alpha = (\sigma_i^\alpha)^\dagger = (\sigma_i^\alpha)^{-1}$. So, we have $W_p^2 = \mathbb{1}$, with eigenvalues $w_p = \pm 1$. The idea now is to separate the total Hilbert space $\mathscr{H}$ into disjoint sectors, each of them corresponding to an eigenspace of W_p, which is an invariant subspace of $\mathcal{H}_K$ itself. Thus, we write the total Hilbert space as

$$\mathscr{H} = \bigoplus_{\{w_p\}} \mathscr{H}_{\{w_p\}}, \tag{2.4}$$

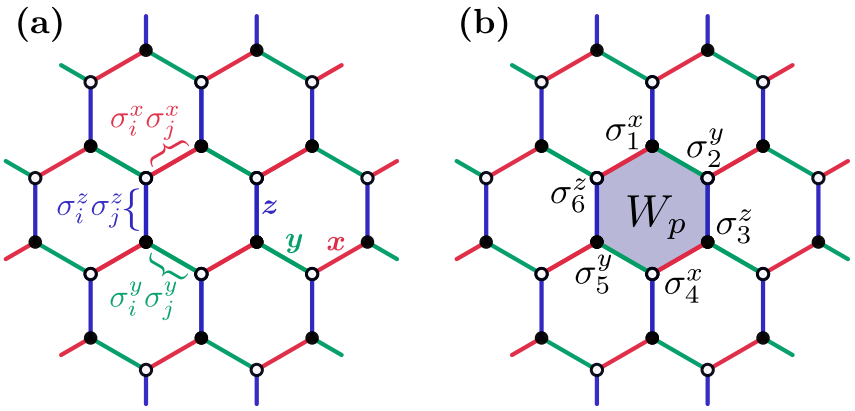

Figure 1 – (a) The Kitaev Honeycomb model. The 3 possible bond orientations are labeled as x, y and z. The spins are coupled according to the corresponding orientation, leading to a highly frustrated spin system. (b) The plaquette operator W_p, defined as the product of spins around a hexagon p.
Source: By the author.

where $\mathscr{H}_{\{w_p\}}$ is the subspace where all plaquettes have the specific set of eigenvalues w_p. This procedure is the same as to block-diagonalizing the Hamiltonian into distinct sectors given by w_p. However, it turns out that this scheme is insufficient to solve the problem. Although the partition of $\mathscr{H}$ had simplified our problem, each eigenspace, $\mathscr{H}_{\{w_p\}}$ is still very large. By taking a lattice with N unit cells, we have $\dim(\mathscr{H}) = 2^{2N}$. Since there are $\sim 2^N$ different flux sectors, we have $\dim(\mathscr{H}_{\{w_p\}}) \sim 2^N$ for each sector. Thus, the Hilbert space still scales exponentially with the system size.

2.1.1 Majorana Fermions and the $\mathbb{Z}_2$ gauge theory

Motivated by the above problem, we now show how to write the spin degrees of freedom in terms of Majorana fermions, following the Kitaev representation.[13] A usual approach when studying spin systems is to use the Abrikosov representation of spins,[58] where a spin operator σ_i^α is written as a combination of two complex fermions, $d_{\uparrow,i}, d_{\uparrow,i}^\dagger$ and $d_{\downarrow,i}, d_{\downarrow,i}^\dagger$, satisfying the usual fermionic algebra: $\{d_{\alpha,i}, d_{\beta,i}^\dagger\} = \delta_{\alpha\beta}$ and $\{d_{\alpha,i}, d_{\beta,i}\} = 0$. Here we take one step further, and define the following Majorana fermion representation:[13]

$$\begin{aligned} b_i^x &= d_{\uparrow,i}^\dagger + d_{\uparrow,i}, & b_i^y &= i\left(d_{\uparrow,i}^\dagger - d_{\uparrow,i}\right) \\ b_i^z &= d_{\downarrow,i}^\dagger + d_{\downarrow,i}, & c_i &= i\left(d_{\downarrow,i}^\dagger - d_{\downarrow,i}\right). \end{aligned} \tag{2.5}$$

Note that c_i and b_i^α can be regarded as the real and imaginary parts of the complex fermions $d_{\alpha,i}$. Therefore, the Majorana fermions obey the reality condition, $(b_i^\alpha)^\dagger = b_i^\alpha$ and $(c_i)^\dagger = c_i$, and satisfies the anticommutation relations

$$\{b_i^\alpha, b_j^\beta\} = 2\delta^{\alpha\beta}\delta_{ij}; \quad \{c_i, c_j\} = 2\delta_{ij}; \quad \{b_i^\alpha, c_j\} = 0. \tag{2.6}$$

Before we write the spins in terms of the Majoranas in (2.5), it is important to take a step back and check the Hilbert space dimensions. In the original spin-1/2 representation,

the local Hilbert space is 2-dimensional. On the other hand, the nominal dimension of a Majorana fermion is $\sqrt{2}$. Therefore, the 4 Majoranas act on an extended Fock space, with dim$=4$. Thus, with the above representation, we are working in an extended space, which contains unphysical degrees of freedom. Keeping this problem in mind, we now represent the spins in terms of Majoranas as

$$\sigma_i^\alpha = i b_i^\alpha c_i \tag{2.7}$$

In order to check the consistency of this representation with the spin algebra, one can write down the anti-commutation relations in terms of the Majorana operators. However, a simpler way is to ask if the operators σ_i^α satisfy the well know identity: $\sigma_i^x \sigma_i^y \sigma_i^z = i$. Using the Majorana algebra, we have

$$\sigma_i^x \sigma_i^y \sigma_i^z = i b_i^x b_i^y b_i^z c_i \tag{2.8}$$

$$= i D_i \neq i, \tag{2.9}$$

where we introduced the operator $D_i \equiv b_i^x b_i^y b_i^z c_i$. It is now clear that in order to fulfill the spin algebra, and to eliminate the spurious degrees of freedom, we need to introduce a constraint for every site i, which defines the *physical* subspace $\mathscr{F}$, equivalent to the original Hilbert space $\mathscr{H}$:

$$\mathscr{H} \simeq \mathscr{F} = \{|\Psi\rangle = D_i |\Psi\rangle \,, \ \forall i\}. \tag{2.10}$$

Now, it is easy to see that D_i acts as an identity on states $|\Psi\rangle$ within the physical subspace, and therefore the operator σ_i^α reproduces the spin algebra when applied to the physical states.

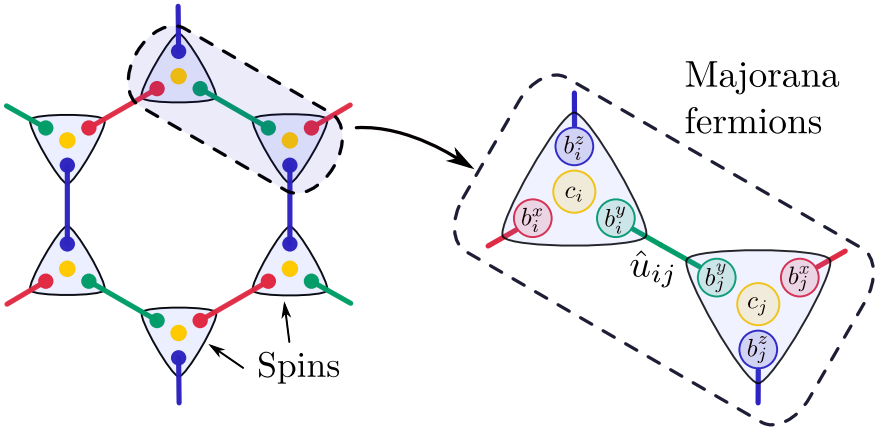

Figure 2 – Majorana representation of spins. The c_i operators (yellow dots) are itinerant Majorana fermions, hopping through the bonds u_{ij} formed by the b_i^α operators (blue, red and green dots).
Source: By the author.

Finally, we can write the Kitaev Hamiltonian in the Majorana representation, keeping in mind that after we obtain the solution, we need to eliminate the redundant

degrees of freedom. By employing the representation (2.5), the Hamiltonian takes the form:

$$\mathcal{H}_K = -\sum_{\langle ij\rangle_\alpha} K_\alpha \left(ib_i^\alpha c_i\right)\left(ib_j^\alpha c_j\right) \tag{2.11}$$

$$= -i\sum_{\langle ij\rangle_\alpha} K_\alpha \hat{u}_{ij} c_i c_j, \tag{2.12}$$

where we have introduced the *bond operators* $\hat{u}_{ij} \equiv ib_i^\alpha b_j^\alpha$. Using the Majorana algebra, it is straightforward to show that

$$\hat{u}_{ij} = -\hat{u}_{ji}; \qquad \hat{u}_{ij}^\dagger = \hat{u}_{ij}; \qquad \hat{u}_{ij}^2 = \mathbb{1}. \tag{2.13}$$

The last of these properties tell us that the eigenvalues of $\hat{u}_{ij}$ are $u_{ij} = \pm 1$. From the Majorana algebra, and the above properties, we can see that the bond variables form a set of integrals of motion: $[\mathcal{H}_K, \hat{u}_{ij}] = 0; \quad [\hat{u}_{ij}, \hat{u}_{kl}] = 0, \ \forall\ i$. Consequently, we can split the extended space into different eigenspaces of $\hat{u}_{ij}$, with each subspace corresponding to a system with a fixed configuration of signs $\{u_{ij}\}$, which can be diagonalized, as $\mathcal{H}_K$ is quadratic in the Majorana fermions. However, the solutions $|\Psi_u\rangle$, obtained for a fixed configuration $\{u_{ij}\}$, might not belong to the physical subspace. Indeed, from $\{D_i, u_{ij}\} = 0$ we can see that D_i has the effect of changing the signs of the three eigenvalues u_{ij} emanating from the site i. Then, the states $|\Psi_u\rangle$ are not necessarily physical, as they might not fulfill the condition $D_i|\Psi_u\rangle = |\Psi_u\rangle$. To eliminate these unphysical states, we define the following projector

$$\mathcal{P} \equiv \prod_i \frac{\mathbb{1} + D_i}{2}. \tag{2.14}$$

Here the product runs over all sites and acting with $\mathcal{P}$ on unphysical states yields zero. From the above discussion, we now see that the variables u_{ij} do not have a direct physical meaning. In fact, the true physical quantities are the plaquette operators, which are written in terms of bond variables as

$$W_p = \prod_{\langle ij\rangle \in \partial p} \hat{u}_{ij} \tag{2.15}$$

$$= \sigma_1^x D_1 \sigma_2^y D_2 \sigma_3^z D_3 \sigma_4^x D_4 \sigma_5^y D_5 \sigma_6^z D_6. \tag{2.16}$$

From $[W_p, D_i] = 0$ and $[\mathcal{H}_K, W_p] = 0$, it is evident that the plaquette operators in the extended space form a set of conserved quantities. We can therefore obtain physical states by just choosing a set of $\{u_{ij}\}$ that obey the condition (2.15), for a given configuration of signs on the plaquettes. From now on, we assume all states to be projected, because we work within fixed W_p sectors.

From this discussion, we can now interpret the solution of the Kitaev model as a $\mathbb{Z}_2$ gauge theory.[13,59] Because different configurations of $\{u_{ij}\}$ can generate the same physical configuration of eigenvalues $\{W_p\}$, one can interpret redundancy in the bond variables as

a $\mathbb{Z}_2$ *gauge theory*. On the other hand, the plaquette operators are recognized as the *fluxes*, which are gauge invariant. From now on, we will use this terminology, where for a given *flux sector*, i.e., a configuration of $\{W_p\}$, one can pick a gauge of $\{u_{ij}\}$, and then proceed to diagonalize the Hamiltonian. As a final remark, we notice that different flux sectors are physically distinct from each other. Consequently, the flux degrees of freedom influence the physical properties of the Kitaev model. Therefore the spins are fractionalized into fluxes and Majoranas.

2.1.2 Ground State and Phase diagram

Now that we have established the basic terminology the Kitaev model, we can proceed with its diagonalization. As discussed above, we have now a theory of itinerant Majorana fermions, hopping in a static bond configuration, described by the Hamiltonian

$$\mathcal{H}_K = -\frac{i}{4}\sum_{\langle ij\rangle} A_{ij} c_i c_j; \qquad A_{ij} = \begin{cases} 2K_\alpha u_{ij} & \text{if } (i,j) \text{ is along } \alpha \\ 0 & \text{otherwise.} \end{cases} \tag{2.17}$$

Here the factor 2 comes from the counting of bonds (i,j) and (j,i). In a generic (periodic) flux sector the Majorana unit cell is enlarged in order to accommodate the periodic gauge configuration $\{u_{ij}\}$. Therefore, for each flux sector we label the honeycomb sites as $(\mathbf{r}_i, \lambda)$, where $\mathbf{r}_i$ is the position of the j-th Majorana unit cell, with $i = 1, \ldots, N$ and $\lambda = 1, \ldots, N_s$ labels the position of a given site within the Majorana unit cell.[60]

To diagonalize the model, we first take the Fourier transform of the Majorana operators:

$$c_{i,\lambda} = \frac{1}{\sqrt{N}}\sum_{\mathbf{k}} e^{i\mathbf{k}\cdot\mathbf{r}_i} c_{\mathbf{k},\lambda}; \quad \lambda = 1, \ldots, N_s \tag{2.18}$$

Note that due to the condition $c^\dagger_{\mathbf{k}',\mu} = c_{-\mathbf{k}',\mu}$, the momentum space operators do not obey the canonical anti-commutation relations: $\{c_{\mathbf{k},\lambda}, c_{\mathbf{k}',\mu}\} = \delta_{\lambda\mu}\delta_{\mathbf{k},-\mathbf{k}'}$. Here we can use a useful trick to avoid this complication. By cutting the Brillouin zone into two halves, and using $c^\dagger_{\mathbf{k}',\mu} = c_{-\mathbf{k}',\mu}$, we can write the expansion as

$$c_{i,\lambda} = \frac{1}{\sqrt{N}}\sum_{\mathbf{k}\in \mathrm{HBZ}} e^{i\mathbf{k}\cdot\mathbf{r}_i} c_{\mathbf{k},\lambda} + e^{-i\mathbf{k}\cdot\mathbf{r}_i} c^\dagger_{\mathbf{k},\lambda}; \quad \lambda = 1, \ldots, N_s \tag{2.19}$$

where HBZ stands for the half of the Brillouin zone, and $-\mathbf{k}$ is defined on the other half. Substituting (2.19) into the Hamiltonian we obtain

$$\mathcal{H}_K = \frac{i}{4}\frac{1}{N}\sum_{\mathbf{k},\mathbf{k}'}\sum_{ij}\sum_{\lambda,\lambda'} A^{\lambda\lambda'}_{ij}\left[c_{\mathbf{k}',\lambda'} e^{i\mathbf{k}'\cdot\mathbf{r}_i} + c^\dagger_{\mathbf{k}',\lambda'} e^{-i\mathbf{k}'\cdot\mathbf{r}_i}\right]\left[c_{\mathbf{k},\lambda} e^{i\mathbf{k}\cdot\mathbf{r}_j} + c^\dagger_{\mathbf{k},\lambda} e^{-i\mathbf{k}\cdot\mathbf{r}_j}\right]. \tag{2.20}$$

Now we recall that A_{ij} depends only on the relative distance between two sites. By introducing $\boldsymbol{\delta} \equiv \mathbf{r}_i - \mathbf{r}_j$, we can write the matrix elements as $A^{\lambda\lambda'}_{\boldsymbol{\delta}}$. Using this notation, we can write the following form of $\mathcal{H}_K$:

$$\mathcal{H}_K = \frac{1}{2}\sum_{\mathbf{k}}\sum_{\lambda,\lambda'} c_{-\mathbf{k},\lambda}\, A^{\lambda\lambda'}(\mathbf{k})\, c_{\mathbf{k},\lambda}, \tag{2.21}$$

where $A^{\lambda\lambda'}(\mathbf{k})$ is the Fourier transform of the matrix A_{ij}, and it is written as

$$A^{\lambda\lambda'}(\mathbf{k}) = i\sum_{\boldsymbol{\delta}} A^{\lambda\lambda'}_{\boldsymbol{\delta}} e^{i\mathbf{k}\cdot\boldsymbol{\delta}}, \qquad A^{\lambda\lambda'}(\mathbf{k}) = \left[A^{\lambda'\lambda}(\mathbf{k})\right]^* \tag{2.22}$$

Then, after establishing a periodic bond configuration, in a given flux sector, we only need to diagonalize the matrix $A^{\lambda\lambda'}(\mathbf{k})$ to find the Majorana band structure.

Now, with this scheme prepared, we can ask which of the infinite possible flux sectors corresponds to the ground state. To solve this, we have to determine the flux configuration that minimizes the ground state energy. In general, one solve this by a direct numerical evaluation of possible realizations.[13] However, for the simplest form of the model discussed so far, a theorem by Lieb[61] states that in a translationally invariant system the ground state is flux free, i.e. $W_p = +1, \ \forall p$, which we refer to as the *0-flux sector.*

Another important observation is that the global ground state energy does not depend on the signs of the exchanges K_α, because any change of sign is compensated by changing the corresponding variables u_{ij} (see Fig. 3 (a)). This is true even if the bond variables u_{ij} are fixed, since the gauge invariant quantities W_p remains frozen after the transformation, and we can return to the original u_{ij} values by a gauge transformation. Therefore it does not matter if the exchanges are ferromagnetic (FM) or antiferromagnetic (AF) for the pure Kitaev Hamiltonian.[13]

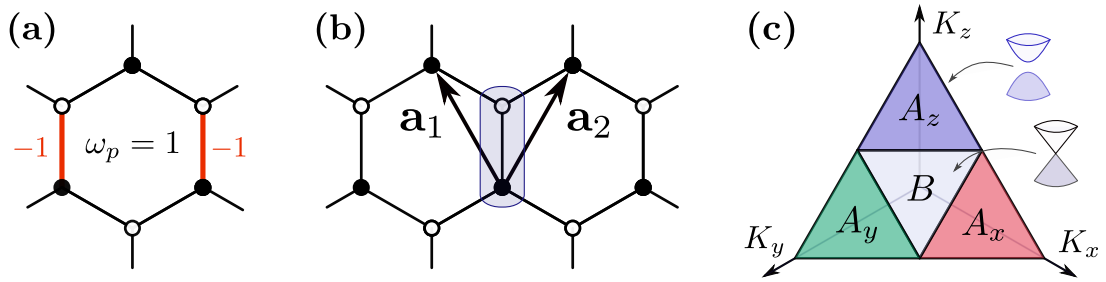

Figure 3 – (a) Invariance of the flux sector under the change of the K_α signal. Here we show the K_z exchange as a representative case. (b) The 0-flux unit-cell, defined by the honeycomb lattice vectors, $\mathbf{a}_1 = (1, \sqrt{3}))/2$ and $\mathbf{a}_2 = (-1, \sqrt{3})/2$. We set the lattice spacing $a = 1$.(c) Phases of Kitaev Model. We can see the existence of 3 gapped phases, and a gapless one. The gap opens as soon as K_α exceeds the sum of the remaining two.
Source: By the author.

Now, we can find the spectrum of Majoranas in the ground state, by just choosing the a gauge where $u_{ij} = +1, \forall \langle i, j\rangle$. This configuration of bonds is periodic, which allows us to use the generic scheme proposed at the beginning of this section. Indeed, the 0-flux sector unit cell is the same as the Honeycomb lattice, and then $N_s = 2$ (sublattice 1 and 2). Now, the calculation is exactly the same as the diagonalization of the tight-biding

model on a Honeycomb lattice,[62] where we have the following elements of $A^{\lambda\lambda'}(\mathbf{k})$:

$$A^{12}(\mathbf{k}) = f(\mathbf{k}) = 2i(K_z + K_x e^{-i\mathbf{k}\cdot\mathbf{a}_1} + K_y e^{-i\mathbf{k}\cdot\mathbf{a}_2} \tag{2.23}$$

$$A^{11}(\mathbf{k}) = 0 \tag{2.24}$$

with $A^{12}(\mathbf{k}) = [A^{21}(\mathbf{k})]^*$, $A^{11}(\mathbf{k}) = A^{12}(\mathbf{k})$. The Hamiltonian, in its matrix form, is written as

$$\mathcal{H} = \frac{1}{2}\sum_{\mathbf{k}} \begin{pmatrix} c_{-\mathbf{k},1} & c_{-\mathbf{k},2} \end{pmatrix} \begin{pmatrix} 0 & f(\mathbf{k}) \\ -f^*(\mathbf{k}) & 0 \end{pmatrix} \begin{pmatrix} c_{\mathbf{k},1} \\ c_{\mathbf{k},2} \end{pmatrix}. \tag{2.25}$$

The Majorana spectrum is finally given by the eigenvalues of this matrix,

$$E(\mathbf{k}) = |f(\mathbf{k})|, \tag{2.26}$$

where $f(\mathbf{k})$ is given by (2.23). By solving $f(\mathbf{k}) = 0$, it can be shown that the spectrum is gapless only if the K_α's are chosen such that the triangular inequality holds:[13]

$$|K_\alpha| \leq |K_\beta| + |K_\gamma|, \tag{2.27}$$

which is valid for any permutation of (α, β, γ). This relation allows us to construct the phase diagram of the model as depicted in Fig.3(c). We can see that there are 3 gapped phases and a gapless one, around the isotropic point $K_x = K_y = K_z$. In the gapless phase B the low energy spectrum is linear, forming Dirac cones at the high symmetry points $\mathbf{K}$ and $\mathbf{K}'$, in the same way as the graphene.[62] Note, however, that we can only have a single Dirac cone if $\mathbf{k} \in$ HBZ, or two halves of the Dirac cones if we are working within the entire BZ. On the other hand, the gapped phases A_α are topologically distinct to the B phase and are equivalent to the toric code model.[13,63] We will not study this limit in this work, as we are going to consider only the isotropic point $K_\alpha = K$, $\forall\alpha$, that is, the center of the B phase.

As the low-energy dispersion of Majoranas follows a graphene-like behavior, it is very tempting to make use of the well-known phenomenology of graphene[62] as an analogy to the ground state of the Kitaev model. However, this approach is rather naive, as we cannot ignore the fractionalized nature of our solution. Indeed, a spin flip creates (or destroys) two fluxes in the adjacent plaquettes, by flipping the bond u_{ij}*, as depicted in Fig.4(b). Therefore, the $\mathbb{Z}_2$ fluxes constitute another type of physical excitation in this system, in the form of a *flux-pair*. This excitation is gapped, with the energy gap Δ_{2f} given by the energy difference of a state with and without the flux pair. As we will discuss in the following chapters, the flux pair gap plays an essential role in the calculation of dynamical quantities in the Kitaev model.[64,65]

* This comes from the fact that any spin σ_j^α anti-commutes with exactly two plaquette operators.

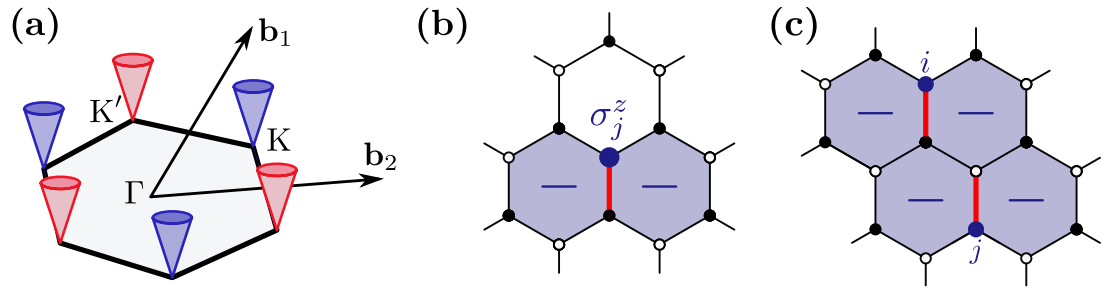

Figure 4 – (a) The Brillouin zone, defined by the reciprocal vectors $\mathbf{b}_1 = \pi(1, \sqrt{3})$ and $\mathbf{b}_2 = \pi(-1, \sqrt{3})$. In the isotropic limit, the low energy bands are given by Dirac cones, situated at the high symmetry points $\mathbf{K}$ and $\mathbf{K}'$. If all the BZ is considered, we can discard the lower band. (b) Creation of a flux pair excitation by applying σ_j^α. (c) Creation of two flux-pair excitations by considering (i, j) beyond NN in the spin-spin correlation function. In this case, the mixing of flux sectors yields a vanishing static correlation.
Source: By the author.

As a final remark, let us discuss briefly the spin correlations in the Kitaev model. To evaluate the static spin-spin correlation, $\left\langle \sigma_i^\alpha \sigma_i^\beta \right\rangle$, we need to act a spin σ_i^β onto the 0-flux ground state. As discussed in the paragraph above, this leads to the creation of a flux pair excitation, leading us to different flux sector. In order to have a non-zero correlation, the application of the second spin must destroy the flux pair previously created, to have a non-zero overlap with the original flux state (see Fig. 4(c) for a case which violates this condition). This is the case only if $\alpha = \beta$ and i is at least a first neighbor of j. Thus, the static correlation reads as[66]

$$\left\langle \sigma_i^\alpha \sigma_j^\beta \right\rangle \propto \delta_{\langle ij \rangle_\alpha} \delta_{\alpha,\beta} \tag{2.28}$$

This ultra short-ranged correlation implies that no magnetic ordering is found in the Kitaev model. This is one of the reasons why the ground state of this system consists of a $\mathbb{Z}_2$ *quantum spin-liquid*.[59,66] In addition, we notice that the Majorana spectrum is gapless, and therefore the ultra short-ranged correlations comes from the presence of the gapped flux excitations, due to the fractionalization.

2.2 Topology in the Kitaev Honeycomb model

2.2.1 Effective Hamiltonian

In this section we consider the presence of a uniform magnetic $\mathbf{h} = (h_x, h_y, h_z)$, which is coupled to the spin degrees of freedom via a Zeeman term

$$\mathcal{H} = \mathcal{H}_K - \sum_j \mathbf{h} \cdot \boldsymbol{\sigma}_j, \tag{2.29}$$

where $\mathcal{H}_K$ is the pure unperturbed Kitaev Hamiltonian. The problem when dealing with such a perturbation is the lost of integrability, as the Zemman term couples the b_i^α and

c_i Majoranas. Consequently, the $\mathbb{Z}_2$ fluxes become dynamical, and we cannot employ the Hilbert space partition scheme presented previously. However, it is possible to treat the magnetic field perturbatively, in such a way that we can use the Majorana representation to write an effective quadratic Hamiltonian, which preserves the exact solution.[13]

To achieve this, we must assume the field magnitude to be smaller than the flux excitation energy, that is $h < \Delta_{2f}$. In this limit, the leading relevant perturbation has the form of a three-spin interaction[13†]:

$$\mathcal{H}_{\text{eff}}^{(3)} \sim \kappa \sum_{\langle\langle i,j,k \rangle\rangle} \sigma_i^x \sigma_j^y \sigma_k^z. \tag{2.30}$$

Here we have introduced the parameter κ, defined as $h_x h_y h_z / \Delta_{2f}$. This contribution explicitly breaks time-reversal symmetry, capturing the essence of the Zeeman term. In addition, we can see the existence of two possible three-spin configurations that are described by the Hamiltonian (2.30), as illustrated in Fig. 5, which we refer to as the (a) and (b) configurations.

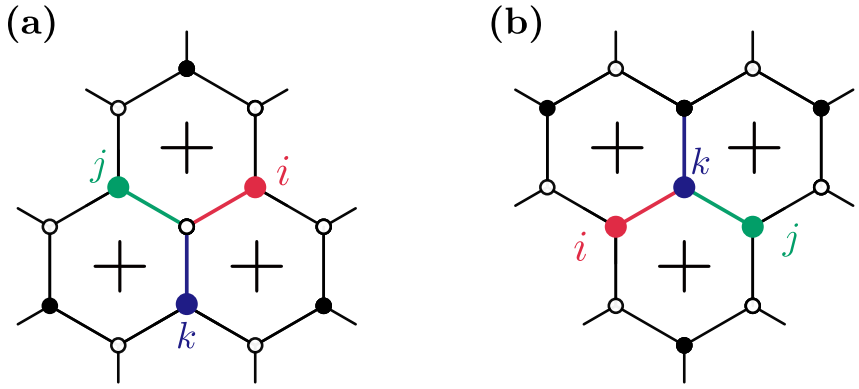

Figure 5 – Representation of the only two possible contributions coming from 3rd order perturbation. (a) In this configuration, the 3 spin interaction gives rise to a quartic fermion term, which is irrelevant. (b) This contribution results in a bilinear next-neighbor fermion interaction, which can be diagonalized.
Source: By the author.

In the Majorana representation (2.7), the three-spin interaction becomes

$$\sigma_i^x \sigma_j^y \sigma_k^z = (i b_i^x c_i) \left(i b_j^y c_j \right) (i b_k^z c_k) \tag{2.31}$$

$$= i b_i^x b_j^y b_k^z c_i c_j c_k. \tag{2.32}$$

Let us focus now on the first configuration, depicted in Fig. 5(a). Here the sites (i, j, k) shares the same neighbor, l. It is possible then to rewrite this contribution in terms of bond operators u_{ij} coming from the site l. Using the definitions of D_i and u_{ij}: $D_i = b_i^x b_i^y b_i^z c_i$ and $\hat{u}_{ij} \equiv i b_i^\alpha b_j^\alpha$, together with the property $b_i^\alpha b_i^\alpha = \mathbb{1}$, the effective Hamiltonian in the

† See the appendix A for a derivation of this effective Hamiltonian.

configuration (a) takes the form:

$$\begin{aligned}\mathcal{H}_{(a)} &\propto i(b_l^x b_l^x)\, b_i^x (b_l^y b_l^y)\, b_j^y (b_l^z b_l^z)\, b_k^z (c_l c_l) c_i c_j c_k \\ &= i D_l \hat{u}_{li} \hat{u}_{lj} c_i c_j c_k c_l \end{aligned} \tag{2.33}$$

This is a 4 fermion interaction, which in principle spoils the integrability of the model. However, this contribution can be ignored because the gapless majorana phase is perturbatively stable with relation to interactions.[67–69]

Now we consider configuration (b). From Fig.5(b) we see that k is a common neighbor of i and j. Thus, we can write this contribution in terms of bond operators coming from the site k. Proceeding with the same steps used in (2.33), the (b) configuration gives the following contribution

$$\mathcal{H}_{(b)} = i D_k \hat{u}_{ik} \hat{u}_{kj} c_i c_j. \tag{2.34}$$

This is a bilinear term describing a next-nearest neighbor (NNN) Majorana hopping, mediated by the bond operators connecting the sites (i, j), as depicted in Fig.6(b). Note that $D_k = \mathbb{1}$ in the physical subspace, so we can ignore this operator in (2.34). Now we have the final form of the Kitaev model in the presence of an external field, described by the effective Hamiltonian:

$$\mathcal{H}_{\text{eff}} = \mathcal{H}_K - i\kappa \sum_{\langle\langle i,j \rangle\rangle} u_{ik} u_{kj} c_i c_j, \tag{2.35}$$

where $\mathcal{H}_K$ is defined in (2.1). From this point, we refer to the effective three-spin interaction as the κ *term* or the κ *interaction*.

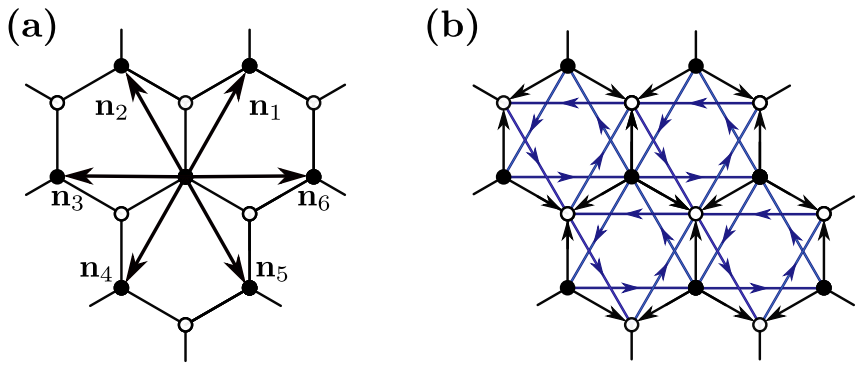

Figure 6 – The six next-nearest neighbors, $\mathbf{n}_i$, $i = 1, 6$, are located at $\pm\mathbf{a}_1$, $\pm\mathbf{a}_2$ and $\pm(\mathbf{a}_1 - \mathbf{a}_2)$. (b) The link orientation of the NN hoppings and the chiral pattern of the NNN hoppings, resembling the Haldane model on the Honeycomb lattice.
Source: By the author.

2.2.2 Topology and Chiral QSL

Now we can explore how the κ term can alter the basic properties of the Kitaev model, as presented in Sec.2.1. First, to ensure that $A_{ij} = -A_{ji}$, we need to establish

an orientation convention for the u_{ij} variables[‡]. Here we impose that u_{ij} is positive if i belongs to the sublattice 1 and j to the sublattice 2(see Fig. 6(b)). As the κ term preserves translation symmetry, the diagonalization follows the same procedure presented in Sec. 2.1.2, where the only difference is the presence of the NNN chiral hoppings, depicted in Fig. 6(b). Now, the matrix elements $A^{\lambda\lambda'}(\mathbf{k})$ are:

$$A^{12}(\mathbf{k}) = f(\mathbf{k}) = 2iK(1 + e^{-i\mathbf{k}\cdot\mathbf{a}_1} + e^{-i\mathbf{k}\cdot\mathbf{a}_2}) \tag{2.36}$$

$$\begin{aligned} A^{11}(\mathbf{k}) = g(\mathbf{k}) &= 2i\kappa\left(1 + e^{i\mathbf{k}\cdot(\mathbf{a}_1-\mathbf{a}_2)} - e^{-i\mathbf{k}\cdot(\mathbf{a}_1-\mathbf{a}_2)} + e^{i\mathbf{k}\cdot\mathbf{a}_2} - e^{-i\mathbf{k}\cdot\mathbf{a}_2} - e^{i\mathbf{k}\cdot\mathbf{a}_1} + e^{-i\mathbf{k}\cdot\mathbf{a}_1}\right) \\ &= 4\kappa\left[\sin(\mathbf{k}\cdot\mathbf{a}_1) - \sin(\mathbf{k}\cdot(\mathbf{a}_1-\mathbf{a}_2)) - \sin(\mathbf{k}\cdot\mathbf{a}_2)\right] \end{aligned} \tag{2.37}$$

with $A^{12}(\mathbf{k}) = [A^{21}(\mathbf{k})]^*$, $A^{11}(\mathbf{k}) = A^{12}(\mathbf{k})$. Now, the Hamiltonian takes the following matrix form:

$$\mathcal{H} = \frac{1}{2}\sum_{\mathbf{k}} \begin{pmatrix} c_{-\mathbf{k},1} & c_{-\mathbf{k},2} \end{pmatrix} \begin{pmatrix} g(\mathbf{k}) & f(\mathbf{k}) \\ -f^*(\mathbf{k}) & -g(\mathbf{k}) \end{pmatrix} \begin{pmatrix} c_{\mathbf{k},1} \\ c_{\mathbf{k},2} \end{pmatrix}. \tag{2.38}$$

Diagonalizing the matrix $A(\mathbf{k})$ in (2.38) yields the following Majorana band structure:

$$E(\mathbf{k}) = \pm\sqrt{|f(\mathbf{k})|^2 + g(\mathbf{k})} \tag{2.39}$$

The Majorana excitations are *gapped* now, with an energy gap given by $\Delta_\kappa = 6\sqrt{3}\kappa$, around the Dirac points $\mathbf{K}$ and $\mathbf{K}'$. Most importantly, however, is the fact that this is a *topological* gap, as we have broken TRS explicitly. Indeed, one shall notice the resemblance of the chiral NNN hopping structure with the Haldane model in the honeycomb lattice, a prototypical model of topological insulators.[70] However, a more careful and generic treatment[71,72] leads us to the conclusion that (2.35) falls into the same topological class as a $p + ip$ topological superconductor,[3,73] where $g(\mathbf{k})$ plays the role of the superconducting gap[§].

Accordingly, it is possible to identify a topological index to our extended model. In a translation invariant system, this index is defined as the *Chern Number*.[74] This quantity corresponds to the following integral over the first Brillouin zone:[3]

$$\mathcal{C} = \frac{1}{4\pi}\int dk_x dk_y \left(\frac{\partial\mathbf{m}}{\partial k_x} \times \frac{\partial\mathbf{m}}{\partial k_y}\right)\cdot\mathbf{m}\,, \tag{2.40}$$

where the vector field $\mathbf{m}(\mathbf{k})$ is defined via $\mathbf{m}(\mathbf{k})\cdot\boldsymbol{\sigma} = -\mathrm{sgn}(iA(\mathbf{k}))$, and $A(\mathbf{k})$ is defined in (2.38). Here we recognize the integrand as the *Berry curvature*[75] of the eigenfunctions of the filled band. From this geometric perspective, it can be shown that $\mathcal{C}$ is indeed an integer,[76] given by the sign of the Majorana gap Δ_κ.[13]

$$\mathcal{C} \equiv \mathrm{sgn}(\Delta_\kappa) = \mathrm{sgn}(\kappa) = \pm 1 \tag{2.41}$$

‡ Although this condition is just a formality for the pure model, for the κ term the sign convention plays an important role, because of its chiral structure.

§ This conclusion is more evident when writing the Kitaev model in terms of complex fermions, which leads to a Bogoliubov-de Gennes form, as presented in Section 3.1.1.

As a consequence, we now expect gapless edge modes to appear in an open system in the presence of $\mathbf{h}$, in a similar fashion to what is observed in the integer quantum Hall effect.[77] These edge modes follow a well-defined chirality, determined by the sign of κ. Moreover, they are expected to be robust in the presence of microscopic details, such as disorder and further perturbations, evidencing the topological nature of 2.35.

However, unlike the quantum Hall effect, these edge modes carry energy, instead of charge. This happens due to the charge-free nature of the Majorana excitations and opens the possibility of a thermal transport measurement. Indeed, these Majorana edge modes can be probed via a *half-integer thermal Hall effect* experiment,[13,36] where the thermal Hall conductivity is given by[13]

$$\frac{k_{xy}}{T} = \frac{1}{2}\left(\frac{\pi k_b^2}{6\hbar}\right) \tag{2.42}$$

The reason to expect a half-integer factor is that a complex fermion is composed of a pair of Majoranas, which means that a single Majorana mode carries half degrees of freedom of a complex fermion. Therefore, this measurement proposal provides a unique signature of the fractionalized nature of the Kitaev spin-liquid.

2.3 Real Materials and Extensions

2.3.1 Microscopic origin of the spin-1/2 Kitaev exchange

The astonishingly rich phenomenology associated with the Kitaev model has sparked very intensive efforts towards its realization in the real world. Much of this interest is motivated by long-standing quests in condensed matter physics, such as the realization of the spin-liquid phase in real materials[6] and the direct probing of its fractionalized nature,[59] as well as the possible experimental observation of Majorana fermions.[78,79] Moreover, there is a strong interest coming from possible applications to quantum computation,[80] as first proposed by Kitaev himself.[13]

The conceptualization of real materials displaying the Kitaev exchange is a challenging task, mainly due to its rather artificial, bond-dependent form. However, some hints were already available at the time Kitaev proposed his model. This form of exchange falls into the family of *compass models*,[8] i.e., models where the coupling between internal spins is directional dependent. These were proposed as minimal models to describe interactions between orbital degrees of freedom in strongly correlated materials, in the pioneering work by Kugel and Khomskii.[81] In this perspective, it is very suggesting that orbital effects and electronic correlations are important ingredients in the realization of the Kitaev exchange. The remaining piece in this puzzle is to consider the effects of relativistic spin-orbit coupling (SOC), as pointed out in the seminal work by Jackeli and Khaliulin.[7,14] In their work, they proposed a physical mechanism responsible for the emergence of the Kitaev exchange in Mott insulators with strong SOC, combined with geometry arguments.

More specifically, they considered $4d^5$ and $5d^5$ transition metal compounds. In these materials, the transition metal ions are surrounded by an octahedral cage of nonmagnetic anions (usually oxygen ions), as depicted in Fig.7. In this configuration, the partially filled d orbital is subject to an effective *crystal field* due to the octahedral environment. Consequently, the 5-fold degeneracy of the d orbital is split into a low-energy triplet, the t_{2g} manifold, and a high-energy doublet, the e_g manifold.[82] While the e_g configuration is empty, the t_{2g}-orbital is occupied by 5 electrons. This partially filled configuration can be viewed as a single hole with an effective orbital angular momentum $l = 1$.[17]

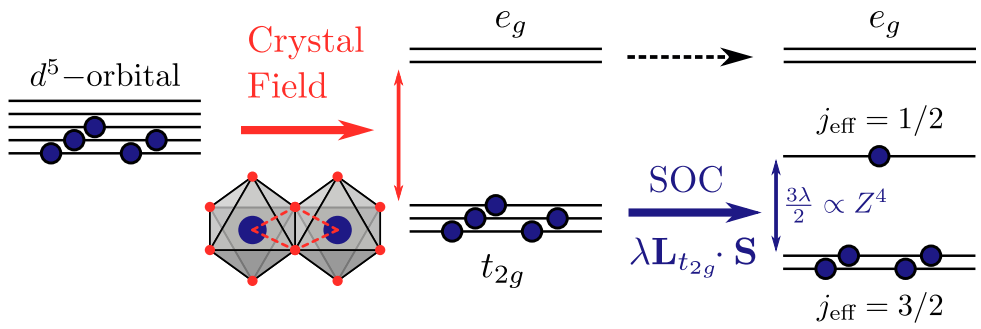

Figure 7 – The splitting of the local d^5 orbitals. The combined effect of the crystal field, spin-orbit coupling and strong electronic correlations leads to the formation of an effective $j = 1/2$ Mott insulator. In the octahedral cage illustration, the red dots at the vertices are nonmagnetic ions, while the large blue dot at the center is the transition metal ion. The dashed lines represents the two exchange paths between the $j_{\text{eff}} = 1/2$ states.
Source: By the author.

Now, we can consider the effects of strong SOC. In this situation, the e_g-orbital remains unaffected, while the effective $l = 1$ angular momentum of the t_{2g}-orbital couples to the spin $s = 1/2$ of the electrons via $\mathcal{H}_{SOC} = \lambda \mathbf{L}_{t_{2g}} \cdot \mathbf{S}$, producing another degeneracy lifting, as depicted in Fig.7. This splitting results into a filled $j_{\text{eff}} = 3/2$ quartet and a high-energy $j_{\text{eff}} = 1/2$ doublet with a single hole. The splitting between these levels is of the order λ. Therefore, if the on-site Coulomb repulsion (Hubbard U) is at least of the order of the bandwidth of the $j_{\text{eff}} = 1/2$ band, the low energy degrees of freedom are the local $j_{\text{eff}} = 1/2$ magnetic moments, which are explicitly given by[17]

$$\left|j_{1/2}\right\rangle = \begin{cases} \frac{1}{\sqrt{3}}\left(-\left|xy,\uparrow\right\rangle - i\left|xz,\downarrow\right\rangle - \left|yz,\downarrow\right\rangle\right), & (m_j = +1/2) \\ \frac{1}{\sqrt{3}}\left(\left|xy,\downarrow\right\rangle + i\left|xz,\uparrow\right\rangle + \left|yz,\uparrow\right\rangle\right), & (m_j = -1/2). \end{cases} \tag{2.43}$$

As the SOC constant λ is proportional to Z,[2] where Z is the atomic number of the ion, the $j_{\text{eff}} = 1/2$ degrees of freedom are expected to be stable for heavy transition metal ions, such as Iridium and Ruthenium atoms.

Because of the spin-orbital nature of the interactions between $j_{\text{eff}} = 1/2$ moments, we expect a highly anisotropic spin exchange. In general, we can write such a generic

exchange in the following form:[17]

$$\mathcal{H} = \sum_{ij} J_{ij}\mathbf{S}_i \cdot \mathbf{S}_j + \mathbf{D}_{ij} \cdot (\mathbf{S}_i \times \mathbf{S}_j) + \mathbf{S}_i \cdot \mathbf{\Gamma}_{ij} \cdot \mathbf{S}_j. \tag{2.44}$$

Here we have the Heisenberg (J_{ij}) and the Dzyaloshinskii-Moriya ($\mathbf{D}_{ij}$) interactions, along with the symmetric $\mathbf{\Gamma}_{ij}$ pseudo-dipolar tensor contribution. In order to have the Kitaev exchange, we need to impose that J_{ij} and $\mathbf{D}_{ij}$ vanishes for every bond, while the only non-zero components in $\mathcal{H}$ are the diagonal elements of $\mathbf{\Gamma}_{ij}$. We are going to focus on the limit where inversion symmetry is not broken, and therefore $\mathbf{D}_{ij} = 0$ always.

It is possible to achieve $J_{ij} = 0$ for a particular geometry, as shown by Jackeli and Khaliullin. If the octahedral cage is displayed in a *edge-sharing* configuration (see Fig. 7), all the leading contributions ($\sim t^2/U$) vanishes, i.e., the Heisenberg and interaction is zero. Moreover, they showed that the only surviving contributions in the next-leading order ($\sim t^2 J_H/U^2$) are the diagonal components of the $\mathbf{\Gamma}_{ij}$ matrix, which is exactly the desired Kitaev exchange. The edge-sharing geometry is essential to achieve result due to the existence of two exchange paths between the $j_{\text{eff}} = 1/2$ states (see Fig.7), which leads to the destructive interference of all leading contributions.

Since the proposal of this mechanism, several theoretical and experimental works were devoted to the search and realization of strong spin-orbit coupled Mott insulators, with the final aim to realize the Kitaev physics. Indeed, in their own work, Jackeli and Khaliullin proposed that honeycomb iridates, such as Na_2IrO_3 and Li_2IrO_3, are candidates to host the Kitaev exchange.[14] In the following years, various compounds were proposed as candidate Kitaev materials, such the Ruthenium-based α-$RuCl_3$[25] and even 3D hyperhoneycomb compounds, such as $\beta{-}Li_2IrO_3$.[83]

2.3.2 Further exchanges and real materials

While the Jackeli-Khaliulin mechanism presents a plausible and elegant way to realize the Kitaev exchange in real materials, a more accurate approach is to consider extensions and deviations to this scenario, to fully describe the phenomenology of Kitaev materials. For instance, we need to take into account the local distortions of the crystal field and also the possibility of a direct $d - d$ hopping between the transition metal ions. Moreover, for heavy $4d$ and $5d$ compounds, the overlap between spatially extended d-orbitals can generate relevant long-range interactions beyond nearest neighbors.[17]

Therefore, to write a realistic spin model, we need to include additional interactions which are allowed by the local symmetries. For the honeycomb lattice, the most generic spin interaction between two sites, i and j, is given by[17,84]

$$\begin{aligned}\mathcal{H}^{\alpha}_{ij} =& J_{ij}\mathbf{S}_i \cdot \mathbf{S}_j + K_{ij}S^{\alpha}_i S^{\alpha}_j + \Gamma_{ij}\left(S^{\gamma}_i S^{\beta}_j + S^{\beta}_i S^{\gamma}_j\right) + \\ &+ \Gamma'_{ij}\left(S^{\alpha}_i S^{\gamma}_j + S^{\alpha}_i S^{\beta}_j + S^{\gamma}_i S^{\alpha}_j + S^{\beta}_i S^{\alpha}_j\right),\end{aligned} \tag{2.45}$$

where $\{\alpha, \beta, \gamma\}$ are permutations of $\{x, y, z\}$. Along with the Kitaev term, we now have the Heisenberg (J) and the off-diagonal interactions (Γ and Γ'). Depending on the context, more simplified versions of this model can be considered, such as the Heisenberg-Kitaev model ($\Gamma = \Gamma' = 0$), as proposed by Chaloupka, Jackeli and Khaliullin in the context of honeycomb Iridates.[15] Another minimal model that can be considered is the $JK\Gamma-$model ($\Gamma' = 0$), in the situation where the distortions of the octahedral cage can be neglected and the Γ' term is small.[84,85]

Regardless of the specific form of the extended model, a generic behavior expected in candidate Kitaev materials is the dominance of the Kitaev exchange against other contributions. Still, the presence of these interactions modify the basic physical properties of the system when compared to the pure Kitaev model. The Heisenberg-Kitaev model is a notorious example, as it presents a very rich phase diagram of magnetically ordered states at sufficiently low temperatures, which was verified by different numerical calculations.[15,16,86,87] Moreover, various Kitaev materials, such as α-$RuCl_3$and Na_2IrO_3, were shown to display magnetic ordering at low temperatures.[88,89] This scenario strongly indicates that extra exchanges work to stabilize these ordered states, which in turn poses a major challenge in the realization of the bare Kitaev model. Notwithstanding, the hunt for the Kitaev spin-liquid is very active, with some promising paths to its realization being proposed over the past few years. One interesting route is to suppress the additional exchange terms by applying an external magnetic field.[32,36,90,91] This approach has gained much attention in the context of α-$RuCl_3$, after the apparent detection of the half-integer quantum Hall effect in this compound under an external field.[32,36] Notice that due to its topological nature, the Kitaev spin liquid is oblivious to further exchanges once it is stabilized.

Another promising approach has been considered very recently, in the context of honeycomb Iridates. The idea is to replace the alkali atoms (Li or Na) with a lighter one, with the aim to enhance magnetic disorder in the material, making Hydrogen-based Iridates natural candidates.[4] This proposal was brought to reality after Kitagawa and colleagues successfully synthesized the honeycomb Iridate $H_3LiIr_2O_6$.[1] This material is notorious due to the total absence of magnetic ordering up to 50mK, making this a very promising spin-liquid candidate. However, its basic properties are at odds with the thermodynamic behavior of the clean Kitaev model:[38–40] (i) the specific heat diverges at low$-T$ as $C/T \propto T^{-1/2}$; (ii) the uniform magnetic susceptibility shows a similar, albeit milder, divergence $\chi \sim T^{-1/2}$; (iii) the $1/T_1$ NMR spin-relaxation rate has a non-vanishing contribution down to low-temperatures and the Knight shift is almost flat in this region. All these results point to an appreciable amount of low-energy excitations, which is not expected in the pure model.

After the $H_3LiIr_2O_6$ results came out, some attempts were made in order to explain

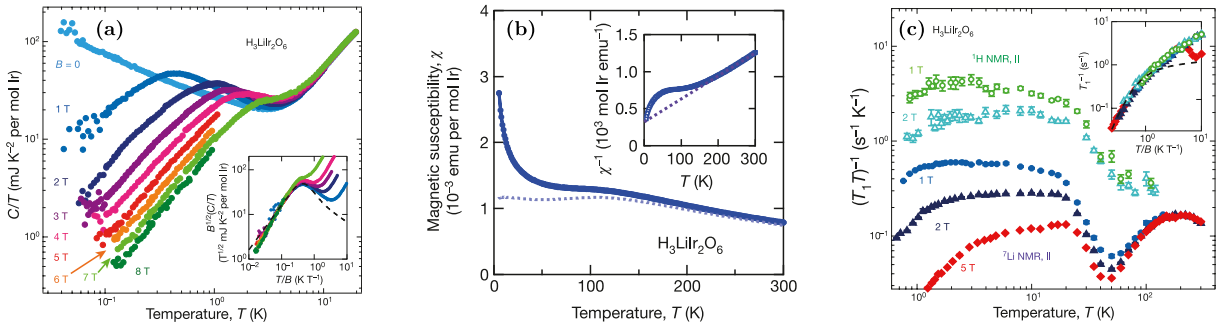

Figure 8 – Experimental data of $H_3LiIr_2O_6$. (a) C/T versus T for various values of the magnetic field. For $B = 0$, the low-T regime is a power-law divergence on the form $T^{-1/2}$. This divergence is suppressed for non-zero values of B. The inset shows the scaling $C/T \sim B^{-3/2}T$, for $T \leqslant B$. (b) The static spin susceptibility, $\chi(T)$. This observable displays similar power-law behavior, $\chi(T) \sim T^{-1/2}$, which is less pronounced in the experimental range.(b) The NMR relaxation rate, $1/(T_1T)$. The almost constant behavior at low-T indicates the presence of low-energy spin excitations.
Source: KITAGAWA *et al.*[1]

its phenomenology[41,42,92,93] and current consensus is that structural disorder plays an important role in this compound, such as stacking faults,[1,93] and the random position of the H atoms.[94] Therefore, a minimal model should consider both the effects of non-Kitaev interactions and structural defects, as we present in the following sections.

2.3.3 Extended Kitaev model

Once the importance of adding extra interactions to the Kitaev model was understood, it became necessary to develop new theoretical and numerical approaches to unveil the physics of Kitaev materials. The reason behind this is due to the loss of integrability in the presence of further exchanges, as the Majorana representation fails to give a quadratic Hamiltonian with static fluxes. On the computational side, a wide range of techniques have provided useful insights on the Kitaev physics beyond the integrable limit, including exact diagonalization,[15,16,95] density matrix renormalization group,[96,97] Tensor Networks,[98,99] Machine learning methods,[100,101] and more prominently, several variations of Monte Carlo methods.[39,102,103]

In this work, we are going to consider a simple approximation based on the Majorana representation. The general idea is to consider the first non-trivial contributions coming from the perturbation expansion of the J, Γ and Γ' interactions, assuming that we do not leave the 0-flux ground state, in the same way as for the magnetic field, in section 2.2. To further simplify our analysis, we can proceed with a more universal scheme, instead of working directly with the non-Kitaev interactions, we seek quadratic Majorana contributions that are consistent with the symmetries of the Kitaev Hamiltonian.[104] Using this procedure, Zhang and colleagues were able to propose the leading time-reversal

symmetric contributions given in terms of a 4-spin interaction,[105]

$$\mathcal{H}_3 = K_3 \sum_{(ijkl)_{\alpha\beta\gamma}} \sigma_i^\alpha \sigma_j^\gamma \sigma_k^\alpha \sigma_l^\gamma + K_3' \sum_{(ijkl)_{\alpha\beta\alpha}} \sigma_i^\alpha \sigma_j^\gamma \sigma_k^\gamma \sigma_l^\alpha, \tag{2.46}$$

where $(ijkl)_{\alpha\beta\gamma}$ and $(ijkl)_{\alpha\beta\alpha}$ are paths consisting of three links (see Figures 9(c) and 37(a)) and (α, β, γ) is a permutation of (xyz) in each term. It is important to stress that TRS breaking contributions are also allowed in this scheme, coming from possible crossed terms between non-kitaev interactions and the magnetic field, for instance.[106] However, our intention in this work is to study the possible effects of the simplest contribution coming from non-Kitaev interactions. Therefore, we will stick ourselves to TR symmetric contributions only. Moreover, we will retain our analysis to a qualitative level, and then, we can choose a single contribution from (2.46), namely the K_3' interaction. The reason to choose this term specifically is due to a more intricate structure of the K_3 term in the language of Majoranas, as we discuss in the appendix B.

Now, by assuming the K_3' as our only perturbation, we can employ the Majorana representation, (2.7), which gives us the following form of $\mathcal{H}_3$:

$$\mathcal{H}_3 = K_3' \sum_{(ijkl)_{\alpha\beta\gamma}} (ib_i^\alpha c_i)(ib_j^\gamma c_j)(ib_k^\gamma c_k)(ib_l^\alpha c_l). \tag{2.47}$$

Now, we use $(b_i^\alpha)^2 = \mathbb{1}$ along with the physical space constraint $D_i = b_i^\alpha b_i^\beta b_i^\gamma c_i = \mathbb{1}$, allowing us to write $\sigma_i^\alpha = ib_i^\alpha c_i = -ib_i^\beta b_i^\gamma$. Using this alternative expression for σ_i^α and the definition of the link operators $\hat{u}_{ij}^\alpha = ib_i^\alpha c_i$, we can finally write the Hamiltonian as a quadratic Majorana interaction,

$$\mathcal{H}_3 = K_3' \sum_{(ijkl)_{\alpha\gamma\alpha}} (ib_i^\alpha c_i)(-ib_j^\alpha b_j^\beta)(-ib_k^\alpha b_k^\beta)(ib_l^\alpha c_l) \tag{2.48}$$

$$= iK_3' \sum_{(ijkl)_{\alpha\gamma\alpha}} (ib_i^\alpha b_j^\alpha)(ib_k^\beta b_j^\beta)(ib_k^\alpha b_l^\alpha) c_i c_l \tag{2.49}$$

$$= iK_3' \sum_{(ijkl)_{\alpha\gamma\alpha}} \hat{u}_{ij}^\alpha \hat{u}_{jk}^\beta \hat{u}_{kl}^\alpha c_i c_l. \tag{2.50}$$

It is possible to see that $\mathcal{H}_3$ gives rise to a third neighbor[¶] Majorana interaction, with the contribution from three consecutive bonds along the path $(ijkl)_{\alpha\beta\alpha}$. In fact, this construction leads to general terms on the form $\mathcal{H}_r$ which contains $r+1$ spin operators and then breaks TRS for even r, while preserving TRS for odd r. In the language of Majoranas, this gives rise to quadratic Hamiltonians with r consecutive bond operators. The κ-term, for instance, is the simplest contribution beyond the Kitaev Hamiltonian, with two bond operators. Accordingly, the next contribution must have a 3-bond structure, making the K_3' term a natural extension in this language.

[¶] Here we use the *Manhattan distance* to calculate the relative positions between two sites.

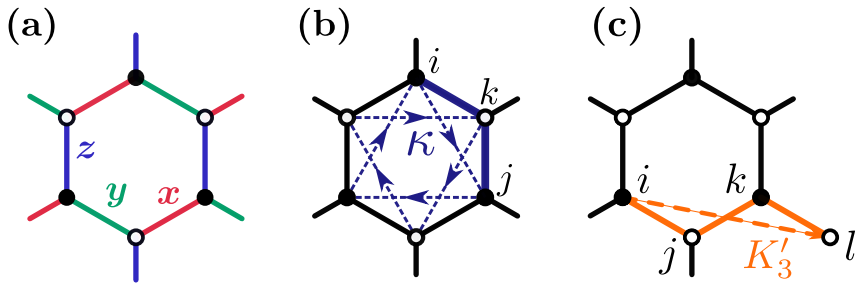

Figure 9 – The 3 terms of the extended Kitaev model. (a) The Kitaev term. (b) The simplest perturbation is the TRS breaking $\kappa-$term, with a 2-bond structure. A representative path is highlighted with its respective sites, (ijk). (c) The K_3' term. This is the natural continuation beyond the κ interaction, due to its 3-bond structure. We highlight a representative $(ijkl)$ path in orange.
Source: By the author.

The full Hamiltonian, including the pure Kitaev term $\mathcal{H}_K$, and the κ term reads as

$$\mathcal{H} = -iK\sum_{\langle ij\rangle} u_{ij}c_ic_j - i\kappa \sum_{\langle\langle i,j\rangle\rangle} u_{ik}u_{kj}c_ic_j + iK_3' \sum_{(ijkl)_{\alpha\beta\gamma}} u_{ij}^{\alpha}u_{kj}^{\beta}u_{kl}^{\alpha}c_ic_l. \tag{2.51}$$

Even in the presence of K_3', the $\mathbb{Z}_2$ bond variables are preserved, and therefore the fluxes are frozen, allowing us to diagonalize (2.51) in the same way presented in the previous sections. However, the K_3' contribution is not completely trivial, as it changes two major characteristics of the system. First, we cannot set the equivalence between the sign of K and u_{ij}, due to the 3-bond structure of K_3'. Therefore, there is a distinction between FM ($K > 0$) and AF ($K < 0$) Kitaev exchanges. In our work, we will be concerned only with AF interactions, for the sake of simplicity. Secondly, in contrast to the pure Kitaev model, where the ground state is the zero-flux configuration due to the Lieb theorem, the presence of K_3' might change the ground state sector.[105] For the K_3' term only, with AF Kitaev exchange, we find that for $K_3' \gtrsim K/8$ the ground state comprises one flux per plaquette, i.e. $W_p = -1$ for all plaquettes (see appendix B), but we do not explore in detail this transition in this work.

3 EXACT DIAGONALIZATION OF THE DISORDERED KITAEV MODEL

As discussed in the previous chapter, the possible realization of the Kitaev quantum spin liquid in real compounds, such as α-$RuCl_3$ and Li_2IrO_3 has attracted a lot of attention from both theoretical and experimental perspectives. Specifically, we are mainly inspired by the recent observations on the hydrogen intercalated iridate $H_3LiIr_2O_6$ and in a smaller degree by doped α-$RuCl_3$*. Much of the enthusiasm to study the physical properties of these materials comes from its intriguing phenomenology, which is caused by the presence of defects (Sec. 2.3.2). Moreover, beyond this specific experimental motivation, there exists a general interest to understand how a QSL responds to different forms of quenched disorder, which can be relevant to other real materials.

Given these motivations, we aim to present in this chapter the general framework in which we work to explore the effects of disorder in the Kitaev quantum spin liquid. Here we describe the numerical procedure to diagonalize the model and extract its physical quantities, with some preliminary results. The main results are shown in Chapters 4 and 5.

3.1 Exact diagonalization

We start from the extended Kitaev model written in terms of Majorana fermions, defined in Eq. (2.51). To study the effects of uncorrelated disorder in this model in a controlled fashion, we address separately the role of two types of defects: *bond disorder* and *site dilution* (vacancies). The first case, of bond randomness, is generically implemented in our model by setting $K \to K_{ij}$, where K_{ij} is a random variable following a given distribution. For the sake of simplicity, we are only concerned with the simple case of *binary bond disorder*, i.e., where $K \to K \pm \delta K$. In the case of site dilution, we remove a randomly distributed concentration of sites, where for each removed site, all of its couplings are turned off. Further details on each case are given in the Chapters 4 and 5.

In all of our calculations, we consider frozen flux configurations, so the problem is exactly solvable regardless of the presence and type of disorder. However, when we put disorder on top of the clean system, translation symmetry is lost, which makes it impossible for us to diagonalize the system in the reciprocal space, as presented in section 2.1.2. Therefore, we diagonalize the model for finite clusters with linear size L (and $N = 2L^2$ sites) with periodic boundary conditions (PBC). We repeat the procedure for several realizations of disorder, where each realization account for a unique $\mathcal{H}$, with a given

* This class of Kitaev materials is more involved because the ground-state is ordered and the putative QSL requires large dilutions and/or fields. Therefore, it is unclear from the outset if our approach is valid.

distribution of couplings or vacancies. Finally, each physical observable is averaged over the disorder realizations.

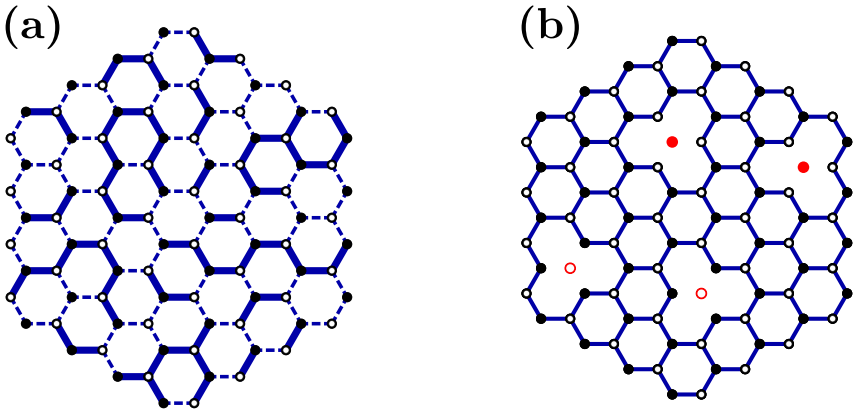

Figure 10 – The two types of disorder which we consider in this work. (a) A realization of binary bond disorder. In this illustration, the strong bonds $(K + \delta K)$ are depicted as the bold solid links, while the weak bonds $(K - \delta K)$ are the thin dashed links. (b) A realization of site dilution. In this figure, the removed sites are depicted as the red dots, where the filled and empty dots refer to different sublattices (A and B).
Source: By the author.

3.1.1 Bogoliubov transformation

To diagonalize the system in real space, for a particular configuration of bond variables u_{ij}, it is useful to rewrite Eq.(2.51) in the following matrix form:

$$\mathcal{H} = \frac{i}{2}\begin{pmatrix} c_A & c_B \end{pmatrix}\begin{pmatrix} F & M \\ -M^T & -D \end{pmatrix}\begin{pmatrix} c_A \\ c_B \end{pmatrix}, \tag{3.1}$$

where $c_{A(B)}$ denote the $N-$component vectors $c_{\mathbf{r},A(B)}$ for a lattice with $N = L^2$ unit cells. The matrix $M_{ij} = Ku_{ij} - K_3' u_{il}^{\alpha} u_{kl}^{\beta} u_{kj}^{\alpha}$ defines the hopping between different sublattices. The hopping in the same sublattice is represented by the matrix elements $F_{ik} = \kappa u_{ij}^{\alpha} u_{kj}^{\beta}$ and $D_{ik} = \kappa u_{ij}^{\alpha} u_{kj}^{\beta}$. Note that we generically have $F \neq D$ due to the sublattice symmetry breaking induced by a generic flux configuration.

Now, we want to bring this Hamiltonian into its canonical form. To accomplish this, we introduce the complex fermion operators d and $d^{\dagger}$, which are related to the Majorana fermions by $d = (c_A + ic_B)/2$ and $d^{\dagger} = (c_A - ic_B)/2$ (Sec. 2.1). In this complex fermion basis, the Hamiltonian assumes the Bogoliubov de-Gennes form[65,107]

$$\mathcal{H} = \frac{1}{2}\begin{pmatrix} d^{\dagger} & d \end{pmatrix}\begin{pmatrix} h & \Delta \\ \Delta^{\dagger} & -h^T \end{pmatrix}\begin{pmatrix} d \\ d^{\dagger} \end{pmatrix}, \tag{3.2}$$

with the $N \times N$ matrices Δ and h defined in terms of M, D, and F as

$$\Delta = (M^T - M) + i(F + D), \tag{3.3}$$

$$h = (M + M^T) + i(F - D). \tag{3.4}$$

To bring the matrix in Eq.(3.2) into its diagonal form, we define the unitary transformation W, which is the matrix representation of the *Bogoliubov transformation.*[107]

$$W \begin{pmatrix} h & \Delta \\ \Delta^\dagger & -h^T \end{pmatrix} W^\dagger = \begin{pmatrix} E & 0 \\ 0 & -E \end{pmatrix}, \tag{3.5}$$

Here E is the $N \times N$ matrix with the positive eigenvalues E_ν stored in descending order. From this construction, it is clear that $W^\dagger$ is the matrix with the eigenvectors ψ_ν stored columnwise as $W^\dagger = \begin{pmatrix} \psi_N & \psi_{N-1} & \dots \psi_1 \end{pmatrix}$. The list of positive eigenvalues $(E_N, \dots, E_1)$ and the matrix $W^\dagger$ consist as our numerical output from the exact diagonalization.

Following the notation used by Blaizot and Ripka in Ref.,[107] we introduce the $N \times N$ Bogoliubov matrices X and Y, corresponding to the occupied and empty states, respectively, so the operator W is written as

$$W = \begin{pmatrix} X^* & Y^* \\ Y & X \end{pmatrix} \qquad W^\dagger = \begin{pmatrix} X^T & Y^\dagger \\ Y^T & X^\dagger \end{pmatrix} \tag{3.6}$$

Now, we can define the Bogoliubov quasiparticle operators f and $f^\dagger$, which are related to d and $d^\dagger$ via

$$d_\nu = \sum_\lambda X^T_{\nu\lambda} f_\lambda + Y^\dagger_{\nu\lambda} f^\dagger_\lambda, \tag{3.7}$$

$$d^\dagger_\nu = \sum_\lambda Y^T_{\nu\lambda} f_\lambda + X^\dagger_{\nu\lambda} f^\dagger_\lambda. \tag{3.8}$$

Here $X_{\nu\lambda}$ and $Y_{\nu\lambda}$ are the Bogoliubov matrices defined in (3.6). In terms of the Bogoliubov quasiparticles, Eq. (3.1) becomes diagonal

$$\mathcal{H} = \sum_\nu \left(f^\dagger_\nu f_\nu - \frac{1}{2} \right) E_\nu. \tag{3.9}$$

Finally, the ground state is defined as the state with no quasiparticle excitations, i.e. $f_\nu |0\rangle = 0$. From this definition, along with (3.9), we define the ground-state energy as $E_0 = -\frac{1}{2} \sum_\nu E_\nu$.

3.1.2 Fluxes

To perform the diagonalization of the complex fermion Hamiltonian in Eq.(3.2), we first need to fix the link variables u_{ij} and work in a well-defined static flux sector, so we can construct the submatrices in Eqs.(3.4) and (3.3).

As discussed in Sec.2.1.2, the flux configuration which minimizes the ground-state energy E_0 is the 0-flux sector, defined as the state where $W_p = +1$ for all hexagons (Fig. 11(a)). However, the situation is more complicated when disorder is introduced in the system, and the 0-flux might not be the most competitive state anymore. Therefore, it

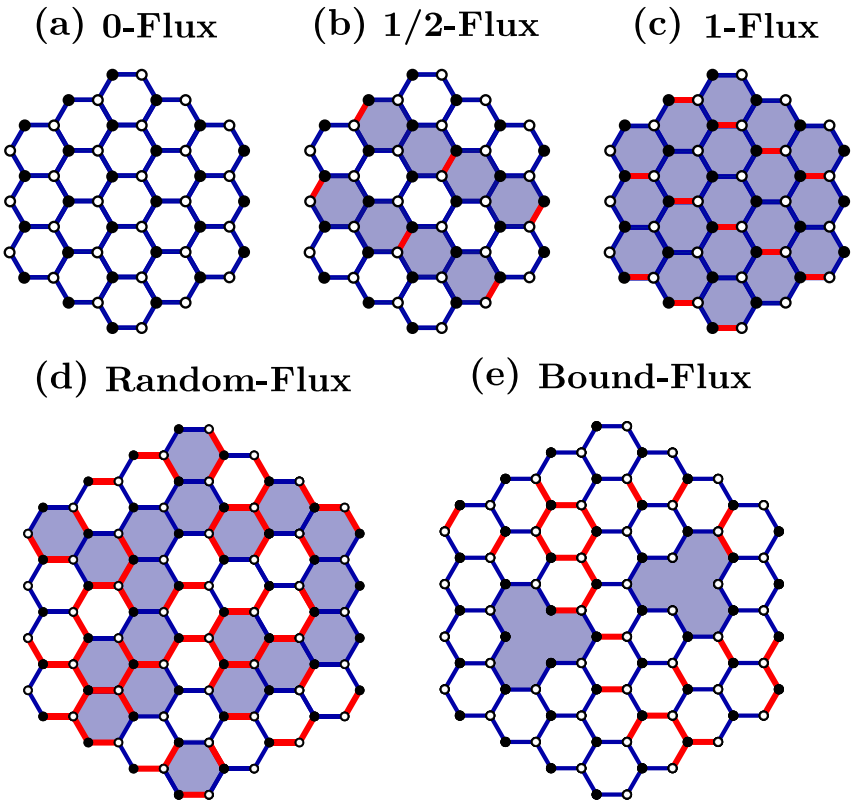

Figure 11 – Flux sectors considered in this work. Red (blue) bonds correspond to $u_{ij} = -1(+1)$, and shaded (white) hexagons correspond to flux $W_p = -1\,(+1)$. (a) 0-flux link configuration, (b) 1/2-flux link configuration, (c) 1-flux link configuration, (d) a random-flux link configuration, and (e) a bound-flux link configuration.
Source: By the author.

is instructive to explore other flux configurations in the presence of disorder. We note, however, that our investigation here has a purely qualitative nature, so we do not exhaust all possible flux configurations. Having this in mind, we pick three representative ordered flux configurations: The 0-flux sector, the 1/2-flux sector, $W_p = +1$ for half of the hexagons and $W_p = -1$ for the other half (Fig. 11(b)), and the 1-flux sector, $W_p = -1$ for all hexagons (Fig. 11(c)). For $K_3' \gtrsim 1/8$ the ground state corresponds to the 1-flux state, in the clean system.[105] The 1/2-flux state is never a competitive ground state in the pristine model for the parameters we use, but it is instructive to study it since it serves as the periodic version of the random-flux state (to be defined in the next paragraph. See Fig. 11(d)). For the parameters we consider in this work, we do not observe a transition in the flux sector as a function of κ. Physically, this suggests we work at weak to moderate fields.

In addition to the ordered sectors, we study the effects of disorder in the flux configuration, by considering the *random-flux* sector (Fig. 11(d)). The idea here is to mimic the effect of thermal fluctuations on the fluxes at low-T, as supported by Monte-Carlo simulations.[39] To numerically construct this state, we randomly assign $u_{ij} = \pm 1$ to each link with equal probability, where in average we have $\langle W_p \rangle = 0$. An interesting

way to explore how the random-flux sector can emerge from the 0-flux, $\langle W_p \rangle = 1$, is to change continuously the probability to flip a bond u_{ij} in the 0-flux sector. By diluting the random-flux in this way, we can graph the average flux $\langle W_p \rangle$ as a function of the bond-flip probability p_{flip}, as in Fig. 12(a). From this exercise, see that $p_{\text{flip}} \approx 0.3$ already generates a random-flux sector, so we can safely set $p_{\text{flip}} = 1/2$ in our calculations, as expected.

Moreover, it is interesting to check how the flux gap evolves as we continuously change $\langle W_p \rangle$ from the 0-flux to the random-flux limit. For this purpose, we calculate Δ_{2f} for several flux realizations with fixed p_{flip}, where $\Delta_{2f} \equiv E_{\text{flipped}} - E_{\text{non-flipped}}$. Specifically, a single z-bond is flipped at a random position. We plot the average value of Δ_{2f} as a function of $\langle W_p \rangle$ in Fig.12(b). It is clear from this analysis that, on average, Δ_{2f} continuously decreases as we decrease the average flux, until we reach the random-flux limit, where $\Delta_{2f} = 0$. This makes sense, since $u_{ij} = \pm 1$ are now random variables, and flipping a single bond modifies $\langle W_p \rangle$ at order $1/N$, which should not change the energy.

Finally, to calculate the physical quantities in the random-flux state, we need to take the average over several random configurations, in the same fashion as we do for bond disorder and vacancies, where each flux realization is static. Therefore, for every observable in the random-flux, we take two independent averages, over the flux configurations, and the disorder realizations.

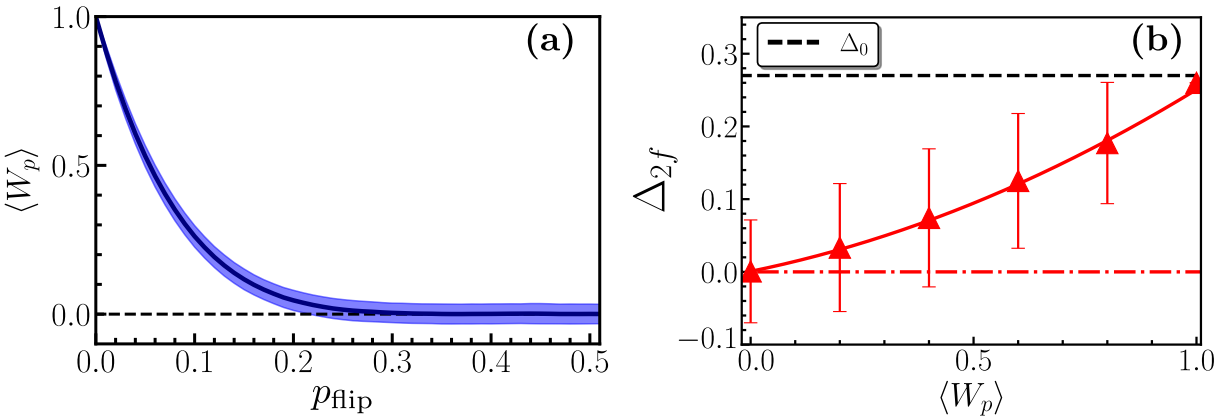

Figure 12 – (a) The flux average $\langle W_p \rangle$ as a function of the bond flip probability p_{flip}. For $p_{\text{flip}} \approx 0.3$ we enter the into the random-flux regime, while $p_{\text{flip}} \to 0$ corresponds to the 0-flux limit. (b) The flux pair gap as a function of $\langle W_p \rangle$. From a quadratic fit (solid line), we observe that the flux gap decreases like $\Delta_{2f} \approx \Delta_0 \langle W_p \rangle (1 + \langle W_p \rangle)/2$ as we approach the random-flux, $\langle W_p \rangle = 0$, where $\Delta_{2f} = 0$ on average. Here Δ_0 stands for the 0-flux limit, $\Delta_0 \approx 0.27$. For both plots we considered the average over ~ 100 realizations of random flux.
Source: By the author.

In the case of vacancies, we consider one additional flux sector, the *bound-flux*. This configuration is motivated by the observation that, for a single impurity, the energy is lowered by nucleating a flux in the extended plaquette formed by the vacancy[108] (See Fig. 13). We can understand this flux binding effect with a very simple argument. Let

us consider a single isolated plaquette as the problem of Majorana fermions hopping on a ring with l sites.[3] The solution for this problem is straightforward, with the following spectrum:

$$E(k_n) = -2K\cos(k_n); \quad k_n = \begin{cases} 2\pi n/l & \text{for PBC} \\ 2\pi(n+1/2)/l & \text{for APBC,} \end{cases} \tag{3.10}$$

where n is an integer, and the allowed wavevectors k_n depend on the boundary conditions. If we consider the 0-flux case, we have the usual periodic boundary conditions (PBC)(See Fig.13(c)). On the other hand, if we pin a flux to the plaquette, we need to flip one bond, $u_{ij} = -1$, which is the same to impose anti-periodic boundary conditions (APBC), as illustrated in Fig.13(b). Finally, we calculate the ground state for each situation, which is simply the sum of the occupied states in the half-filled band depicted in Fig.13(a). For the extended plaquette around a diluted site, we have $l = 12$, and the energy difference between the two cases is readily calculated as $E_{\text{bound}} - E_0 \approx -0.51 < 0$, which shows that a flux indeed lowers the energy of a single plaquette.

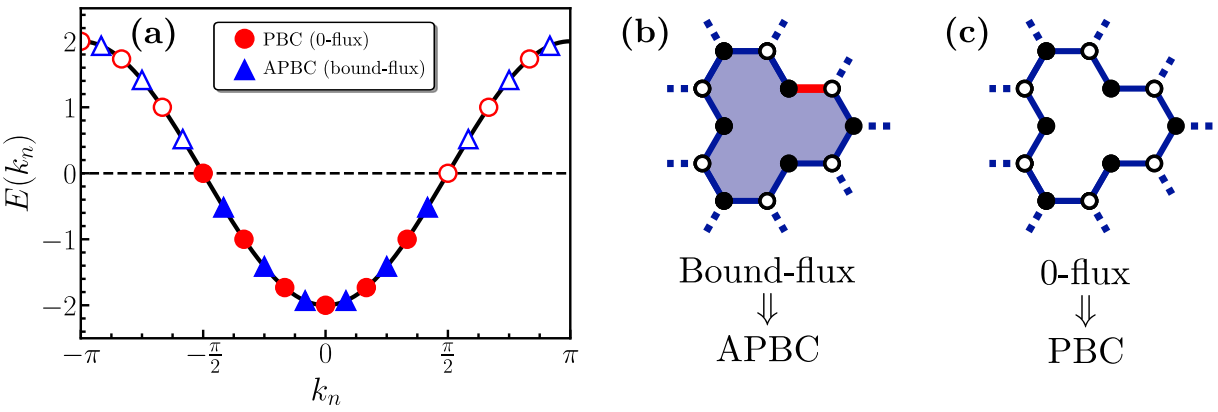

Figure 13 – (a)The spectrum of a $l = 12$ ring of fermions, for both periodic and anti-periodic boundary conditions. The filled markers indicate the occupied states, while the empty states are indicated by the open markers. (b) The $l = 12$ plaquette for the bound-flux sector. The act to flip a bond (in red) is equivalent to imposing APBC. (c) The $l = 12$ plaquette in the 0-flux. Here we have the usual PBC. The dashed links in (b) and (c) indicate the bonds present in the honeycomb lattice, which are ignored here.
Source: By the author.

This flux binding effect was shown analytically by Willans *et al.*,[108] and was also verified by numerical calculations,[42] with the vacancy embedded in the full honeycomb lattice. Therefore, it is natural to consider the situation where one flux is attached to each extended plaquette for a finite concentration of vacancies in the lattice, which we refer to as the bound-flux. To numerically construct the bound-flux sector, we follow the prescription from Ref.[42] After all vacancies positions are assigned, we randomly flip a single bond around the $l = 12$ site plaquette surrounding each vacancy, see Fig. 35(b). This binds a flux inside this plaquette. We then iteratively sweep over the lattice to guarantee

that all hexagons not surrounding the defects encompass no flux. For a given vacancy configuration, we repeat this procedure – starting at distinct random positions – until we find a link configuration corresponding to a true bound-flux state.

Once we define the static flux configuration, we diagonalize the extended Kitaev model and compute its ground state energy. The gauge sector with the smallest energy is selected as the ground state. Although biased, this variational approach is numerically efficient and exploits the integrability of the model. The results of this procedure are given in Sec. 4.1 for bond disorder and Sec. 5.1 for vacancies.

3.2 Thermodynamics and dynamics

3.2.1 Density of States and Specific Heat

The first quantity we consider is the density of states (DOS), which is a useful probe to characterize the physics of low-E Majorana excitations. The DOS can be seen as the histogram of accessible states as a function of the energy and is directly calculated from the eigenvalues E_ν coming from the exact diagonalization. For each disorder realization, the DOS is readily calculated as

$$\rho(E) = \frac{1}{N}\sum_{\nu}\delta(E - E_\nu) \tag{3.11}$$

$$\approx \frac{1}{\pi N}\sum_{\nu}\frac{\gamma}{\gamma^2 + (E - E_\nu)^2}, \tag{3.12}$$

where we have approximated the Dirac-delta function by a Lorentzian distribution. In our calculations, we set the Lorentzian broadening around $10^{-3}K$. Again, we notice that $\rho(E)$ must be averaged over all disorder realizations, and flux configurations in the case of the random-flux. We compute only the average DOS, since it is linked to the observables of interest and we do not study Anderson localization effects.

In the clean system, the ground-state DOS has a graphene-like form, with a linear low-E behavior: $\rho(E) \sim E$. For our extended model, the 0-flux remains as the ground-state in the presence of κ, and also for small values of K_3'. Therefore it is instructive to see how this parameter affects the DOS. As shown in Fig.14(a), the DOS still presents a linear behavior for a small K_3' perturbation. The situation changes dramatically as soon as κ is turned on, opening an energy gap $\Delta_\kappa \sim \kappa$ (Sec. 2.2.2). For the other ordered fluxes, the results for the low-E regime are qualitatively the same, where the only difference is the appearance of multiple bands, due to the enlargement of the Majorana unit cell.[60,105,109]

Beyond the ordered fluxes, it is instructive to study the effects of the random-flux configuration on the DOS, in the absence of defects. This case is plotted in Fig. 14(b), for different values of κ and K_3'. From this, we can see that if $\kappa = 0$, the DOS is flattened in almost the whole energy range of allowed energies. For the TRS breaking case, we see the appearance of two bands, which is reminiscent of the ordered limit of the 1/2-flux.[109]

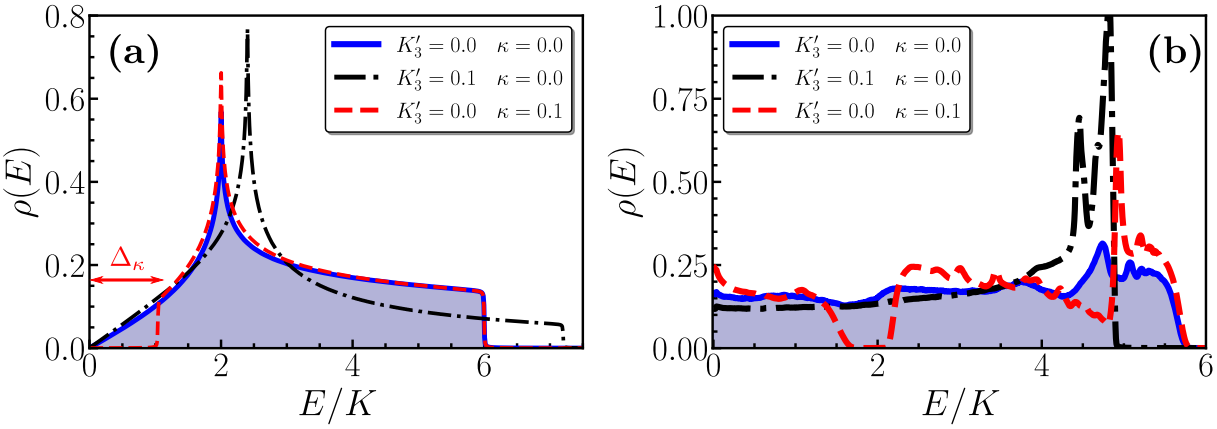

Figure 14 – The density of states in the absence of disorder, for different values of κ and K_3'. (a) The 0-flux sector DOS. The shaded curve correspond to the pure model ($\kappa = K_3' = 0$). It is possible to see the linear low-E behavior for $\kappa = 0$. For the TRS breaking case, $\kappa \neq 0$, we see the opening of the energy gap Δ_κ. (b) The random-flux sector DOS. In this case, the flux disorder blurs the Dirac-like spectrum, leading to a pile-up of low-E excitations, and the destruction of the topological gap Δ_κ. The DOS was averaged over $\sim 3 \times 10^3$ realizations of flux.
Source: By the author.

Another important result is that $\Delta_\kappa \to 0$ in the random flux, regardless of the microscopic parameters. This gapless behavior will become an important property when studying the topological features of the model (Sec. 3.3.1). Finally, we point out that in the very small energy scales, there is an apparent power-law behavior for the DOS. This is a key point to connect our minimal model with the observed $H_3LiIr_2O_6$ phenomenology. We will explore this feature in more detail in future chapters when the fully disordered system is considered.

In addition to the DOS, it is also important to consider the specific heat, $C(T)$. In the $H_3LiIr_2O_6$ experiments, this thermodynamic quantity presents a divergence in the form of a power-law $C/T \sim T^{-1/2}$,[1] and would be interesting to verify if our disordered model can reproduce this behavior, at least qualitatively. Although it is tempting to employ simple thermodynamic calculations and extract $C(T)$ directly from the DOS, the situation is quite intricate, due to the presence of the $\mathbb{Z}_2$ fluxes, which are thermally activated at finite-T. One possible way to explore the thermodynamics of the Kitaev model is via Monte-Carlo simulations,[38,39,78,102] where a sampling over the flux configurations is performed, and it is found that for $T \lesssim \Delta_{2f}$ the fluxes starts to localize, up to a point where all fluxes are frozen, and the low-T behavior of the system is dictated by the Majorana fermions dispersion.

Given the above scenario, we can assume a low-T regime where the flux configuration is frozen, allowing us to keep the exact diagonalization scheme presented so far. Because the fluxes are static the specific heat is solely dependent on the Majorana excitations, so

we can determine $C(T)$ from the DOS as usual,

$$C(T) = \frac{\partial}{\partial T} \int dE\ E\rho(E) f(E), \tag{3.13}$$

where $f(E)$ is the Fermi-Dirac distribution with the chemical potential pinned at zero: $f(E) = 1/\left(e^{E/T} + 1\right)$, since we map our spins into a half-filled Majorana fermion problem. From the linear graphene-like dispersion seen in Fig.14(a), the specific heat for the clean system is of the form $C(T) \sim T^2$. Finally, as we will see in future chapters, the DOS in the presence of disorder displays either a power-law or a gapped behavior. Therefore, because the specific heat is only determined by the DOS, from Eq.(3.13), its calculation becomes redundant. So, we will only focus on the extraction of the density of states in the disordered system.

3.2.2 Dynamical quantities

We now turn our attention to the dynamical properties of the Kitaev spin liquid. More specifically, we focus on the calculation of the static spin susceptibility, $\chi(T)$, and the nuclear magnetic resonance (NMR) relaxation rate, $1/T_1$. These are important experimental probes to characterize the nature of Kitaev candidate materials, such as $H_3LiIr_2O_6$, as discussed in Sec.2.3.2. We now describe the approximation we employ to calculate these quantities in the disordered system, where the results are shown in Sec.4.3 and Sec.5.3.

The first step is to calculate the dynamical spin structure factor, which can be directly probed via inelastic neutron scattering (INS) experiments,[110] and is defined by:[65,110]

$$S(\mathbf{q}, \omega) = \frac{1}{N} \sum_{ij} \sum_{\alpha\beta} e^{-i\mathbf{q}\cdot(\mathbf{r}_i - \mathbf{r}_j)} S_{ij}^{\alpha\beta}(\omega), \tag{3.14}$$

where $S_{ij}^{\alpha\beta}$ is the Fourier transform of the spin-spin correlation function:

$$S_{ij}^{\alpha\beta}(\omega) = \int_{-\infty}^{\infty} dt\ e^{i\omega t} \left\langle \sigma_i^{\alpha}(t) \sigma_j^{\beta}(0) \right\rangle. \tag{3.15}$$

The expected value in this expression involves the application of a spin onto the ground state. Therefore, by using the same flux selection rules discussed in Sec.2.1.2 (See Fig.4(b) and (c)), we conclude that the spin-spin correlation is ultra short-ranged, with only on-site and nearest-neighbors correlations non-zero,[66] and we choose $\mathbf{q} = 0$, for the sake of simplicity. Due to the C_3 symmetry of the problem, we only calculate its zz component (in the disordered case this symmetry holds after disorder averaging).

Conversely to the static correlations, the calculation of $S_{ij}^{\alpha\beta}(\omega)$ is quite involved, due to time dependence. As the fluxes are created, they locally change the Majoranas evolution, leading to a non-equilibrium problem. As showed by Knolle *et at.*, this is equivalent to the well-known X-ray edge problem,[111,112] and the calculation of $S_{ij}^{\alpha\beta}(\omega)$ can be performed

exactly for the clean system.[64,65] The numerical calculation in this scheme is, however, quite challenging because it requires the overlap between the original gauge configuration and the new one with a flipped bond. To reduce the computational cost, we work within the adiabatic approximation.[41,65,113] In this approach, we assume this overlap to be always finite and we perform all calculations in the new gauge configuration[†]. Therefore, it is possible to show that $S^{zz}(\mathbf{q}=0,\omega)$ takes the following form:[65]

$$S^{zz}(\mathbf{q}=0,\omega) = \sum_{\nu} \delta(\omega - E_\nu - \Delta_{2f})|X_{\nu o}|^2 f(-E_\nu) + \sum_{\nu} \delta(\omega + E_\nu - \Delta_{2f})|Y_{\nu o}|^2 f(E_\nu), \tag{3.16}$$

where $X_{\nu o}$ and $Y_{\nu o}$ are the Bogoliubov matrices defined in Eq.(3.6), and the index o specifies the flipped bond position. The derivation of Eq.(3.16) is presented in the appendix C.

The static spin susceptibility can be obtained from $S^{zz}(\mathbf{q}=0,\omega)$ via the fluctuation-dissipation theorem[58]

$$\chi(T) = \int_{-\infty}^{\infty} d\omega\; S(\mathbf{q}=0,\omega)\; \frac{1-e^{-\omega/T}}{\omega}. \tag{3.17}$$

Substituting the $S^{zz}(\mathbf{q}=0,\omega)$ expression in Eq.(3.16) in the above definition, we get the final form of $\chi(T)$,

$$\chi(T) = \sum_{\nu} |X_{\nu o}|^2 f(-E_\nu)\; \frac{1-e^{-(E_\nu+\Delta_{2f})/T}}{E_\nu+\Delta_{2f}} + |Y_{\nu o}|^2 f(E_\nu)\; \frac{1-e^{(E_\nu-\Delta_{2f})/T}}{-E_\nu+\Delta_{2f}}. \tag{3.18}$$

In addition to the spin susceptibility, we also calculate the NMR relaxation rate, $1/T_1$. In an NMR experiment the sample is subject to magnetic pulse with an intensity close to the nuclear spins resonance frequency, ω_0. The spin of the nuclei couple to the surrounding electronic spins via the hyperfine interaction.[114,115] The transitions induced by the hyperfine Hamiltonian modify the nuclear magnetization, by changing the spin population on each level. The relaxation rate, $1/T_1$ is then defined as the decay rate in which the longitudinal component of the nuclear magnetization reaches its equilibrium value after the magnetic pulse is turned off.[114]

From this qualitative discussion, we can compute the relaxation rate as the spin-flip decay rate provoked by the hyperfine interaction, which can be determined by Fermi's golden rule:[58]

$$\frac{1}{T_1} \propto \frac{1}{1-e^{\omega_0/T}} \sum_{\mathbf{q}} |A_{\mathbf{q}}| \chi''_{+-}(\mathbf{q},\omega_0), \tag{3.19}$$

where $A_{\mathbf{q}}$ is the hyperfine coupling, ω_0 is the nuclear resonance frequency, and $\chi''_{+-}(\mathbf{q},\omega_0)$ is the imaginary part of the dynamical susceptibility for the spin component transverse

[†] Recall that there is no orthogonality catastrophe for a graphene-like DOS

to the applied field. From the theory of linear response, we can relate $\chi''_{+-}(\mathbf{q},\omega_0)$ the dynamical structure factor as[58]

$$S^{+-}(\mathbf{q},\omega_0) = \frac{1}{\pi(1-e^{\omega_0/T})}\chi''_{+-}(\mathbf{q},\omega_0) \tag{3.20}$$

where $S^{+-}(\mathbf{q},\omega_0)$ is the transverse component of the dynamical structure factor. However, as aforementioned we only need to compute S^{zz}, due to the C_3 symmetry of the problem and because the magnetization M_z is not conserved. In NMR experiments, ω_0 is generally much smaller than other energy scales,[114] so we can set $\omega_0 \to 0$. In addition, we assume the hyperfine form factor $A_{\mathbf{q}}$ as a constant. Finally, the NMR relaxation rate can be easily calculated in the adiabatic approximation as

$$\frac{1}{T_1} \propto S^{zz}(\mathbf{q}=0,\omega_0)\Big|_{\omega_0\to 0}, \tag{3.21}$$

where $S(\mathbf{q}=0,\omega_0)$ is given by Eq.(3.16).

To calculate $\chi(T)$ and $1/T_1(T)$ we need not only to diagonalize the system with a bond flipped but also we need to know the value of the two flux gap Δ_{2f}: the energy difference between the configuration with a single link variable flipped with respect to the reference gauge sector. The flux pair gap in the ground state is well known, with its value given by $\Delta_{2f}/K = 0.27$. The other ordered sectors are also gapped, and the values of Δ_{2f} can be checked in Ref.[13] In all random-flux calculations, we use the average value of Δ_{2f}, instead of its value on each particular realization. In the absence of bond and site disorder, we find $\Delta_{2f} \to 0$ on average for the random-flux sector (See Fig. 12).

Before we explore the dynamics in the presence of disorder, it is instructive to discuss the results for the clean system. Here we calculate both $\chi(T)$ and $1/T_1(T)$ for the 0-flux and the random-flux, where the flux pair gap is given by $\Delta_{2f} = 0.27$ and $\Delta_{2f} = 0$, respectively.

For the static susceptibility (Fig.15(a)), both the 0-flux and random-flux follows the expected Curie-Weiss law behavior at high-T, with $\chi(T) \sim 1/(4T)$. On the other hand, there is a discrepancy in the low-T regime. In this case, the 0-flux is constant, while the random-flux diverges. We can qualitatively explain this scenario with a simple exercise. Let us consider the low-E contribution to the temperature dependence on $\chi(T)$. Because we have two basic excitations, the Majoranas and the fluxes, the lowest energy scale in the problem is the flux pair gap, Δ_{2f}, as we set $E_\nu \to 0$ for the Majoranas. In the adiabatic approximation, Eq.(3.18), this limit gives the following contribution to $\chi(T)$

$$\chi(T) \propto \left[\frac{X_o}{\Delta_{2f}}\left(\frac{1-e^{-\Delta_{2f}/T}}{2}\right) + \frac{Y_o}{\Delta_{2f}}\left(\frac{1-e^{-\Delta_{2f}/T}}{2}\right)\right], \tag{3.22}$$

where X_o and Y_o are constants proportional to the spectral weight from the Bogoliubov matrices. From this expression, it is easy to see that the low-T limit, $T \to 0$, is given by

$$\chi(T) \propto \frac{1}{\Delta_{2f}}. \tag{3.23}$$

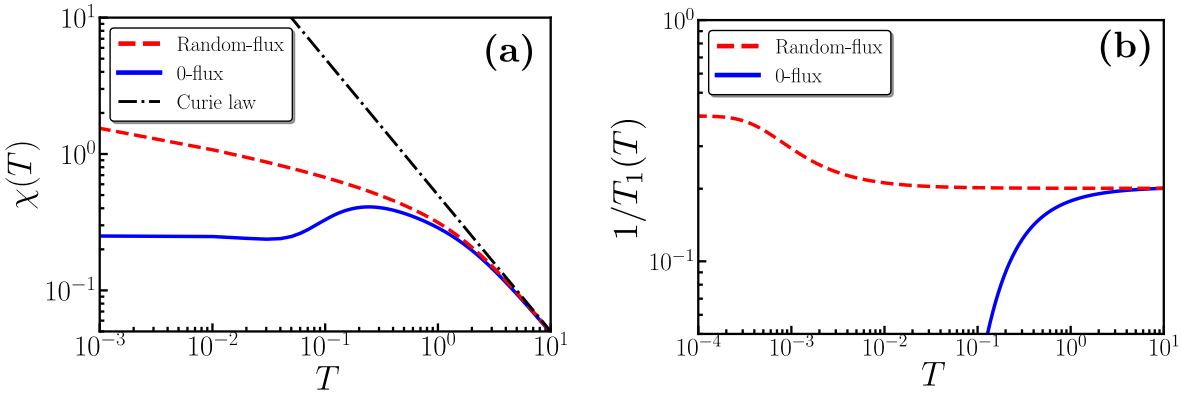

Figure 15 – (a) The static spin susceptibility for the clean system, in the log-log scale. For the 0-flux, we see the constant behavior at low-T, due to the finite flux pair gap Δ_{2f}. For the random-flux, $\Delta_{2f} \to 0$, which causes the apparent power-law divergence in the low-T regime. For both cases, the high-T regime follows the Curie law. (b) The NMR relaxation rate in the clean system, in the log-log scale. For the 0-flux $\Delta_{2f} \neq 0$, so we have an exponential decay. The scale was adjusted to highlight the discrepancy between the random and 0-flux results. For the random-flux, $1/T_1$ is constant at $T \to 0$, due to the gapless flux excitations.
Source: By the author.

Although seemingly naive, this argument succeeds in explaining the low-T discrepancy observed for $\chi(T)$. It is clear now that the origin of this behavior can be traced back to the flux pair gap. If $\Delta_{2f} \neq 0$, the susceptibility displays a constant low-T behavior,[‡] which is the case for the 0-flux (Fig.15(a)), and for the other ordered fluxes as well. On the other hand, if we set $\Delta_{2f} \to 0$, the spin susceptibility diverges, which qualitatively explains the random-flux scenario in Fig.15(a). A more careful analysis is presented in Sec.4.4, where the divergence on $\chi(T)$ is connected with the low-E DOS in the presence of disorder.

Finally, we can use a similar argument to interpret the $1/T_1$ results presented in Fig.15(b). Here we consider Eq.(3.16), where the energies E are filtered by the delta distribution. If we assume $\Delta_{2f} \neq 0$, the temperature dependence on $1/T_1$ is proportional to

$$\begin{aligned} \frac{1}{T_1} &\propto \frac{1}{e^{-(\omega_0+\Delta_{2f})}+1}\Big|_{\omega_0\to 0} \\ &\propto e^{-\Delta_{2f}/T}. \end{aligned} \tag{3.24}$$

Therefore, the 0-flux sector must have an exponential decay, as presented in Fig.15(b). From this argument, it is also easy to see that $\Delta_{2f} \to 0$ gives us a constant relaxation rate, as we checked for the random-flux. This constant behavior indicates a proliferation of low-energy magnetic excitations, as observed in the $H_3LiIr_2O_6$ experiment[1,19] (Sec.2.3.2).

‡ This is analogous the Pauli paramagnetism, where here the flux gap plays the role of a finite Fermi energy.[116]

From this discussion, we conclude that because of the fractionalized nature of the problem, the qualitative behavior of the dynamical quantities in the low-T regime is dictated by the flux pair gap, Δ_{2f}. Therefore, the calculation of Δ_{2f} will become a key piece of information to characterize the basic properties of the Kitaev spin liquid in the presence of disorder, as we will explore in the following chapters.

3.3 Topology and edge modes

3.3.1 Bott Index

Without time-reversal symmetry, $\kappa \neq 0$, the extended Kitaev model is topologically non-trivial in the clean limit.[13,105,106] To characterize the distinct topological phases, we calculate the Bott Index, which is equivalent to the Chern number (Eq.(2.40)) in periodic systems.[117–119] As we will see shortly, the Bott index relies only on the spatial structure of the Hamiltonian, and therefore it is more conveniently implemented in systems lacking translational invariance.[117,120,121] The Bott Index is defined as:

$$\mathcal{B} = \frac{1}{2\pi} \operatorname{Im} \left\{ \operatorname{Tr} \left[\log \left(V U V^\dagger U^\dagger \right) \right] \right\}, \tag{3.25}$$

where the matrices U and V are given by

$$P e^{2\pi i R_x/L} P = \begin{pmatrix} X^* & Y^* \\ Y & X \end{pmatrix} \begin{pmatrix} 0 & 0 \\ 0 & U \end{pmatrix} \begin{pmatrix} X^T & Y^\dagger \\ Y^T & X^\dagger \end{pmatrix}, \tag{3.26}$$

$$P e^{2\pi i R_y/L} P = \begin{pmatrix} X^* & Y^* \\ Y & X \end{pmatrix} \begin{pmatrix} 0 & 0 \\ 0 & V \end{pmatrix} \begin{pmatrix} X^T & Y^\dagger \\ Y^T & X^\dagger \end{pmatrix}. \tag{3.27}$$

Here, P is the projector onto the occupied states, $P = \sum_{E_\nu<0} |\psi_\nu\rangle \langle\psi_\nu|$. In terms of the Bogoliubov matrices, we can write P as

$$P = \begin{pmatrix} X^* & Y^* \\ Y & X \end{pmatrix} \begin{pmatrix} 0 & 0 \\ 0 & \mathbb{1} \end{pmatrix} \begin{pmatrix} X^T & Y^\dagger \\ Y^T & X^\dagger \end{pmatrix}, \tag{3.28}$$

with X and Y defined in (3.7). The operators R_x and R_y are diagonal matrices whose entries correspond to the unit cell positions x_i and y_i, respectively. Mathematically speaking, the Bott index measures the non-commutativity of a couple of unitary or almost unitary matrices, U and V in this case.[117] Physically speaking, this commutativity measure encodes information about the localization properties of the system. It can be shown that the existence of exponentially localized Wannier functions implies the vanishing of the Bott index,[122] which in turn implies the existence of a topologically trivial state.[123]

To increase the stability of the numerical algorithm, we perform a singular value decomposition on U and V: $U = \Sigma S \Theta^\dagger$, where S is diagonal, and Σ and Θ are unitary matrices. With this, we redefine the projected matrices as $\widetilde{U} \equiv \Sigma\Theta^\dagger$, which is equivalent to a scaling transformation and does not change the Bott Index.[121]

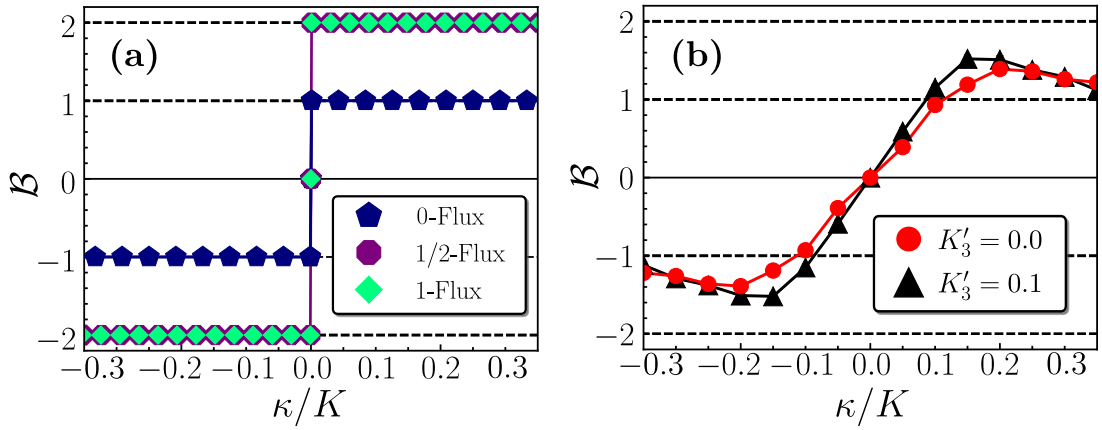

Figure 16 – Bott Index $\mathcal{B}$ as a function of κ for the clean case. We show results for different ordered flux sectors in (a), where $\mathcal{B}$ is quantized. For the random-flux (b), the curves depend on K_3', and topology is lost. We considered $L = 30$ and average over 100 link configurations for the random-flux case.
Source: By the author.

For the disordered system we calculate the Bott Index averaged over N_s samples, $\mathcal{B} = \sum_{i=1}^{N_s} \mathcal{B}_i/N_s$, where $\mathcal{B}_i$ is the Bott index for a particular sample i. Our numerical algorithm only returns values of $\mathcal{B}_i$ that are integers, reinforcing the robustness of the method. Therefore, the averaged value of the Bott index corresponds to the proportion of topologically non-trivial samples found for a particular set of parameters. As a benchmark, we present results for the clean case in Fig. 16. For the 0-flux gauge, we get $\mathcal{B} = \pm 1$. For the 1-flux and 1/2-flux cases, see Fig. 11, we have $\mathcal{B} = \pm 2$, as we have the contribution from two filled bands.[13,106,124] For the random-flux case, however, the averaged value of $\mathcal{B}$ is no longer quantized, even in the absence of disorder in the bonds, $\delta K = 0$. We interpret this result as the lack of a topological phase for this particular flux sector. This is consistent with the absence of a topological gap in the DOS, Fig. 14

We can trace back the destruction of the topological phase in the random-flux sector to the random orientation of the NNN hoppings induced by the random-flux gauge. This happens because of the 2-bond structure of the κ term in (2.51), which picks the signs of the random u_{ij} configuration, destroying its chiral pattern (See Fig.9). To better understand how this affects the topological properties of the system, we propose the following exercise. Instead of the random-flux sector, we consider the 0-flux in the presence of a κ interaction with random orientations. This can be implemented by sorting the local sign of NNN interactions in the same way as we do for the random-flux. The idea here is to mimic the effects of random orientations in the κ-term provoked by the random-flux gauge.

We diagonalize this system for several realizations of random orientations, and different values of κ, so we can compute the DOS and the Bott index. Notably, the random orientation closes the gap, regardless of the value of κ. In fact, the DOS in Fig.17(a)

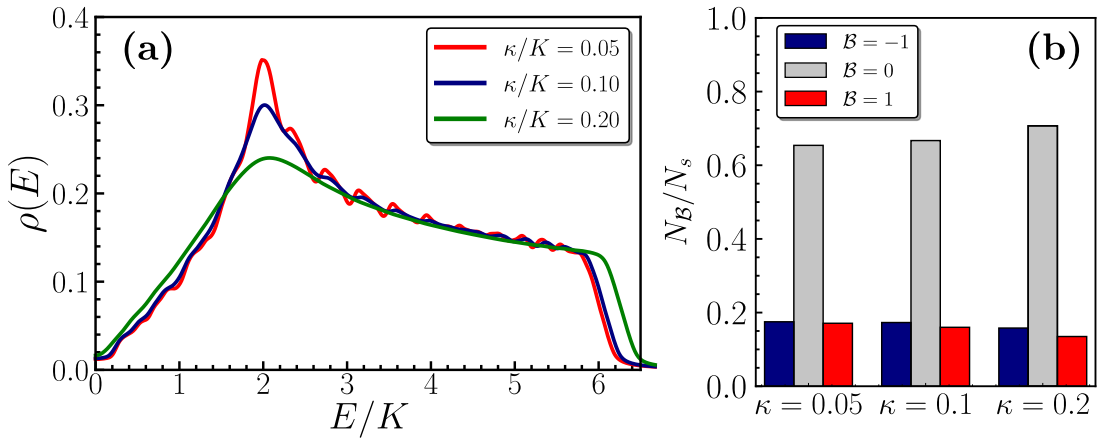

Figure 17 – (a) DOS for the Kitaev model with the random-κ term. Here we can see the closing of the topological gap, for all $\kappa \neq 0$. (b) The normalized histogram of the Bott index over N_s realizations of random signs. For all values of κ, the average value of $\mathcal{B}$ is zero.
Source: By the author.

resembles very much the clean limit, with $\kappa = 0$. To further understand the fate of topology in this system we consider the distribution of Bott index values for all realizations. In Fig.17(b) we plot $N_{\mathcal{B}}/N_s$ over the possible outcomes, $\mathcal{B} = 0, \pm 1$, where $N_{\mathcal{B}}$ stands for the number of realizations with a topological index equals to $\mathcal{B}$ and N_s is the number of samples. We observe that the majority of samples returns $\mathcal{B} = 0$, while the contributions with $\mathcal{B} \neq 0$ are approximately equal, so $\mathcal{B} = 0$ on average. From this perspective, we link the lack of topological phase in the random-flux to the random orientation of NNN hoppings.

3.3.2 Level Statistics

As discussed briefly in section 2.2.2, the Kitaev model in the presence of a field, $\kappa \neq 0$, hosts chiral edge modes, in resemblance to the quantum Hall effect.[3] Due to its experimental appeal,[32,36] we are interested in further exploring the robustness of the edge modes under the presence of disorder, beyond the topological number calculation presented previously.

For the clean system, it is possible to extract the edge modes contribution to the spectrum, by considering open boundary conditions(OBC). A simple way to implement this is to cut the honeycomb lattice in such a way that only the lower half-plane is filled, as illustrated in Fig.18(a). In this geometry, we impose PBC along the x-direction. By performing the Fourier transform in the horizontal direction, Kitaev showed that the edge modes spectrum for very small κ takes the approximate form: $E(k_x) \approx 12\kappa \sin(k_x)$, with $k_x \in [2\pi/3, 4\pi/3]$ (See Fig. 18(b)). Although this is just an approximation, this calculation is capable to show an important qualitative feature of the spectrum in the topological phase: the presence of an edge state inside the gap, with a well-defined chirality, which is

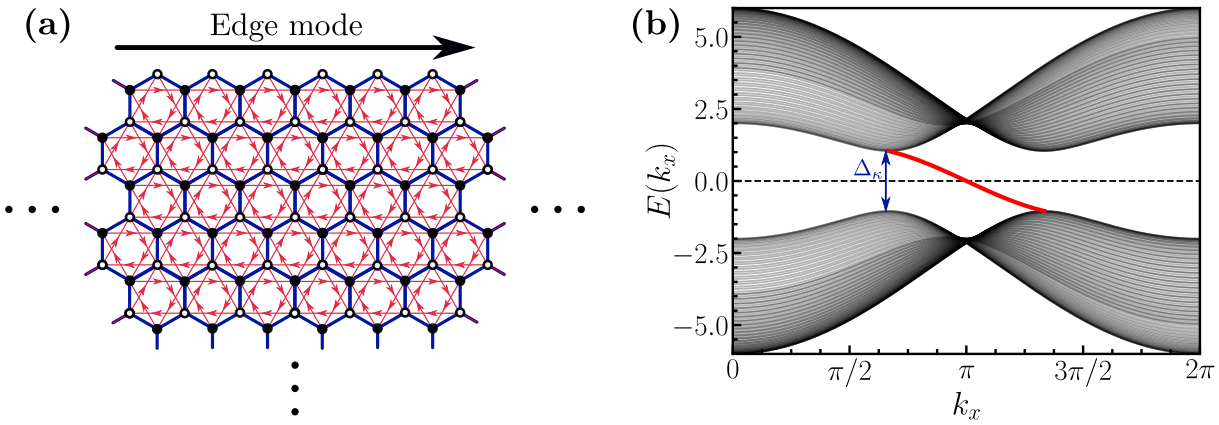

Figure 18 – (a) The Kitaev honeycomb model with OBC in the y-direction. The lattice fills the lower half-plane, giving rise to a chiral edge mode when $\kappa \neq 0$ (NNN hoppings in red). (b) The spectrum for the system is depicted in (a). The filled gray region corresponds to the bulk spectrum, with an energy gap given by Δ_κ. The in-gap edge mode is plotted in red.
Source: By the author.

labeled by a topological number $\mathcal{B} = 1$.

However, in the disordered system, we lost translation symmetry, forbidding us to employ the formulation presented in the above discussion. Although it is still possible to numerically extract the edge modes with open boundary conditions, we take advantage of the bulk-boundary correspondence,[3] and focus our attention only on the bulk properties of the system, by imposing PBC. In this sense, to probe the extent of the bulk states, we employ a level statistics study of the spectrum.[125] This is a well-established technique from the theory of random matrices and is widely used in the context of localization,[126–128] and disordered topological insulators.[125,129,130] This investigation is particularly useful to assess the stability of the topological gap in the Majorana spectrum in the presence of disorder and complement the information coming from the Bott index. Specifically, we compute the average of the level spacing ratio[126]

$$\widetilde{r}_\nu = \frac{\min(\delta_\nu, \delta_{\nu-1})}{\max(\delta_\nu, \delta_{\nu-1})} = \min\left(\frac{r_\nu}{r_{\nu-1}}\right). \tag{3.29}$$

Here $\delta_\nu = E_{\nu+1} - E_\nu$ is the difference between two adjacent energy levels E_ν from a given disorder realization and $r_\nu = \delta_\nu/\delta_{\nu-1}$. Notice that $\widetilde{r}_\nu$ is constrained to the interval $[0, 1]$ by definition.

For extended states, the ratio follows the Gaussian unitary ensemble (GUE) statistics, given by the following distribution[131]

$$P_{\mathrm{GUE}}(\widetilde{r}) = \frac{81\sqrt{3}}{4\pi}\frac{(\widetilde{r} + \widetilde{r}^2)^2}{(1 + \widetilde{r} + \widetilde{r}^2)^4}, \tag{3.30}$$

and the average value of $\widetilde{r}$ is $\langle\widetilde{r}\rangle_{\mathrm{GUE}} \approx 0.60266$. On the other hand, exponentially localized

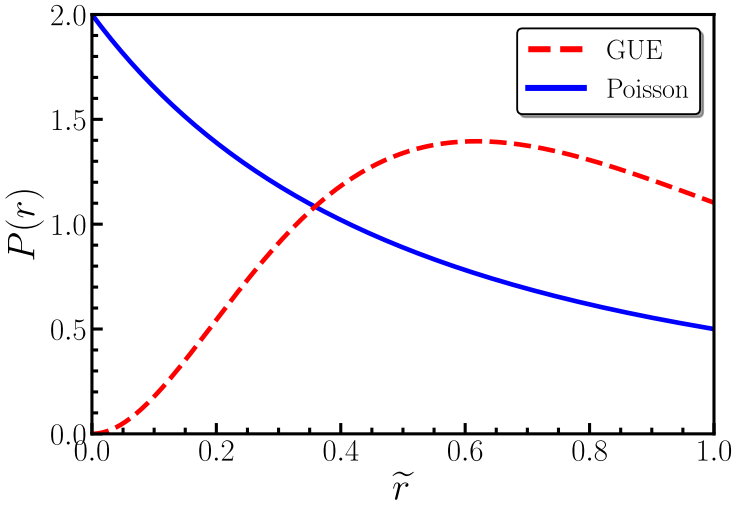

Figure 19 – The distributions of the level spacing ratio $\tilde{r}$. The histogram of $\tilde{r}$ of an extended state with an energy E follows the GUE distribution (dashed line). For exponentially localized states, we expect the Poisson distribution (solid line).
Source: By the author.

states follow the Poisson statistics,[131]

$$P_{\text{Poisson}}(\tilde{r}) = \frac{2}{(1+\tilde{r})^2} \tag{3.31}$$

with $\langle\tilde{r}\rangle_{\text{Poisson}} \approx 0.38629$.[131] The definition in Eq. (3.29) is particularly useful because it avoids the definition of a local average level spacing. In practice, we calculate $\langle\tilde{r}\rangle$ at a given energy E using a small energy window of 5 levels above and below E,[125] so we can plot $\langle\tilde{r}\rangle$ as a function of the energies. In addition, it is possible to plot the histogram of $\tilde{r}_\nu$ for a given energy, and compare it with the exact distributions plotted in Fig.19.

4 BOND DISORDER IN THE KITAEV MODEL

We now add disorder to the model in Eq. (2.51). Specifically, we consider a binary bond disorder for the Kitaev couplings setting $K \to K \pm \delta K$, with probability 0.5 to generate either a weak $(K - \delta K)$ or a strong bond $(K + \delta K)$ (See Fig.10(a)). For simplicity, we assume the couplings κ and K_3' to be homogeneous. In terms of Majorana fermions, this problem translates into a random hopping problem on a bipartite lattice. In this chapter, we present the results for the DOS, where the power-law observed in the $H_3LiIr_2O_6$ experiment[1] is discussed. To further explore the effects of bond disorder on the thermodynamic response, we also calculate the static uniform susceptibility and the NMR relaxation rate, employing the adiabatic approximation. Finally, by calculating the Bott index and the level statistics, we discuss the fate of the chiral edge modes in the presence of bond disorder.

4.1 Fluxes and ground-state energy

Before we explore the thermodynamics and dynamics of the extended model in the presence of disorder, we investigate how the ground state energy changes under variations of the disorder strength, δK, for different flux sectors. This is an important step, as we can select the energetically favorable flux configurations for a given set of parameters and perform all subsequent calculations within this flux sector.

Therefore, after fixing the flux state and the disorder strength, we numerically diagonalize the extended model for several bond disorder realizations and compute the average ground state energy. In Fig. 20(a) we show the ground state energy as a function of the bond disorder for different flux sectors for $\kappa = K_3' = 0$. At weak disorder, the 0-flux state is the ground state, thus evolving adiabatically from the clean limit.[13] On the other hand, we find that the static flux configuration is sensitive to strong disorder.[113] Specifically, we find that for $\delta K \gtrsim 0.6$ the ground state energies of the different flux sectors become comparable within error bars. This implies that $\Delta_{2f} \to 0$ as $\delta K \to 1$, per recent Quantum Monte Carlo results in Refs.[132,133] We interpret this result as a tendency towards the random-flux state for strong disorder,[113] so we consider this as a competitive variational flux state. Moreover, we find this generic behavior remains valid for small values of κ.

In addition, we investigate how the TR symmetric term, K_3', changes the ground state energy in the presence of bond disorder. For the clean system, we find a flux transition around $K_3' = 1/8$, from the 0-flux to the 1-flux configuration –as discussed in the Appendix B– and it is natural to expect an approximately similar behavior for weak disorder. However, this might not be true for the strong disorder regime. Therefore, we compute the

ground state energy as a function of K_3' for fixed bond disorder $\delta K = 0.8$, as presented in Fig.20(b). Even in this limit, we observe a tendency towards the 1-flux state as K_3' increases, which is reminiscent of the transition in the clean limit. Nevertheless, all energies coincide within error bars for small values of K_3', which again points to the random-flux as a competitive state.

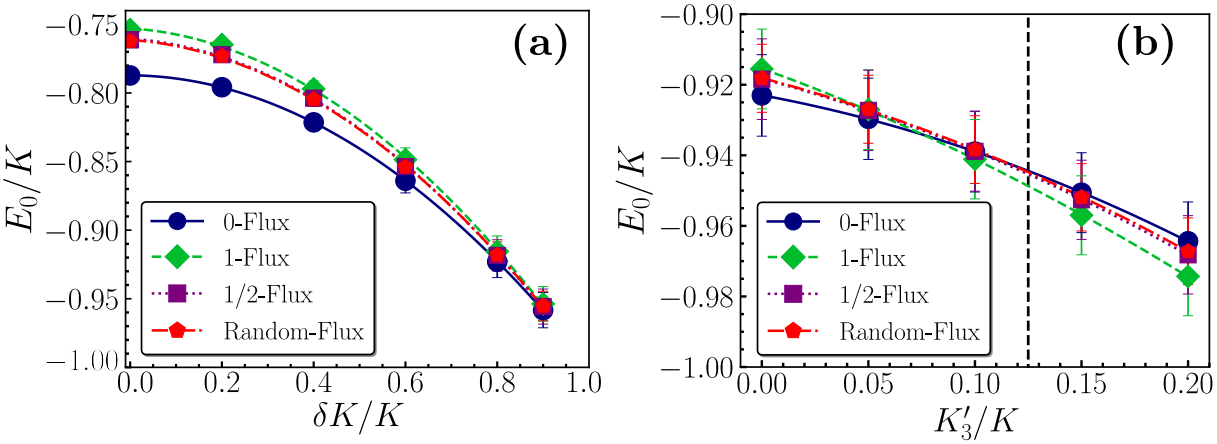

Figure 20 – (a) Ground state energy per site, E_0, as a function of the bond disorder strength δK for $\kappa = K_3' = 0$. (b) E_0 as a function of K_3' for $\delta K = 0.8$ and $\kappa = 0$. The dashed line indicates the flux transition in the clean system, $K_3'/K \approx 1/8$. We considered $L = 30$ and up to 3×10^3 disorder realizations.
Source: By the author.

4.2 Results for the DOS: Power law divergence

In this section, we show the numerical results for the DOS in the presence of bond disorder. From our analysis of the ground state energy presented in the previous section, we focus our attention on the random-flux sector and compare it with the original ground state, the 0-flux. The numerical procedure is described in Sec.3.2.1.

Before we show our numerical outcomes, it is useful to review some general aspects concerning the DOS for disordered systems. In the 0-flux sector, our model is equivalent to the problem of random hopping on a bipartite lattice for Dirac fermions.[45] This is a well-known problem, which has been widely studied for different symmetry classes in various contexts in the last two decades.[134–136] In the present particle-hole symmetric case, for $\kappa = K_3' = 0$, it is rigorously known that the density of states (DOS), Eq.(3.11), has a low-E divergence

$$\rho(E) \sim \exp\left(-c\,|\ln E|^{2/3}\right)/E, \tag{4.1}$$

where c is a positive constant.[45] Nevertheless, this divergence occurs only at asymptotically low-energy scales, eluding even large-scale numerical simulations.[45] This fact probably places it outside the experimentally accessible regimes for magnetic materials. Moreover,

as reported in the previous section, strong disorder in the Kitaev model may also affect the flux state, making this asymptotic scenario not too relevant for our analysis.

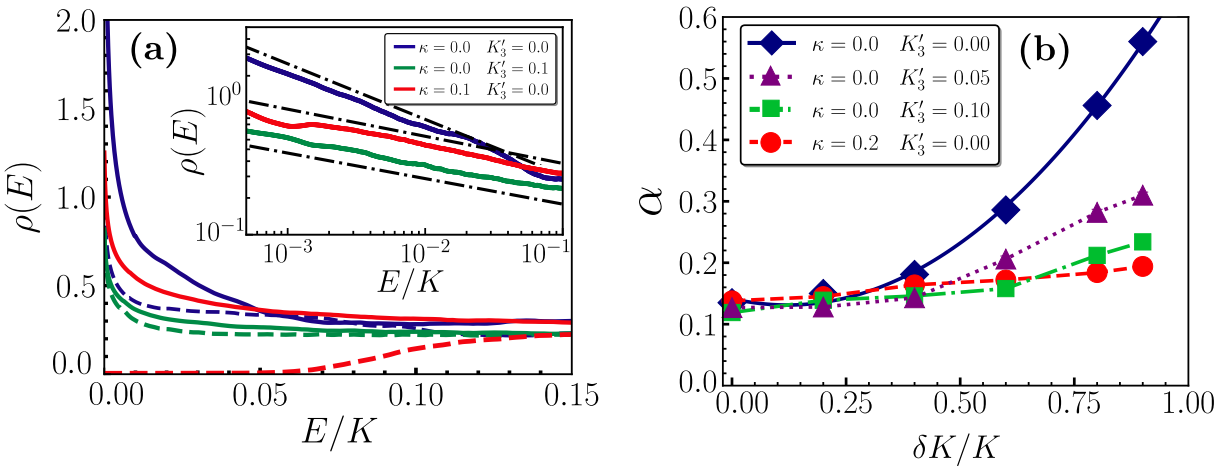

Figure 21 – (a)DOS as function of the energy for $\delta K = 0.8$. Inset: log-log plot showing the power-law divergence at low-E. The full curves correspond to the random-flux, while the 0-flux is represented by the dashed curves. The dot-dashed curves are power-law fits that are shifted with respect to the original curves. (b)Non-universal power-law exponent α for the extended Kitaev model, Eq. (2.51), in the random-flux sector with bond disorder as a function of the disorder strength δK. We observe $\alpha \approx 0.13$ for $\delta K = 0$. We consider different values of κ and K_3', $L = 30$, and 3×10^3 disorder realizations.
Source: By the author.

The problem of bond disorder in the Kitaev honeycomb model has already been addressed in previous numerical studies,[41,92] where the divergence in the low energy DOS was identified as a power-law distribution, in accordance with the $H_3LiIr_2O_6$ phenomenology. Here, we report the same qualitative behavior for the pure Kitaev model, and further extend the analysis by considering the extended model in Eq.(2.51).

In Fig. 21(a) we show the the averaged low-E DOS for $\delta K = 0.8$. For $K_3' = \kappa = 0$, both the 0-flux and random-flux states produce the desired diverging power-law behavior at low-E: $\rho(E) \sim E^{-\alpha}$, in agreement with the results of Refs.[41,92] First, we shall notice that if one assumes that the flux degrees of freedom are frozen, it follows that $C/T \sim T^{-\alpha}$,[41,42] as observed in $H_3LiIr_2O_6$.[1] Furthermore, we point out that a pile-up of low energy states is only seen for the 0-flux configuration in the strong disorder regime presented in Fig. 21(a), for $\kappa = 0$. If $\kappa \neq 0$, the 0-flux state displays a gap in the Majorana spectrum, which is reminiscent of the topological gap present in the clean case.[13]

Meanwhile, the random-flux sector already displays a mild divergence for $\delta K = 0$, as presented in Fig.14(b), highlighting the fact that the random-flux sector favors an accumulation of low-E states even in the absence of disorder. In the strong disordered case, we observe the power-law remains. However, from the inset in Fig.21(a), it is clear that the power-law exponent α is non-universal and it depends continuously on the model

parameters. In Fig.21(b) we show the non-universal power-law exponent α as a function of $\delta K/K$ and different values of κ and K_3'. We compute α by means of the maximum likelihood estimator, as described in Appendix D. The evolution of α is sensitive to all parameters, where its value increases with disorder and is suppressed by κ and K_3'. This is in accordance with the power-law suppression observed for the $H_3LiIr_2O_6$ in an external field.[1]

4.3 Results for the dynamical quantities

As a preliminary step to the dynamical quantities calculations, we need to compute the flux pair gap, Δ_{2f} in the presence of bond disorder. The procedure, along with the clean system results, is described in Sec.3.2.2. In Fig. 22(a), we present the average value of Δ_{2f} as a function of $\delta K/K$, for the pure Kitaev model: $\kappa = K_3' = 0$. For this case, the flux pair gap vanishes in the random-flux sector for all values of $\delta K/K$ and we set $\Delta_{2f} = 0$ in our calculations. For the 0-flux sector, Δ_{2f} is finite and approaches zero in the limit of strong disorder, $\delta K/K \to 1$,[133,137] The vanishing of the flux gap in the strongly disordered regime is consistent with our ground state energy calculations, Fig. 20.

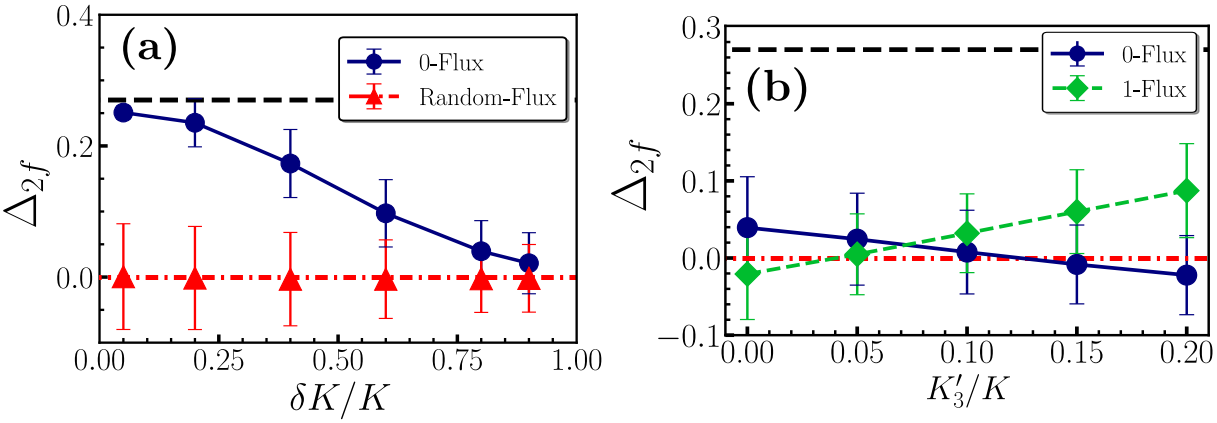

Figure 22 – The flux pair gap Δ_{2f} as a function of disorder for $\kappa = K_3' = 0$. The dashed line corresponds to its clean value, $\Delta_{2f} \approx 0.27K$. (a) Δ_{2f} as a function of the strength of the bond disorder $\delta K/K$. (b) Δ_{2f} as a function of K_3'/K for the strong disordered scenario, $\delta K/K = 0.8$. Here we compare the 0-flux with the 1-flux sector. We considered $L = 30$ and 3×10^3 realizations of disorder.
Source: By the author.

In the TR breaking case, $\kappa \neq 0$, we set the flux gap to the same values displayed in Fig.22(a). Here we argue that, as κ does not change the flux state, Δ_{2f} should be an independent function of κ. On the other hand, the K_3' term induces a flux transition, so it is natural to inquire if Δ_{2f} depends on K_3'. We therefore compute Δ_{2f} for the random and 0-flux sectors, with strong disorder, $\delta K/K = 0.8$. In addition, we consider the flux pair gap for the 1-flux sector, just for the sake of comparison, as this is the ground-state for moderate values of K_3' (see Fig.20(b)). In Fig.22(b) we observe that Δ_{2f} is a decreasing function of K_3' in the 0-flux, where the gap is positive only for $K_3' \lesssim 1/8$. This is again a

reminiscent result of the flux transition in the clean system. As the value of K_3' is increased, the 0-flux sector becomes less favorable, which in turn makes the flux pair creation less costly in energy. Beyond the transition point ($K_3' \approx 1/8$), the flux pair gap is naturally negative, as the 1-flux sector is energetically favorable against the 0-flux. Finally, we find that the random-flux sector still has a vanishing gap, regardless of the K_3' value.

Now, with the values of Δ_{2f} already extracted, we can employ the adiabatic approximation (Sec.3.2.2) to compute the static spin susceptibility, $\chi(T)$, given by Eq.(3.18) and the NMR relaxation rate, $1/T_1$, as in Eq.(3.21). We show sample results for different values of κ and K_3' with $\delta K = 0.8$ in Fig. 23.

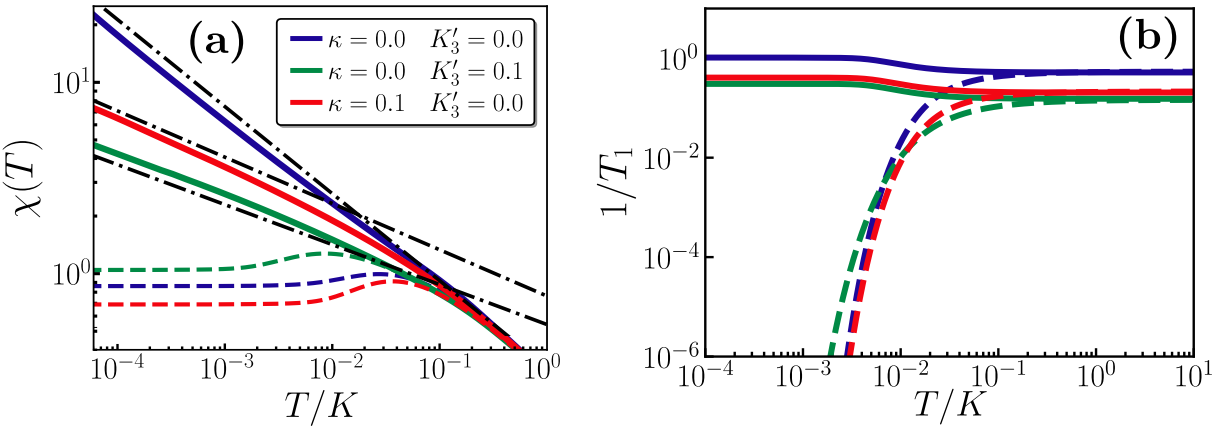

Figure 23 – Static uniform spin susceptibility(a) and NMR relaxation rate(b) as a function of the temperature in a log-log plot for $\delta K = 0.8$. We consider the same parameters in (a) and (b). The dot-dashed curves in (a) are power-law fits that are shifted with respect to the original curves, and the full (dashed) curves correspond to random (0)-flux. We considered $L = 30$ and 3×10^3 realizations of disorder.
Source: By the author.

In Fig. 23(a), the random-flux sector shows a diverging susceptibility $\chi \sim T^{-\alpha}$ at low-T, while the 0-flux state shows a finite χ at low-T. As discussed in Sec.3.2.2, we can trace back these behaviors to the value of Δ_{2f}. In the 0-flux state, Δ_{2f} remains finite, albeit smaller, for $\delta K > 0$,[133,137] and the susceptibility goes to a constant for $T < \Delta_{2f}$. In the random-flux state, $\Delta_{2f} \to 0$ and we expect a divergence on the spin susceptibility, as anticipated in Eq.3.23. More interesting, however, is the fact that $\chi(T)$ follows $\rho(E)$ at low energies, so α is the same as in Fig.21(a), in line with the results for $H_3LiIr_2O_6$.[1] As we shall see in next section, these observations can be explained with a single argument, based on the presence of rare-regions in the bulk.

Finally, the NMR relaxation rate is presented in Fig.23(b). Here we adjust the scale to highlight the discrepancy between the random and 0-flux results, as in the clean case, Fig.15(b). As expected, the random-flux has a flat curve for $1/T_1$, which points to a large amount of low-E magnetic excitations, as observed in the $H_3LiIr_2O_6$ experiment.[1] Meanwhile, the 0-flux display an exponential decay, as anticipated in Eq.(3.24). It is also

possible to observe that in the $K_3' \neq 0$ case the curve is slightly dislocated from the other two cases. This comes from the fact that Δ_{2f} is not the same for $K_3' \neq 0$, which further corroborates the qualitative expression of the NMR relaxation rate, $1/T_1 \sim e^{-\Delta_{2f}/T}$.

4.4 Rare regions and Griffiths-like scenario

4.4.1 Rare regions and the origin of the power-law behavior

We now present a physical mechanism behind the singularities in the low-E DOS. Power-law distributions of energy scales are commonly observed in the vicinity of quantum critical points in disordered systems,[44–49] in the so-called Griffiths phase. This phenomenon is typically associated with statistically rare fluctuations caused by the presence of quenched disorder, generally called rare regions. They were first observed in the context of the FM 2D Ising model,[138,139] and later with a variety of other physical systems.[44,46–49] Even though the Kitaev spin liquid displays no phase transition in 2D,[39] we exploit this similarity with the Griffiths phases and propose a rare region mechanism to explain the power-law in the DOS.

We define a rare region as a droplet connected to the bulk through weak couplings only, as illustrated in Fig. 24(a). Now, suppose a rare region of linear size ℓ. The probability of finding such a cluster inside the bulk is $P(\ell) \propto p^{b\ell}$, where $b > 0$ is a constant with dimensions of the inverse of length and p is the probability of finding a single weak bond. A more convenient form of $P(\ell)$ is written as

$$P(\ell) \propto \exp[b \ln(p)\, \ell]. \tag{4.2}$$

To estimate the scaling of the Majorana excitation gap with its linear size ℓ, we assume this island is completely disconnected from the bulk. This simplification allows us the treat the rare regions as a finite cluster of size ℓ and open boundary conditions. For bond-disorder, this assumption is strictly valid in the limit $\delta K/K \to 1$ whereas for spin dilution it is readily realized. In this situation, a finite-size gap appears in the Majorana spectrum $\Delta(\ell) \propto \exp[-a\ell]$, with $a > 0$ another constant. This gap comes from the hybridization of the localized states at the edges of this cluster. Fig. 24(b) shows the scaling of the gap with ℓ in a mono-log scale and the exponential decay is evident, for all flux sectors we studied.

Now we can compute the contribution to the density of states coming from these rare regions as

$$\rho(E) = \int d\ell\, P(\ell)\, \delta(E - \Delta(\ell)) \sim E^{-\alpha}, \tag{4.3}$$

with $\alpha = 1 + (b/a)\ln(p)$. Therefore, weakly coupled clusters give rise to a power-law singularity in the DOS. For even lower temperatures, we eventually flow away from this crossover regime towards the asymptotic regime $\rho(E) \sim \exp\left(-c\,|\ln E|^{2/3}\right)/E$.[45]

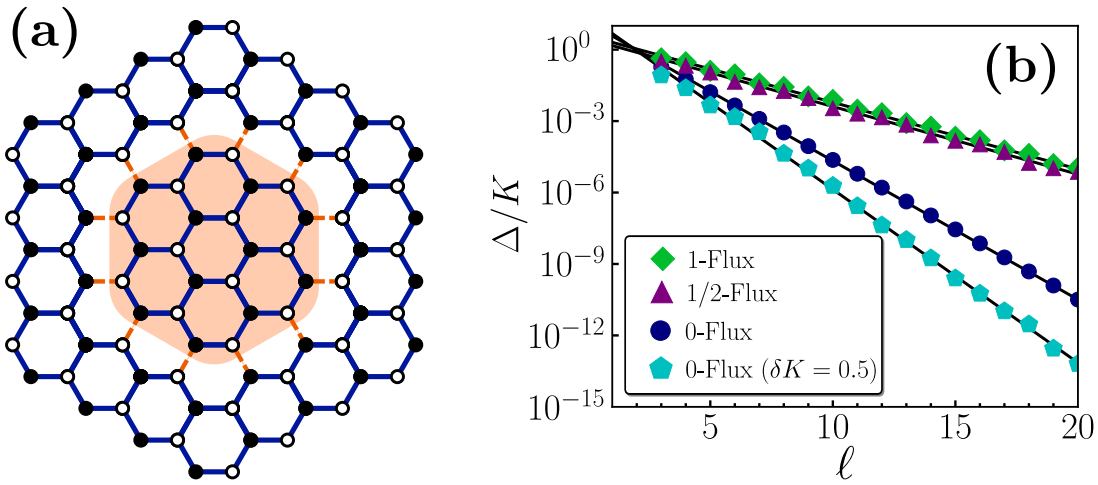

Figure 24 – (a) Sketch of a disorder-induced rare region (shaded area). The dashed orange links represent the weak bonds connecting this droplet to the bulk. (b) Finite-size energy gap Δ for the Kitaev model as a function of the cluster size ℓ considering open boundary conditions. We consider different flux sectors in the clean case. For the disordered case, $\delta K = 0.5$, we show the result for the 0-flux and average over 100 realizations of disorder.
Source: By the author.

The pure Kitaev model displays a phase transition as a function of the exchange anisotropy.[13] In our work, we consider only isotropic Kitaev exchange couplings, but disorder renders them locally anisotropic. For instance, if a given site has two weak bonds and one strong bond it could be locally inside the gapped phase of the pure Kitaev model if $\delta K > K/3$. It is then natural to ask if taking into account disorder inside the rare region would modify our argument qualitatively. We find that this is not the case, with the finite-size energy gap still going exponentially to zero as the size of the rare region is increased, Fig. 24(b). This result points towards the robustness of our argument. We leave an in-depth study of the transition between the two phases in the Kitaev model in the presence of disorder for future work.

4.4.2 The Griffiths-like scenario

Although the power-law derived in Eq.(4.3) is most likely a crossover regime,[45] the fact that it emerges for distinct choices of disorder distributions[41,42] suggests a more general picture. Therefore, we extend this Griffiths phase analogy and calculate the leading low-T contribution to several physical observables in the limit of $T \gg \Delta_{2f}$, such that we can link the spin excitations solely to $\rho(E)$. Such assumption is consistent with our results for the random-flux sector, as $\Delta_{2f} \to 0$.

As a first step to calculate the thermodynamic properties of the system in this Griffiths-like scenario, we estimate the number of free clusters at finite temperature T:

$$n(T) \sim \int_0^T \rho(E)\, dE \sim T^{-\alpha+1}. \tag{4.4}$$

Each free cluster contributes ln(2) to the entropy, which leads to a finite low-T entropy for the spins $S \sim n(T) \ln 2$, with $n(T)$ given by the above expression. Therefore, we can calculate the specific heat as

$$C/T = \frac{\partial S}{\partial T} \propto T^{-\alpha}, \tag{4.5}$$

which is in agreement with the $H_3LiIr_2O_6$ phenomenology, as we discussed in 4.2. Analogously, the uniform spin susceptibility can be estimated from the number of free spins. As the rare regions are basically independent, each of them contributes as a Curie-law to the susceptibility, so we have

$$\chi(T) \sim n(T)/T \sim T^{-\alpha}, \tag{4.6}$$

which eventually overcomes any regular contribution from the bulk. This is again consistent with the $H_3LiIr_2O_6$ observations, and is corroborated by our numerical calculations, Fig.23(a). The imaginary part of the dynamical susceptibility is given by

$$\chi''(\omega) \sim \int \delta(\omega - E)\, \rho(E)\, dE \sim \omega^{-\alpha}. \tag{4.7}$$

Because the cluster excitations are essentially local, we may write the NMR spin-relaxation rate $1/T_1$ as[58] $1/T_1T \sim \chi''(\omega_o)/\omega_o \sim \omega_o^{-\alpha-1}$, where ω_o is the nuclear resonance frequency. Therefore, $1/T_1T$ remains finite down to very low-temperatures, as observed for the random-flux sector, Fig.23(b).

We can also discuss another important result encountered in Ref.,[1] the data scaling of the specific heat as a function of the applied magnetic field B: $C/T \sim B^{-3/2}T$. This scaling law occurs in a regime where $T < B$, which is different to the one considered so far. Nevertheless, it is still interesting to see whether the Griffiths-like scenario is capable to give the experimentally observed scaling for C/T. As T/B is small, we can set $T \sim \Delta_{2f}$ as the low-energy scale in this regime. We then write[13] $\kappa \sim B^3/\Delta_{2f}^2 \sim B^3/T^2$. Because $T \ll \kappa$, we can treat this as a fermionic system, and employ a Sommerfeld-like expansion for the specific heat: $C/T \sim \rho(\kappa)$, where κ plays the role of the Fermi energy E_F. From this, we find the following scaling

$$C/T \sim \kappa^{-\alpha} \sim B^{-3\alpha}T^{2\alpha}, \tag{4.8}$$

where we assumed the DOS to follow the power-law form $\rho \sim E^{-\alpha}$. For $\alpha = 1/2$, we obtain the desired scaling, $C/T \sim B^{-3/2}T$, in agreement with the exponent found in Ref.[1]

Lastly, we can use the rare region argument to explain the non-universality of the power-law exponent, Fig.21(b). As δK increases, the coupling of the rare regions to the bulk is weakened and one may translate this effect into an enhancement of the effective probability of finding a droplet of size ℓ, which accounts for the enhancement of α. In the Majorana language, κ and K_3' correspond to second and third-neighbor hopping,

respectively. Because these longer-range hopping amplitudes are not disordered, they effectively increase the coupling of the rare regions to the bulk and thus decrease α. This is qualitatively similar to the effect of long-range magnetic interactions in the usual Griffiths scenario.[46,48] For $H_3LiIr_2O_6$, it was reported that $\alpha = 1/2$.[1] The Griffiths-like scenario we propose implies that thermodynamics and local dynamics alone are insufficient to conclusively pin down the minimum model for this Kitaev material since α is non-universal. Further crucial information for $H_3LiIr_2O_6$, and other Kitaev materials, comes from their topological properties.

In summary, we conclude that a disordered extension of Kitaev's spin liquid provides a consistent scenario to the experimental results observed in $H_3LiIr_2O_6$, once we combine a power-law low-energy DOS with standard Griffiths-like arguments. However, as we shall see in the next section, such a scenario is incompatible with a topological non-trivial phase, for bond disorder alone, because it requires a random-flux state.

4.5 Topology in the disordered model

4.5.1 Bott Index

For our model, in the presence of bond disorder alone, the power-law behavior in $\rho(E)$ is robust only for the random-flux state. For the 0-flux state, the power-law disappears as we switch on κ because the clean topological gap survives. This automatically implies that the topological phase of the Kitaev model is stable for bond disorder provided the clean gauge sector is preserved, which is true for weak to moderate disorder.

These two fluxes states also manifest differently in the topological properties of the system. To capture a non-trivial topological phase, we compute the topological number via the Bott index formula,[117] as described in Sec.3.3.1. The average Bott index as a function of $\delta K/K$ is presented in Fig.25, for both the 0-flux and the random-flux sectors.

The 0-flux state shows a stable topological phase up to $\delta K \to 1$, as $\mathcal{B}$ is pinned to 1 for all disorder realizations. This is due to the finite topological gap in the Majorana spectrum present in $\rho\,(E)$,[132,137] as we have shown in Fig.21(a). This is similar to what is observed in disordered two-dimensional disordered Chern insulators.[125,129,140,141] In the random-flux state, however, there is a pile-up of low-energy states even for $\delta K = 0$ and the topological phase is trivially destroyed, for all δK. This is more evident if we notice that all curves in Fig.25 for the random-flux depends on the microscopical details of the model, κ and K_3'.

From this perspective, we conclude that disorder on the bonds alone is not capable to destroy the topological phase in the Kitaev model. In contrast, topology is absent in the random-flux in all instances, as previously discussed in Sec.3.3.1.

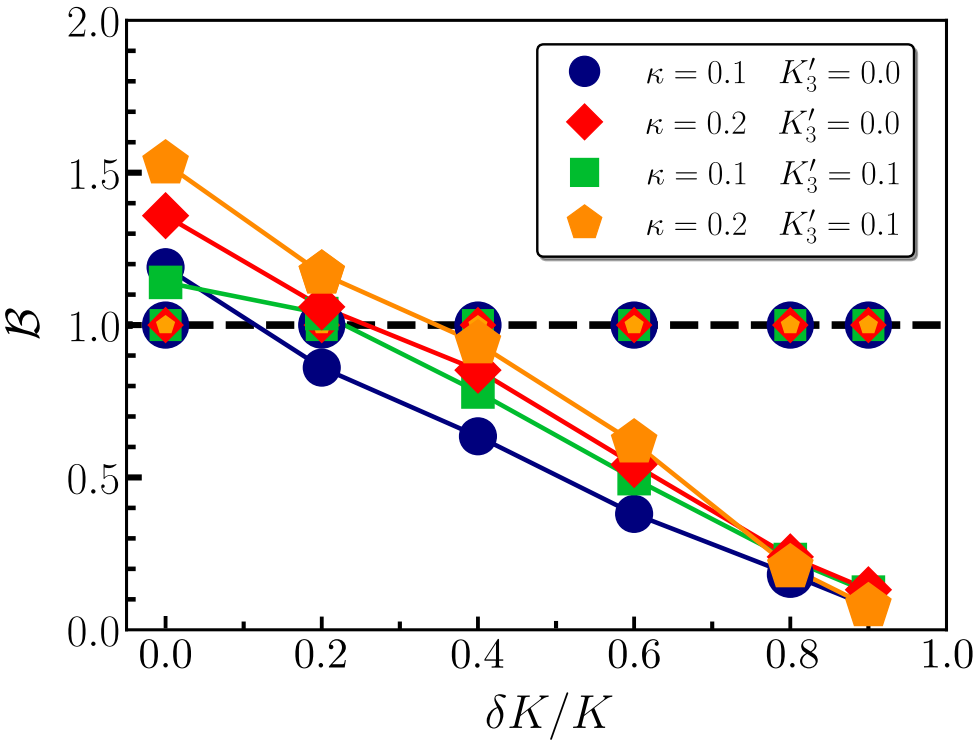

Figure 25 – Average Bott index as a function of disorder. We consider different values of κ and K_3'. The solid lines correspond to the random-flux sector, which is not quantized. The dashed line represents the 0-flux sector, where all points are pinned to $\mathcal{B} = 1$.

Source: By the author.

4.5.2 Level spacing ratio

The robustness of the topological phase in our model reflects not only in a quantized Bott index but also in the level spacing statistics. Here we complement the Bott index results with an investigation of the level spacing statistics,[125,126,131] following the methods described in Sec. 3.3.2. Our results are displayed in Fig. 26 for the 0-flux sector and in Fig. 27 for the random-flux sector.

For the 0-flux we see that $\langle \tilde{r} \rangle$ touches the expected value for GUE statistics just before the topological gap then drops abruptly inside it due to the absence of states in this region (Fig. 26). While putative extended states for higher energies, $E \gtrsim 2K$, are suppressed with the disorder, the extended states close to the gap edge are remarkably robust. We ascribe the shrinking of the topological gap with δK to the levitation and annihilation mechanism first identified in disordered Chern insulators.[140] Fig. 26(b) and (c) exhibits the histogram of $\tilde{r}$ for an extended and a localized state, respectively. As expected, the numerical outcomes are in accordance with the exact GUE and Poisson distributions.

For the random-flux state, the topological gap does not exist and there is no evidence of extended states, except at $E = 0$, which is a special point in the model, even for this gauge sector. We can understand this by connecting our model to the random bipartite

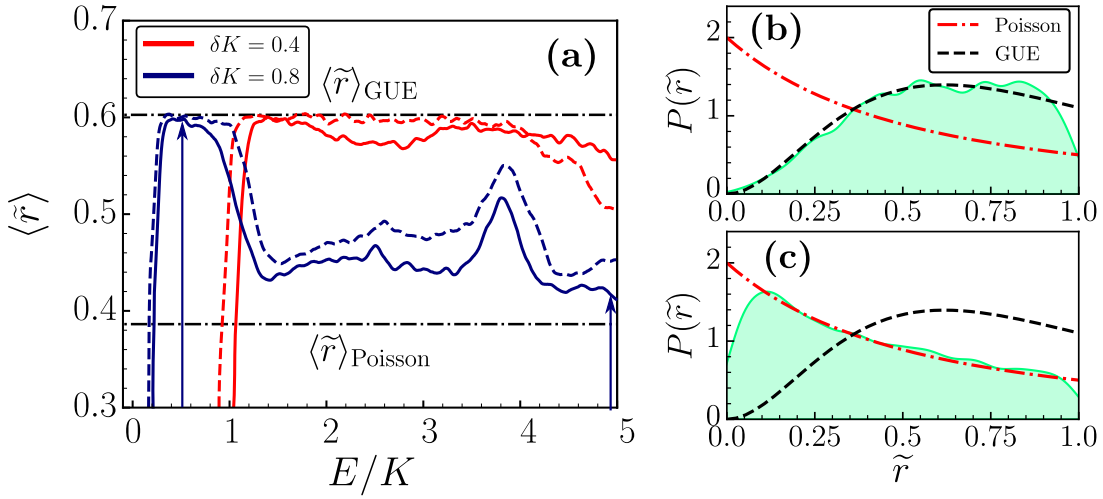

Figure 26 – (a)Average level spacing ratio for the 0-flux sector, with bond disorder as a function of the energy E for $\kappa = 0.2K$ and different values of δK and K_3'. The full and dashed curves correspond to $K_3' = 0.0$ and $K_3' = 0.1$, respectively. (b)-(c) The smooth histogram of $\widetilde{r}$ values at a given energy E. The value is indicated by the arrow on the right for the extended state close to the gap (plot (b)) and on the left for an approximate localized state (plot (c)). We compare the histogram with the exact distributions.

Source: By the author.

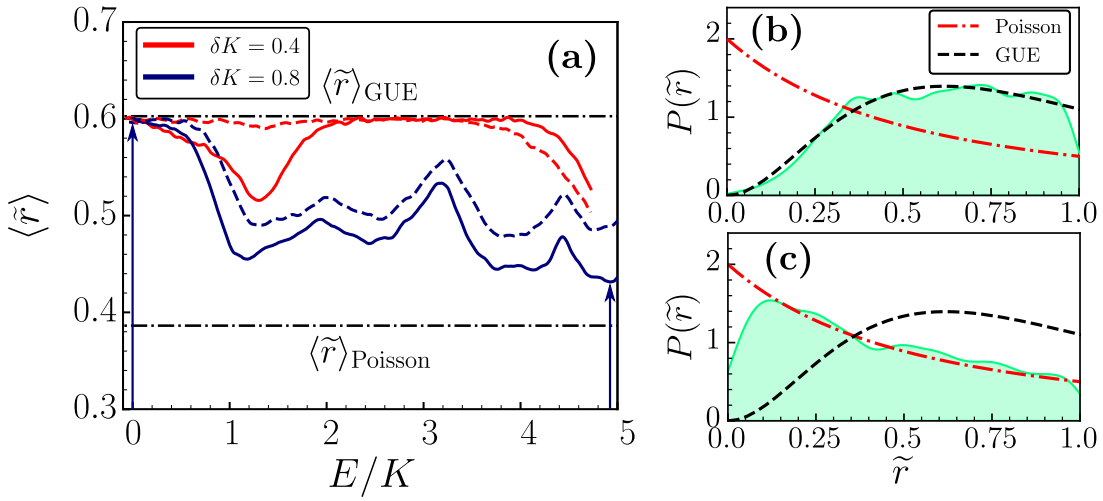

Figure 27 – (a)Average level spacing ratio for the random-flux sector, with bond disorder as a function of the energy E for $\kappa = 0.2K$ and different values of δK and K_3'. The full and dashed curves correspond to $K_3' = 0.0$ and $K_3' = 0.1$, respectively. (b)-(c) The smooth histogram of $\widetilde{r}$ values at a given energy E. The value is indicated by the arrow on the right for the extended state at $E = 0$ (plot (b)) and on the left for an approximate localized state (plot (c)). We compare the histogram with the exact distributions.

Source: By the author.

hopping problem again. For this class of models, it is known that as long as particle-hole symmetry is not broken, there is always a delocalized state at $E = 0$, which does not depend on the disorder strength.[45,142] This is exactly our case, due to the symmetric bond

disorder we consider. Also, we notice that even in the random-flux sector the sublattice symmetry is preserved on average, so the argument still holds.

Lastly, we observe that a large portion of the spectrum touches the GUE statistics, even in the random flux state. This is most likely a finite-size effect, where the correlation length is of the order of the lattice size L. To confirm this hypothesis, one should employ a finite-size scaling analysis. However, this is beyond the scope of the present work, as our prime intention is to probe the existence of chiral edge modes.

Based on the results presented so far, we construct the following scenario for topology in disordered Kitaev materials. Taking κ to mimic the effects of an external magnetic field, the experimental results observed in $H_3LiIr_2O_6$[1] can be described by the extended Kitaev model, augmented by bond disorder, only if one assumes a random-flux state,[41,42] as we argued in Sec.4.4. This, in turn, implies that power-law singularities at zero fields are associated with a topologically trivial phase in a finite field also displaying power-law singularities, but with a reduced exponent.

5 SITE DILUTION IN THE KITAEV MODEL

We now present the results for the extended Kitaev model in Eq. (2.51) in the presence of vacancies. A vacancy is the absence of a site on the lattice, with all its connections turned off. In practice, this can happen either in its literal sense, by deleting an atom at a given site, or replacing a magnetic ion by a non-magnetic impurity. Here we assume the former limiting case where the site is entirely removed from the lattice.

Therefore, we remove a fraction x of spins from the system and employ the exact diagonalization described in Sec. 3.1. The removal of a site is equivalent to eliminating its correspondent row/column in the Hamiltonian matrix in Eq.(3.1). Hence, by working in this reduced dimensional space, we already eliminate trivial zero modes coming from the deleted sites. In addition, we assume a compensated distribution of vacancies, by removing exactly $xN/2$ spins from each sub-lattice. For the honeycomb lattice an imbalance on this distribution leads to trivial zeros. We will return to this point later, when discussing the low-E properties of the system. After the diagonalization, we compute the same physical quantities considered in the case of bond-disorder and discuss our findings in comparison to the $H_3LiIr_2O_6$ phenomenology.

5.1 Fluxes and ground-state energy

In the same manner as performed in Sec.4.1, we begin with an investigation of the ground state energy as a function of the disorder parameter, in this case, the dilution concentration x. From this analysis, we can select the most favorable flux states, and then calculate the thermodynamic and dynamical quantities of the diluted system.

Here we consider both the 0 and random-flux states, as in the bond-disordered case. In addition to these configurations, we also consider the bound-flux sector.[42,108] As we discussed in Sec.3.1.2, in the limit $x \ll 1$, a vacancy binds a flux to it:[108] as one loops the impurity plaquette $W_p = -1$, Fig. 11(e). It is then natural to inquire whether this configuration is favorable as we increase the dilution concentration, and also as we change the parameters κ and K_3'. In Fig. 28(a) we show the ground-state energy as a function of the vacancy concentration for $\kappa = K_3' = 0$ and $x \lesssim 0.1$. The bound-flux and 0-flux states have very similar energies, with a slight preference towards the bound-flux configuration, thus confirming our expectations. On the other hand, the energy of the random-flux state is not competitive in this range of moderate dilution, in agreement with Ref.[42] Therefore, we can discard this flux state in our subsequent calculations.

In Fig. 28(b) we show the energy difference between the 0-flux and bound-flux states, δE_0, as a function of x for different κ values and $K_3' = 0$. For our parameter range, there is

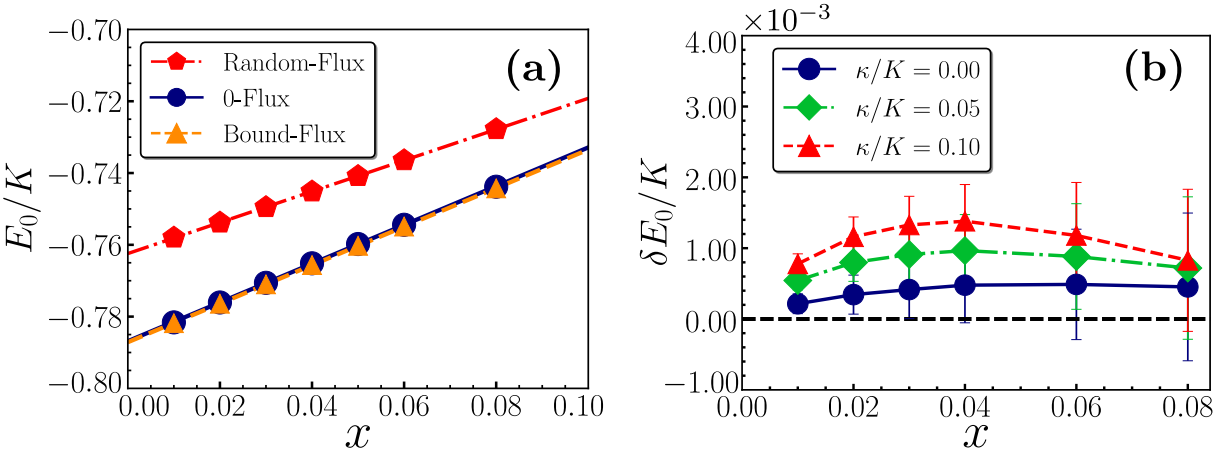

Figure 28 – (a) E_0 as a function of the vacancy concentration x for $\kappa = K_3' = 0$. (b) Difference between the ground state energy of the 0-flux and bound-flux sectors, δE_0 as a function of x for $K_3' = 0$ and three values of κ. We considered $L = 30$ and up to 3×10^3 disorder realizations.
Source: By the author.

no change in the ground-state as a function of κ, suggesting the bound-flux as the ground state for $x \lesssim 0.1$. This result remains the same for finite values of K_3'. Notwithstanding, the energy difference between the two fluxes is rather small, $\delta E_0 \sim 10^{-3}K$, regardless of the parameter values. For this reason, we consider both the 0 and bound-flux sectors as equally competitive states.

5.2 Results for the DOS

In this section, we discuss the fate of the DOS in the diluted Kitaev model, following the numerical procedure described in Sec.3.2.1. From the ground state results presented in the previous section, we select only the 0-flux and the bound-flux states to perform our calculations.

The generic effects of vacancies in fermionic systems on the honeycomb lattice have already been studied in several different contexts,[142–146] and it is well-known that site dilution tends to have a strong impact on the low-E DOS. This is indeed what happens for the Kitaev honeycomb model, as verified in the recent work by Kao *et al.*,[42] where a power-law distribution in the low-E DOS was found, in agreement with the $H_3LiIr_2O_6$ results.[1] Here, we put forward a similar analysis for the extended model in Eq.2.51, where we observe some of the basic features reported in Ref.[42]

In Fig. 29(a) we show the the averaged DOS for $\kappa = K_3' = 0$ for different values of dilution x. The curves for both flux sectors are similar, so we choose to show the bound-flux only. Unlike the bond disordered case, a small dilution is sufficient to induce a pile-up of low-energy states, similar to what is observed in graphene,[142–145] independently of the flux sector.[42] In Fig. 29(b) we plot the low-energy part of the DOS, highlighting

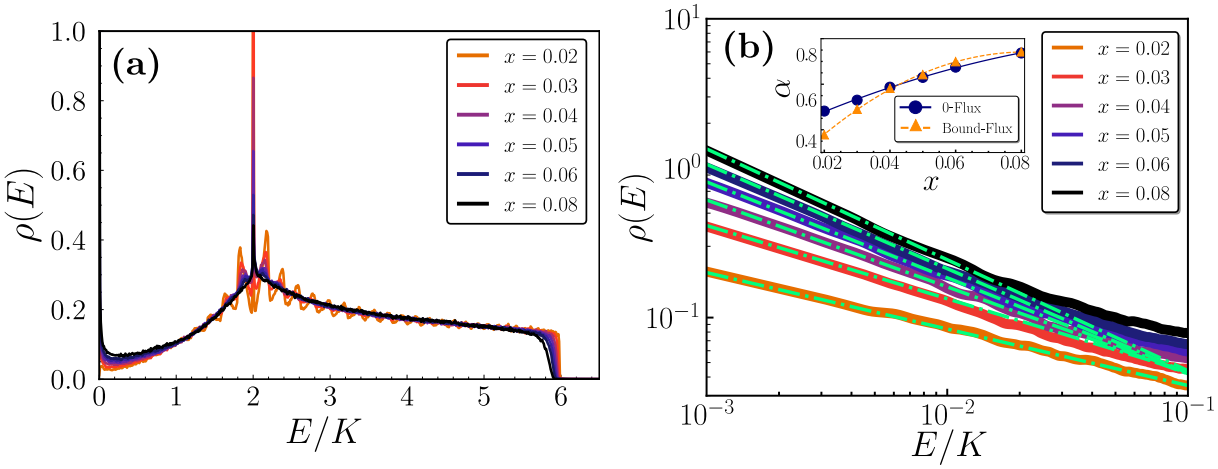

Figure 29 – (a) The average density of states for several values of vacancy concentration x in the bound-flux sector. For $E/K \gtrsim 1$ the DOS resembles very much the clean limit. In the low-E limit, we observe a power-law behavior. (b)Low-energy behavior of the density of states in a log-log plot. The dot-dashed lines are power-law fits to the data. Inset: Non-universal power-law exponent α as a function of x both for the 0-flux and bound-flux sectors. We consider $\kappa = K_3' = 0$, $L = 30$, and 10^3 disorder realizations.
Source: By the author.

its power-law behavior for the bound-flux sector. The inset shows α as a function of the vacancy concentration x for both the bound-flux sector and the 0-flux sector. The behavior in both cases is similar to the one in Fig. 21(b): α increases with x because the larger the dilution, the larger are the odds of constructing a droplet of linear size ℓ disconnected from the bulk. Similarly, we find that α is suppressed with longer range hopping.

A clearer distinction between the different gauge sectors emerges for $\kappa \neq 0$. In Fig. 30 we show the DOS for the 0-flux(a) and the bound-flux(b) sectors, with $\kappa = 0.1K$, $K_3' = 0$, and several values of dilution x. In the 0-flux sector, the DOS value abruptly drops close to the field gap in the clean case, $\Delta_\kappa \sim \kappa$. However, we observe that vacancies induce a pile-up of low-energy states inside this gap, so we have a pronounced power-law divergence as in the $\kappa = 0$ case. In contrast, the bound-flux sector displays a more intricate structure in its low-E DOS. For $x \lesssim 0.05$ we observe a localized level inside the clean gap, at $E/K \approx 0.82$. This state is clearly separated from the DOS peak at $E = 0$, and the larger the κ, the more well-defined this state is. As we increase x we reduce the impurity distance – its typical value scales as $1/\sqrt{x}$ – enhancing the overlap between these localized states which gives rise to an "impurity band" inside the clean topological gap,[42] similar to what is observed in disordered Chern insulators.[125,129,140] The resulting DOS then displays a power-law singularity, as shown in the inset of Fig. 30(b). As we shall see in the next sections, this discrepancy between the two flux sectors plays a major role in the fate of the chiral edge modes in the diluted system.

As a final remark, we comment on the possible effects an imbalanced distribution

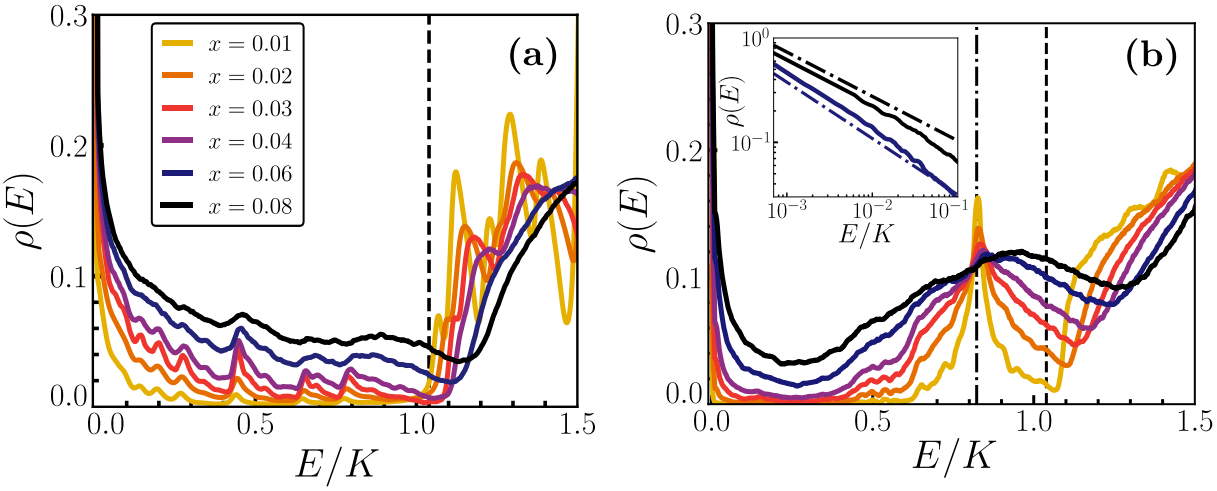

Figure 30 – DOS as function of the energy for the 0-flux(a) and bound-flux(b) sectors, with $\kappa = 0.1K$, $K_3' = 0$ and several values of vacancy concentration x. The dashed line indicates the topological gap Δ_κ in the clean limit. The dot-dashed line in (b) shows the localized level inside the gap. Inset(b): log-log plot showing the power-law divergence at low-E for $x \geq 0.06$. The dot-dashed curves are fits assuming a power-law singularity, which are shifted for the sake of presentation.
Source: By the author.

of vacancies can have on our results. As already mentioned, we assumed a compensated distribution of vacancies, where the number of removed sites on each sublattice is given by $N_A = N_B = xN/2$. One can argue that a more careful analysis should take into account realizations with an imbalanced distribution of vacancies, where $N_A \geqslant N_B$ and vice-versa. For such imbalance, we always have a number $N_I = |N_A - N_B|$ of zero modes,[3] which can potentially alter the low-E DOS. However, this conclusion is only true for single realizations of disorder. If we diagonalize several samples without any constraint, the average number of sites on each sublattice is equal. This consequently results in the same average DOS as plotted in Fig. 29 and Fig. 30.

However, it is important to notice that a *local* imbalance of sites is still possible, even in the equally distributed case. As pointed out by Refs.,[142,147] there exists a special type of rare region on bipartite lattices, dubbed as $\mathcal{R}$-type region. This consists of a droplet where its boundary is made up of sites belonging to only one sublattice. Therefore, such a subsystem must contain a number of zero modes proportional to its local sublattice imbalance. The $\mathcal{R}$-type regions contribute to the DOS peak at $E = 0$ regardless of the flux sector, but we did not weight their individual contribution.

5.3 Results for the spin susceptibility

For the site dilution case, there are two contributions to Δ_{2f} coming from the paired and unpaired spins.[133] An unpaired spin is located in a site that misses one bond

due to the dilution of the nearest neighbor, as illustrated in Fig.31(a). For the paired spins, we have Δ_{2f} finite and slowly diminishing with the dilution x, Fig. 31(b). For the unpaired spins, $\Delta_{2f} = 0$ by definition since there is no bond to flip. For $x \leq 0.1$, we observe a fraction of x unpaired spins, and $(1-x)$ of paired spins. We also have orphan spins in our system, spins missing all their nearest neighbors. In the current model, they are of order $\mathcal{O}(10^{-3}x)$, which implies that their contribution to the physical observables is negligible in the experimentally relevant temperature range.

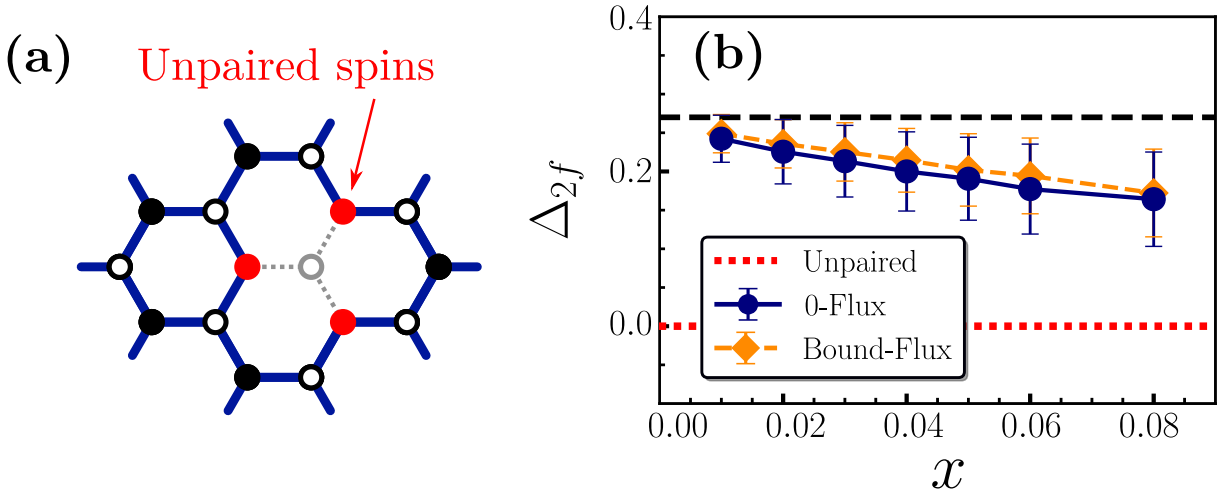

Figure 31 – (a) The unpaired spins around a vacancy. By removing a site (in gray), we automatically leave its three nearest neighbors disconnected along one bond (dashed lines). (b) The flux pair gap Δ_{2f} as a function of x for $\kappa = K_3' = 0$. The dashed line corresponds to its clean value, $\Delta_{2f} \approx 0.27K$. $\Delta_{2f} = 0$ for the unpaired spins. We considered $L = 30$ and 3×10^3 realizations of disorder.
Source: By the author.

As we have already emphasized, all qualitative features of the spin susceptibility and the NMR relaxation rate in the adiabatic approximation can be traced back to the flux pair gap. Therefore, before we show the results for the dynamical quantities, it is useful to make some predictions using the results for Δ_{2f}. If we ignore the contribution from the orphan spins, the NMR relaxation rate can be simply expressed as the weighted sum of the paired and unpaired contributions: $1/T_1 = 1/T_1^{\text{par}}(1-x) + 1/T_1^{\text{unp}}\, x$. Because the paired spins are gapped (Fig.31(b)), they contribute as an exponential decay, while the gapless unpaired spins have a constant relaxation rate. Therefore, we have the following qualitative form of $1/T_1$ in the presence of vacancies

$$\frac{1}{T_1} \propto (1-x)e^{-\Delta_{2f}/T} + x. \tag{5.1}$$

From this expression, it is evident that we still have a constant $1/T_1$ at a very low-T regime, where the unpaired spins dominate, independently of the flux state.

The spin susceptibility can be estimated in the exact same way, by taking the separate contributions from paired and unpaired spins: $\chi(T) = (1-x)\chi^{\text{par}}(T) + x\chi^{\text{unp}}(T)$.

Again, each term contributes differently, depending on whether Δ_{2f} is gapped or not. Therefore, we write the static susceptibility as

$$\chi(T) \propto (1-x)\frac{1}{\Delta_{2f}} + x\, T^{-\alpha}, \tag{5.2}$$

where we have already assumed the power-law singularity for the $\Delta_{2f} = 0$ case, as in the bond-disordered case. From this expression, we expect a divergence to appear at the very low-T regime. In order to verify if the spin susceptibility follows this qualitative analysis, we perform a full numerical computation of $\chi(T)$.

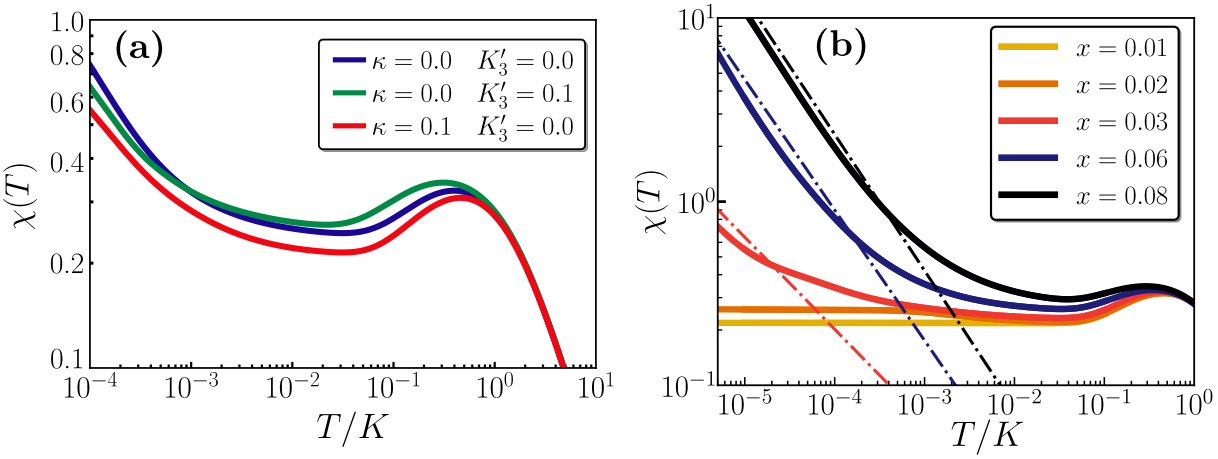

Figure 32 – (a) Static uniform spin susceptibility as a function of the temperature in the bound-flux sector for $x = 0.04$. We use a log-log plot scale. (b) Low-temperature part of the uniform susceptibility $\chi(T)$ as a function of the temperature T in a log-log plot for several values of vacancy concentration x in the bound-flux sector. We consider $\kappa = K_3' = 0$. The dot-dashed lines are power-law fits to the data, with power coming from Fig. 29(b). For both plots, we consider $L = 30$, and 10^3 disorder realizations.
Source: By the author.

In Fig. 32(a) we show sample results for the static uniform spin susceptibility $\chi\,(T)$. We observe a mild increase in $\chi\,(T)$ for the bound-flux, with similar results for the 0-flux. A bona fide power-law divergence is present only at much lower temperatures. This is more evident in Fig. 32(b), where we show the uniform susceptibility for the bound-flux sector, which behaves as $\chi(T) \sim T^{-\alpha}$ at very low-T. As anticipated, the contribution for this power-law tail comes from the unpaired spins because $\Delta_{2f} = 0$ for these sites, Fig. 31(b). Since the density of unpaired spins increases as x, the singular behavior becomes more pronounced at low-T and larger dilution. In these regimes, it overcomes the regular contribution of the bulk spins. Experimentally, this should translate into a milder divergence of the uniform susceptibility in comparison to the specific heat for moderate values of x and not too low-T, Fig. 32(a). Finally, for the small dilution limit, the overall contribution from unpaired spins is masked by the remaining $1-x$ fraction of bulk spins which give a finite contribution to $\chi\,(T)$ if $T < \Delta_{2f}$. This is also in line with

the Knight shift measurements reported in:[1] spins far away from the defects produce a regular flat contribution to the local spin susceptibility, whereas spins around a vacancy give a singular response.

The results of $\chi(T)$ obtained within the adiabatic approximation agrees well with the expected results based on our Griffiths-like arguments, suggesting this is a satisfactory approach for the problem at hand. In fact, because the condition $\Delta_{2f} = 0$ is automatically satisfied by these unpaired spins, the Griffiths-like scenario discussed previously applies directly here, regardless of the considered static flux background.

As a closing remark, we stress that the asymptotic results for $\chi\,(T)$ calculated in Ref.[108] – $\chi(T) \propto \ln(1/T)$ for the bound-flux and $\chi(T) \propto 1/(T\ln(1/T))$ for the 0-flux – are only relevant for large fields, where the magnetic length is smaller than the typical inter-impurity distance and the single vacancy limit holds.

5.4 Topology in the diluted system

5.4.1 Bott index and level spacing ratio

Now, we calculate the Bott index and the level spacing ratio to verify whether the topological phase in the TRS breaking case survives against the presence of vacancies, following the prescription in Sec. 3.3.1 and Sec. 3.3.2. Before we show the results for $\mathcal{B}$, it is useful to take a closer look at the DOS for $\kappa \neq 0$, Fig. 30. As in the bond disordered case, we can link the power-law behavior in $\rho(E)$ to a trivially topological phase. For $x \leqslant 0.02$ the peak at $E = 0$ is well separated from the gap, for both flux sectors. This may be an indication that the topological phase can survive for a very small concentration of vacancies. However, the bound-flux sector displays a more complex structure in its low-E DOS, where we also observe the presence of a localized in-gap state for small dilutions.

To see the effects of the in-gap states on the topological properties of the system, we compute the Bott index, Fig. 33. In the small κ regime, $\mathcal{B}$ is no longer quantized for the 0-flux gauge for $x > 0.02$, as expected from our results for the DOS. Interestingly, in the bound-flux state $\mathcal{B}$ remains pinned to an integer value for larger values of x, even though the clean topological gap is the same. For small κ we find this critical value to be $x \approx 0.05$, but its exact value can change for moderate or very small values of κ. For larger values of x, we interpret that the loss of quantization in both gauges comes from the emergence of an impurity band inside the clean topological gap, similar to what is observed in disordered Chern insulators.[125,129,140]

As anticipated, this extra robustness of the bound-flux state is rooted in the in-gap state at finite energy shown in Fig. 30(b). Because this is a property of the Majorana spectrum, it should be evident from the level statistics perspective. Therefore, we compute the level spacing ratio for the bound-flux case, as shown in Fig. 34. For $\kappa = 0.05K$ and

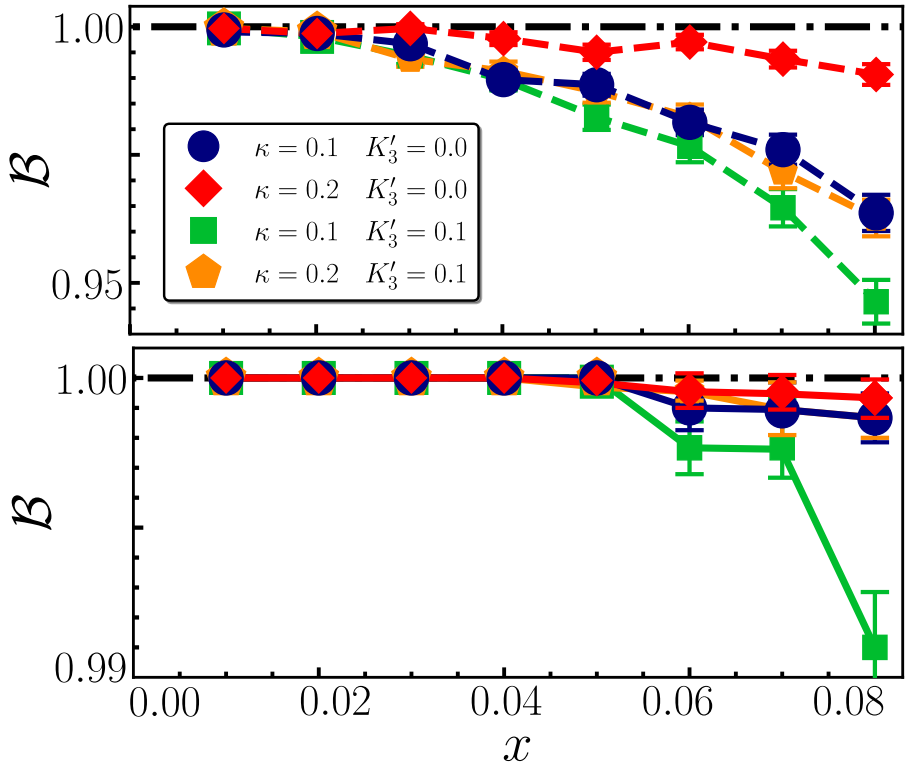

Figure 33 – Bott index as a function of the dilution x, for different values of κ and K_3'. The upper panel corresponds to the 0-flux values (dashed lines), while the bound-flux (solid lines) results are displayed in the lower one.
Source: By the author.

$K_3' = 0.1K$, the energy of the aforementioned localized state is close to the edge of the clean topological gap and the topological phase survives only up to $x \approx 0.03$. For $\kappa = K_3' = 0.1K$, there is a well-defined in-gap state at $E \approx 0.8K$. As the impurity levels move initially into this localized state, there is extra protection and the topological survives up to $x \approx 0.05$.

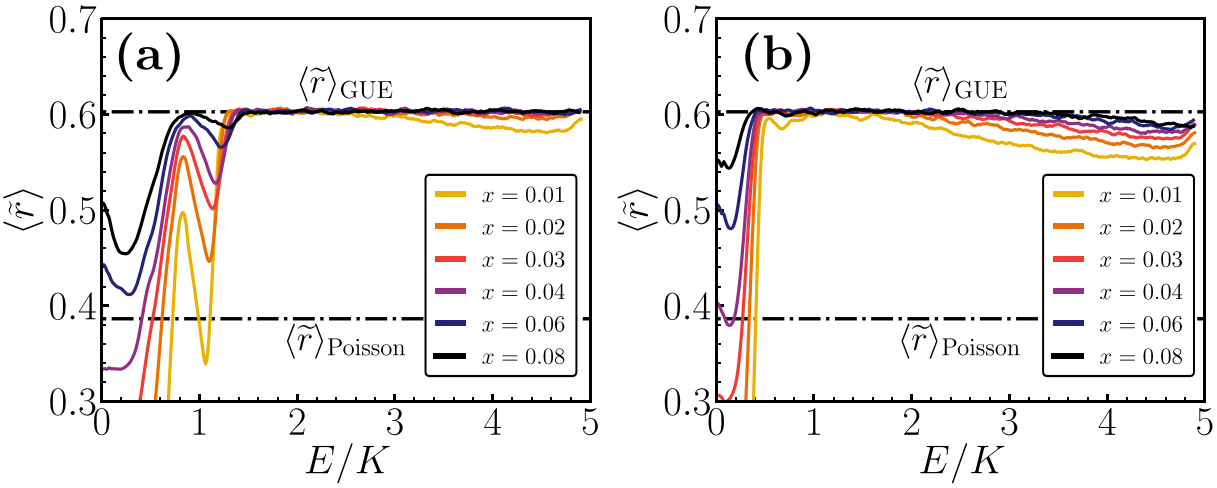

Figure 34 – Average level spacing ratio in the bound-flux state as a function of the energy E for $K_3' = 0.1K$ and several concentrations x. (a) $\kappa = 0.1K$. (b) $\kappa = 0.05K$. We considered $L = 30$ and 3×10^3 realizations of disorder.
Source: By the author.

Contrary to the bond disordered case, we find that in diluted systems there is a window where it is possible to link together the Griffiths-like scenario with a topologically non-trivial phase if we assume the bound-flux sector. The presence of this topological phase might be probed experimentally using the thermal Hall conductance.[36,37,148] Despite being challenging, these measurements could be relevant both to $H_3LiIr_2O_6$[1] and Ir-doped $RuCl_3$.[149]

5.4.2 Majorana Zero Modes

From the Bott index results, complemented with a level statistics analysis, it became clear that the extra robustness for the topological phase in the bound-flux state comes from the fact that each vacancy binds a flux,[108] which creates a localized level inside the clean gap.

To understand the appearance of this in-gap state at finite energies it is sufficient to study the problem of two vacancies placed in an otherwise 0-flux clean background. We set these impurities at a distance $L/2$ apart, but our results are independent of this distance as long as the impurities plaquettes do not share a common link.[42] An impurity plaquette with $l = 12$ sites is shown in Fig. 35(b). We consider two situations: the impurity either binds a flux (bound-flux) or does not (0-flux). We then diagonalize Eq. (2.51) and study its energy spectrum, Fig. 35(a). For the 0-flux state, there is an $E = 0$ state (a Majorana zero mode) whereas for the bound-flux state the impurity energy is gapped. This is the source of extra protection for the topological phase in the bound-flux sector. Interestingly, the gap for the two impurities problem gives precisely the energy of the in-gap state for our full numerics, Fig. 30(b).

The existence of an energy gap in the bound-flux state can be traced back to an even simpler setup. Consider the impurity plaquette as a $l = 12$ tight-binding chain with nearest-neighbor hopping only. The spectrum of this problem has a gap only if the chain binds a flux. This can already be observed from our previous discussion on the bound-flux sector, Eq. 3.10, and more clearly from Fig. 13. For finite x, the impurity states go into this level, ensuring the localization of the impurity states around the vacancy for small x.

As x increases, the diluted impurity picture breaks down. In particular, the probability of finding a pair of neighboring vacancies becomes non-negligible. In this situation, the length of the two-impurity plaquette is $l = 14$, Fig. 35(d). If we study the energies levels of two pairs of neighboring impurities separated by a distance $L/2$, the result is reversed with respect to the single vacancy case: the bound-flux state displays a Majorana zero mode, whereas the 0-flux state shows a gap, Fig. 35(c). Ultimately, the topological phase is destroyed with the increase of dilution for all gauge sectors and we observe $\rho(E) \sim E^{-\alpha}$ at low-E. Nevertheless, the topological phase is particularly robust for the bound-flux state at small x, and increasing κ helps stabilize it. This suggests that a topological phase could

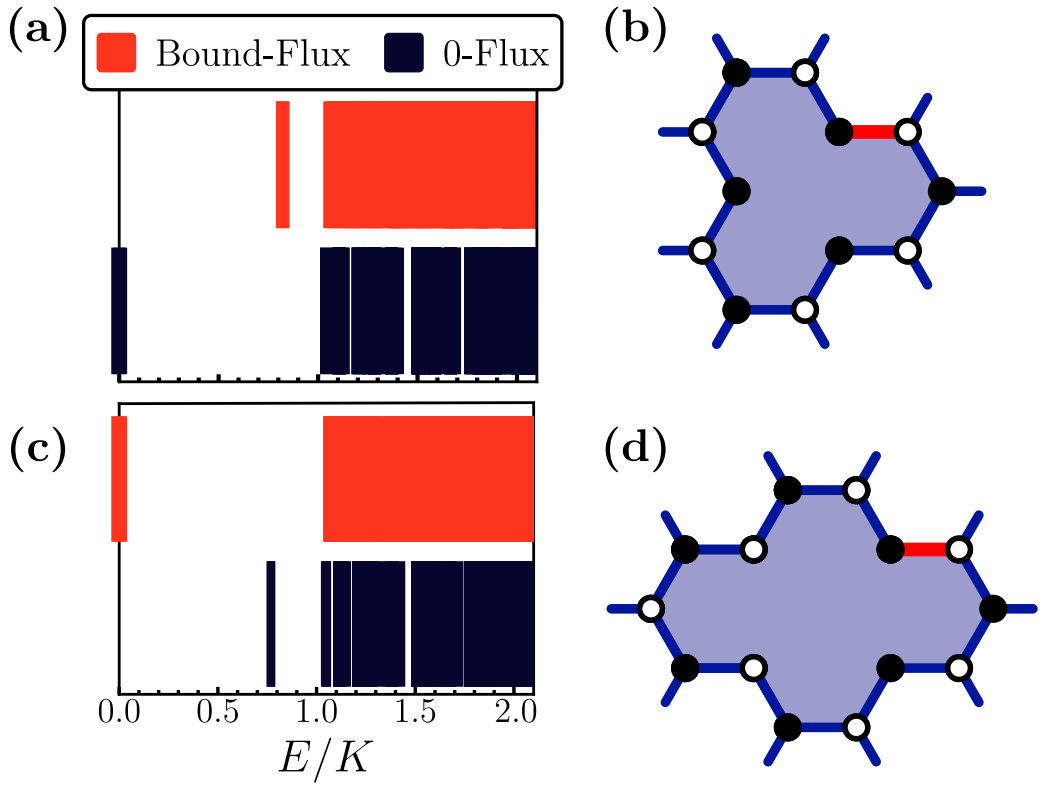

Figure 35 – (a) Energy levels for a system with two vacancies placed at a distance $L/2$ apart. We show the spectrum for the 0-flux and bound-flux states. (b) $l = 12$ plaquette corresponding to a single vacancy. (c) Energy levels for a system with two pairs of neighboring vacancies placed at a distance $L/2$ apart. We show the spectrum for the 0-flux and bound-flux. (d) $l = 14$ plaquette corresponding to a pair of neighboring vacancies. We considered $\kappa = 0.1K$ and $K_3' = 0.0$.
Source: By the author.

be stable in the diluted system for an external field that is large enough to quantize $\mathcal{B}$ for a given x, but not too large as to move the system away from the bound-flux state.[42,108]

As a last remark, we notice that zero modes can also appear from other arrangements, along with the $l = 14$ plaquette in Fig.35(d). This is particularly evident in the high dilution limit, where the formation of larger clusters is more likely to happen. In addition, we can also have zero modes from a local sublattice imbalance, that is, from the $\mathcal{R}$-type regions[142,147] (Sec. 5.2). Ultimately, the stability of the in-gap state renders the topology in the bound flux sector more robust, despite these many contributions to the $E = 0$ state. This non trivial results highlights a general trend: topological phases in interacting systems are more robust than in their non-interacting counterparts.

6 CONCLUSION AND OUTLOOK

In this dissertation, we have investigated an extended Kitaev model in the presence of defects, specifically either bond disorder or site dilution. Our main goal was to understand some of the effects uncorrelated disorder can induce in the Kitaev spin liquid phase. In order to have a broad view of the phenomenology of disordered Kitaev systems, we explored both the thermodynamics and dynamical features of the system, along with an investigation of the interplay of disorder and topology in the presence of an external field.

Following the methodology presented in Chapter 3, we first calculate the physical quantities in the bond disorder case, as shown in Chapter 4. After establishing the random-flux sector as the most competitive state in the strong disorder regime, Sec.4.1, we calculate the DOS and the dynamical quantities. We observe the emergence of a singular power-law density of states at low energies, in accordance with previous works.[41,42] This divergence has a non-universal exponent and it is more pronounced in the random-flux sector, regardless of the values of the microscopic parameters. As we argued in Sec.3.2.1, if one assumes the fluxes to be frozen, we recover the experimentally observed divergence for the specific heat, $C/T \sim T^{-\alpha}$. For the dynamic quantities, we observe a divergence on the static spin susceptibility, $\chi(T) \sim T^{-\alpha}$, with the same power-law as the one observed in the DOS. On the other hand, the NMR relaxation rate is flat at low-T, in agreement with the $H_3LiIr_2O_6$ phenomenology. Both results can be traced back to the vanishing of the flux pair gap in the random-flux configuration and the proliferation of Majorana modes at low-E.

We then construct a phenomenological scenario for our numerical findings by discussing this power-law distribution of energy scales in terms of a Griffiths-like phase. Our results agree well with the experimental observations for $H_3LiIr_2O_6$.[1] From a theoretical perspective, this unanticipated link deserves further studies because the Griffiths phenomenology also emerges naturally in a random-singlet phase.[50–56] In the absence of disorder, a valence-bond crystal and the Kitaev spin-liquid are separated by a quantum phase transition.[150,151] Our work points towards an interesting evolution of this critical point with the disorder.

In Chapter 5, we performed the same calculations for another type of disorder, vacancies. As we pointed out in Sec.3.1.2 and Sec.5.1, the most competitive state in the diluted system is the Bound-flux sector, where one flux is attached to each vacancy.[42,108] Because its energy difference with respect to the original ground state is very small, we also considered the 0-flux sector in the subsequent calculations. In this case, the pile-up of low-E states emerges for any dilution x, independent of the flux-sector.[42] Again, the power-law exponent is non-universal, although it shows similar behavior for both fluxes.

Because of the presence of unpaired spins, we observe a mild increase in static susceptibility, where a power-law divergence is present only at much lower temperatures. Finally, we argue that a Griffiths-like argument can also be considered in this case, as the flux gap vanishes for the contribution of the unpaired spin.

In the presence of a time-reversal breaking term, we find that the topological properties of the system are sensitive both to the static flux background and to the particular choice of disorder. For bond-disorder, the power-law singularities are robust only if one assumes a random-flux background, which in turn implies the lack of a topological spin-liquid phase. For small concentrations of vacancies, however, the power-law singularities survive at weak external magnetic fields and are eventually quenched at larger fields, where a topological phase with chiral Majorana edge modes emerges. The stability of this topological phase comes from the fact that a vacancy binds a flux to it, which helps protect the clean topological gap in the Majorana spectrum. We believe our results can impact future theoretical and experimental research, as it indicates that diluted Kitaev materials are good candidates to display Kitaev's chiral spin-liquid phase in the presence of weak to moderate magnetic fields.

We expect our results to hold in the experimentally relevant temperature range not only for $H_3LiIr_2O_6$[1] but also for other diluted Kitaev materials, such as the Iridates.[152,153] However, the scenario constructed in this work is not the final tale of diluted Kitaev materials. For instance, a recent experiment on the diluted $RuCl_3$ showed that C/T and $\chi(T)$ diverge with different exponents, and no scaling on C/T was found.[149] Therefore, further theoretical investigations on the effects of disorder on Kitaev materials are required. One possible path would be to consider the effects of perturbations beyond the integrable point. In this case, a mean-field approach could be employed, along with more powerful numerical techniques, such as Monte-Carlo methods.[38,39,102,132,133] It is also promising to investigate the dynamics of the flux background,[154,155] and how it evolves with disorder. Because the key experimental probe to capture topology is the thermal Hall effect, a great deal of effort has been devoted to understand the phonon contribution to the thermal transport and the interplay between phonons and Majoranas.[156–159] Ultimately, this is a problem which will be explored in great detail in the coming future. On the experimental side there is the need of ever better samples and more precise measurements at low-T. On the theory side, the ultimate goal is to determine a minimal model that captures the key physics of disordered Kitaev QSL.

REFERENCES

1 KITAGAWA, K. *et al.* A spin–orbital-entangled quantum liquid on a honeycomb lattice. **Nature**, v. 554, n. 7692, p. 341–345, 2018. DOI: 10.1038/nature25482.

2 WITCZAK-KREMPA, W. *et al.* Correlated quantum phenomena in the strong spin-orbit regime. **Annual Review of Condensed Matter Physics**, v. 5, n. 1, p. 57, 2014. DOI: 10.1146/annurev-conmatphys-020911-125138.

3 MOESSNER, R.; MOORE, J. E. **Topological phases of matter**. Cambridge: Cambridge University Press, 2021.

4 TREBST, S.; HICKEY, C. Kitaev materials. **Physics Reports**, v. 950, p. 1–37, 2022. DOI: 10.1016/j.physrep.2021.11.003.

5 ANDERSON, P. W. Resonating valence bonds: a new kind of insulator? **Materials Research Bulletin**, v. 8, p. 153, 1973.

6 BALENTS, L. Spin liquids in frustrated magnets. **Nature**, v. 464, n. 7286, p. 199 – 208, 2010. DOI: 10.1038/nature08917.

7 KHALIULLIN, G. Orbital order and fluctuations in mott insulators. **Progress of Theoretical Physics Supplement**, v. 160, p. 155, 2005. DOI: 10.1143/PTPS.160.155.

8 NUSSINOV, Z.; BRINK, J. van den. Compass models: theory and physical motivations. **Reviews of Modern Physics**, v. 87, n. 1, p. 1-59, Jan. 2015. DOI:10.1103/RevModPhys.87.1.

9 RAU, J. G.; LEE, E. K.-H.; KEE, H.-Y. Spin-orbit physics giving rise to novel phases in correlated systems: iridates and related materials. **Annual Review of Condensed Matter Physics**, v. 7, n. 1, p. 195–221, 2016. DOI: 10.1146/annurev-conmatphys-031115-011319.

10 NATORI, W. M. H. *et al.* Chiral spin-orbital liquids with nodal lines. **Physical Review Letters**, v. 117, n. 1. p. 017204, July 2016. DOI: 10.1103/PhysRevLett.117.017204.

11 NATORI, W. M. H.; ANDRADE, E. C.; PEREIRA, R. G. SU(4)-symmetric spin-orbital liquids on the hyperhoneycomb lattice. **Physical Review B**, v. 98, n. 19, p. 195113, Nov 2018. DOI: 10.1103/PhysRevB.98.195113.

12 NATORI, W. M. H. *et al.* SU(4) Heisenberg model on the honeycomb lattice with exchange-frustrated perturbations: implications for twistronics and Mott insulators. **Physical Review B**, v. 100, n. 20, p. 205131, Nov 2019. DOI: 10.1103/PhysRevB.100.205131.

13 KITAEV, A. Anyons in an exactly solved model and beyond. **Annals of Physics**, v. 321, n. 1, p. 2-111, 2006. DOI: 10.1016/j.aop.2005.10.005.

14 JACKELI, G.; KHALIULLIN, G. Mott insulators in the strong spin-orbit coupling limit: from Heisenberg to a quantum compass and Kitaev models. **Physical Review Letters**, v. 102, n. 1, p. 017205, 2009. DOI: 10.1103/PhysRevLett.102.017205.

15 CHALOUPKA, J.; JACKELI, G.; KHALIULLIN, G. Kitaev-Heisenberg model on a Honeycomb lattice: possible exotic phases in iridium oxides A_2IrO_3. **Physical Review Letters**, v. 105, n. 2, p. 027204, 2010. DOI: 10.1103/PhysRevLett.105.027204.

16 CHALOUPKA, J.; JACKELI, G.; KHALIULLIN, G. Zigzag magnetic order in the iridium oxide Na_2IrO_3. **Physical Review Letters**, v. 110, n. 9, p. 097204, 2013. DOI: 10.1103/PhysRevLett.110.097204.

17 WINTER, S. M. *et al.* Models and materials for generalized Kitaev magnetism. **Journal of Physics:** condensed matter, v. 29, n. 49, p. 493002, 2017. DOI: 10.1088/1361-648X/aa8cf5.

18 HERMANNS, M.; KIMCHI, I.; KNOLLE, J. Physics of the Kitaev model: fractionalization, dynamic correlations, and material connections. **Annual Review of Condensed Matter Physics**, v. 9, n. 1, p. 17-33, 2018. DOI: 10.1146/annurev-conmatphys-033117-053934.

19 TAKAGI, H. *et al.* Concept and realization of Kitaev quantum spin liquids. **Nature Reviews Physics**, v. 1, n. 4, p. 264–280, 2019. DOI: 10.1038/s42254-019-0038-2.

20 SAVARY, L.; BALENTS, L. Quantum spin liquids: a review. **Reports on Progress in Physics**, v. 80, n. 1, p. 016502, 2017. DOI: 10.1088/0034-4885/80/1/016502.

21 BROHOLM, C. *et al.* Quantum spin liquids. **Science**, v. 367, n. 6475, p. eaay0668, 2020. DOI: 10.1126/science.aay0668.

22 HICKEY, C.; TREBST, S. Emergence of a field-driven U(1) spin liquid in the Kitaev honeycomb model. **Nature Communications**, v. 10, p. 530, 2019. DOI:10.1038/s41467-019-08459-9.

23 CHOI, S. K. *et al.* Spin waves and revised crystal structure of honeycomb iridate Na_2IrO_3. **Physical Review Letters**, v. 108, n. 12, p. 127204, 2012. DOI: 10.1103/PhysRevLett.108.127204.

24 SINGH, Y. *et al.* Relevance of the Heisenberg-Kitaev model for the Honeycomb lattice iridates A_2IrO_3. **Physical Review Letters**, v. 108, n. 12, p. 127203, Mar. 2012. DOI: 10.1103/PhysRevLett.108.127203.

25 PLUMB, K. W. *et al.* α-$RuCl_3$: a spin-orbit assisted Mott insulator on a honeycomb lattice. **Physical Review B**, v. 90, n. 4, p. 041112(R), 2014. DOI: 10.1103/PhysRevB.90.041112.

26 SEARS, J. A. *et al.* Magnetic order in α-$RuCl_3$: a honeycomb-lattice quantum magnet with strong spin-orbit coupling. **Physical Review B**, v. 91, n. 14, p. 144420, 2015. DOI: 10.1103/PhysRevB.91.144420.

27 BANERJEE, A. *et al.* Proximate Kitaev quantum spin liquid behaviour in a honeycomb magnet.. **Nature Materials**, v. 15, p. 733, 2016. DOI: 10.1038/nmat4604.

28 JANSSEN, L.; ANDRADE, E. C.; VOJTA, M. Magnetization processes of zigzag states on the honeycomb lattice: identifying spin models for α-$RuCl_3$ and Na_2IrO_3. **Physical Review B**, v. 96, n. 6, p. 064430, 2017. DOI: 10.1103/PhysRevB.96.064430.

29 CÔNSOLI, P. M. *et al.* Heisenberg-Kitaev model in a magnetic field: $1/S$ expansion. **Physical Review B**, v. 102, p. 155134, Oct. 2020. DOI: 10.1103/PhysRevB.102.155134.

30 SEARS, J. A. *et al.* Phase diagram of α-$RuCl_3$ in an in-plane magnetic field. **Physical Review B**, v. 95, p. 180411(R), May 2017. DOI: 10.1103/PhysRevB.95.180411.

31 WOLTER, A. U. B. *et al.* Field-induced quantum criticality in the Kitaev system α-$RuCl_3$. **Physical Review B**, v. 96, p. 041405(R), July 2017. DOI: 10.1103/PhysRevB.96.041405.

32 KASAHARA, Y. *et al.* Unusual thermal hall effect in a Kitaev spin liquid candidate α-$RuCl_3$. **Physical Review Letters**, v. 120, p. 217205, 2018. DOI: 10.1103/PhysRevLett.120.217205.

33 JANSSEN, L.; VOJTA, M. Heisenberg-Kitaev physics in magnetic fields. **Journal of Physics:** condensed matter, v. 31, n. 42, p. 423002, July 2019. DOI: 10.1088/1361-648x/ab283e.

34 BALZ, C. *et al.* Finite field regime for a quantum spin liquid in α-$RuCl_3$. **Physical Review B**, v. 100, p. 060405(R), Aug. 2019. DOI: 10.1103/PhysRevB.100.060405.

35 GASS, S. *et al.* Field-induced transitions in the Kitaev material α-$RuCl_3$ probed by thermal expansion and magnetostriction. **Physical Review B**, v. 101, p. 245158, June 2020. DOI: 10.1103/PhysRevB.101.245158.

36 KASAHARA, Y. *et al.* Majorana quantization and half-integer thermal quantum hall effect in a Kitaev spin liquid. **Nature**, v. 559, p. 227–231, 2018. DOI: 10.1038/s41586-018-0274-0.

37 YOKOI, T. *et al.* Half-integer quantized anomalous thermal Hall effect in the Kitaev material candidate α-$RuCl_3$. **Science**, v. 373, n. 6554, p. 568 – 572, 2021. DOI: 10.1126/science.aay5551.

38 NASU, J.; UDAGAWA, M.; MOTOME, Y. Vaporization of Kitaev spin liquids. **Physical Review Letters**, v. 113, p. 197205, Nov. 2014. DOI: 10.1103/PhysRevLett.113.197205.

39 NASU, J.; UDAGAWA, M.; MOTOME, Y. Thermal fractionalization of quantum spins in a Kitaev model: temperature-linear specific heat and coherent transport of Majorana fermions. **Physical Review B**, v. 92, p. 115122, Sept. 2015. DOI: 10.1103/PhysRevB.92.115122.

40 FENG, K.; PERKINS, N. B.; BURNELL, F. J. Further insights into the thermodynamics of the Kitaev honeycomb model. **Physical Review B**, v. 102, p. 224402, Dec. 2020. DOI: 10.1103/PhysRevB.102.224402.

41 KNOLLE, J.; MOESSNER, R.; PERKINS, N. B. Bond-disordered spin liquid and the honeycomb iridate $H_3LiIr_2O_6$: abundant low-energy density of states from random majorana hopping. **Physical Review Letters**, v. 122, p. 047202, Feb. 2019. DOI: 10.1103/PhysRevLett.122.047202.

42 KAO, W.-H. *et al.* Vacancy-induced low-energy density of states in the Kitaev spin liquid. **Physical Review X**, v. 11, p. 011034, Feb. 2021. DOI: 10.1103/PhysRevX.11.011034.

43 FREITAS, L. R. D.; PEREIRA, R. G. Gapless excitations in field-induced Kitaev spin liquids with line defects. **Physical Review B**, v. 119, n. 22, p. 227208, 2021. DOI: 10.1103/PhysRevB.105.L041104.

44 VOJTA, T. Rare region effects at classical, quantum and nonequilibrium phase transitions. **Journal of Physics A:** mathematical and general, v. 39, n. 22, p. R143–R205, May 2006. DOI: 10.1088/0305-4470/39/22/r01.

45 MOTRUNICH, O.; DAMLE, K.; HUSE, D. A. Particle-hole symmetric localization in two dimensions. **Physical Review B**, v. 65, p. 064206, Jan. 2002. DOI: 10.1103/PhysRevB.65.064206.

46 MIRANDA, E.; DOBROSAVLJEVIĆ, V. Disorder-driven non-Fermi liquid behaviour of correlated electrons. **Reports on Progress in Physics**, v. 68, n. 10, p. 2337–2408, Aug. 2005. DOI: 10.1088/0034-4885/68/10/r02.

47 ANDRADE, E. C.; MIRANDA, E.; DOBROSAVLJEVIĆ, V. Electronic Griffiths phase of the $d = 2$ Mott transition. **Physical Review Letters**, v. 102, p. 206403, May 2009. DOI: 10.1103/PhysRevLett.102.206403.

48 VOJTA, T. Quantum Griffiths effects and smeared phase transitions in metals: theory and experiment. **Journal of Low Temperature Physics**, v. 161, n. 1, p. 299–323, 2010. DOI: 10.1007/s10909-010-0205-4.

49 VOJTA, T.; HOYOS, J. A. Criticality and quenched disorder: Harris Criterion versus rare regions. **Physical Review Letters**, v. 112, p. 075702, Feb. 2014. DOI: 10.1103/PhysRevLett.112.075702.

50 BHATT, R. N.; LEE, P. A. Scaling studies of highly disordered spin-½ antiferromagnetic systems. **Physical Review Letters**, v. 48, p. 344–347, Feb. 1982. DOI: 10.1103/PhysRevLett.48.344.

51 ZHOU, S. *et al.* Valence-bond theory of highly disordered quantum antiferromagnets. **EPL**, v. 87, n. 2, p. 27003, July 2009. DOI: 10.1209/0295-5075/87/27003.

52 UEMATSU, K.; KAWAMURA, H. Randomness-induced quantum spin liquid behavior in the $s = \frac{1}{2}$ random J_1-J_2 Heisenberg antiferromagnet on the square lattice. **Physical Review B**, v. 98, p. 134427, Oct. 2018. DOI: 10.1103/PhysRevB.98.134427.

53 LIU, L. *et al.* Random-singlet phase in disordered two-dimensional quantum magnets. **Physical Review X**, v. 8, p. 041040, Dec. 2018. DOI: 10.1103/PhysRevX.8.04104.

54 KIMCHI, I.; NAHUM, A.; SENTHIL, T. Valence bonds in Random quantum magnets: theory and application to $YbMgGaO_4$. **Physical Review X**, v. 8, p. 031028, July 2018. DOI: 10.1103/PhysRevX.8.031028.

55 KIMCHI, I. *et al.* Scaling and data collapse from local moments in frustrated disordered quantum spin systems. **Nature Communications**, v. 9, n. 1, p. 4367, 2018. DOI: 10.1038/s41467-018-06800-2.

56 SANYAL, S. *et al.* Emergent moments and Random singlet physics in a Majorana spin liquid. **Physical Review Letters**, v. 127, p. 127201, Sept. 2021. DOI: 10.1103/PhysRevB.78.115116.

57 BASKARAN, G.; SEN, D.; SHANKAR, R. Spin-S Kitaev model: classical ground states, order from disorder, and exact correlation functions. **Physical Review B**, v. 78, p. 115116, Sept. 2008. DOI: 10.1103/PhysRevB.78.115116.

58 COLEMAN, P. **Introduction to many-body physics**. Cambridge: Cambridge University Press, 2015.

59 WEN, X.-G. **Quantum field theory of many-body systems:** from the origin of sound to an origin of light and electrons. Oxford: Oxford University Press, 2004.

60 ZHANG, S.-S.; BATISTA, C. D.; HALÁSZ, G. B. Toward kitaev's sixteen fold way in a honeycomb lattice model. **Physical Review Research**, v. 2, p. 023334, June 2020. DOI: 10.1103/PhysRevResearch.2.023334.

61 LIEB, E. H. Flux phase of the half-filled band. **Physical Review Letters**, v. 73, p. 2158–2161, Oct. 1994. DOI: 10.1103/PhysRevLett.73.2158.

62 NETO, A. H. C. *et al.* The electronic properties of graphene. **Reviews of Modern Physics**, v. 81, p. 109–162, Jan. 2009. DOI: 10.1103/RevModPhys.81.109.

63 KITAEV, A. Y. Fault-tolerant quantum computation by anyons. **Annals of Physics**, v. 303, n. 1, p. 2–30, 2003. DOI: 10.1016/S0003-4916(02)00018-0.

64 KNOLLE, J. *et al.* Dynamics of a two-dimensional quantum spin liquid: signatures of emergent Majorana Fermions and fluxes. **Physical Review Letters**, v. 112, p. 207203, May 2014. DOI: 10.1103/PhysRevLett.112.207203.

65 KNOLLE, J. *et al.* Dynamics of fractionalization in quantum spin liquids. **Physical Review B**, v. 92, p. 115127, Sept. 2015. DOI: 10.1103/PhysRevB.92.115127.

66 BASKARAN, G.; MANDAL, S.; SHANKAR, R. Exact results for spin dynamics and fractionalization in the Kitaev model. **Physical Review Letters**, v. 98, p. 247201, June 2007. DOI: 10.1103/PhysRevLett.98.247201.

67 SACHDEV, S. **Quantum phase transitions**. Cambridge: Cambridge University Press, 2011.

68 HERMANNS, M.; O'BRIEN, K.; TREBST, S. Weyl spin liquids. **Physical Review Letters**, v. 114, p. 157202, Apr. 2015. DOI: 10.1103/PhysRevLett.114.157202.

69 MENG, Z. *et al.* Quantum spin liquid emerging in two-dimensional correlated Dirac Fermions. **Nature**, v. 464, n. 7290, p. 847–851, 2010. DOI: 10.1038/nature08942.

70 HALDANE, F. D. M. Model for a quantum hall effect without landau levels: condensed-matter realization of the "parity anomaly". **Physical Review Letters**, v. 61, p. 2015–2018, Oct. 1988. DOI: 10.1103/PhysRevLett.61.2015.

71 ALTLAND, A.; ZIRNBAUER, M. R. Nonstandard symmetry classes in mesoscopic normal-superconducting hybrid structures. **Physical Review B**, v. 55, p. 1142–1161, Jan. 1997. DOI: 10.1103/ PhysRevB.55.1142.

72 CHIU, C.-K. *et al.* Classification of topological quantum matter with symmetries. **Reviews of Modern Physics**, v. 88, p. 035005, Aug. 2016. DOI: 10.1103/RevModPhys.88.035005.

73 NAYAK, C. *et al.* Non-abelian anyons and topological quantum computation. **Reviews of Modern Physics**, v. 80, p. 1083–1159, Sept. 2008. DOI: 10.1103/RevModPhys.80.1083.

74 THOULESS, D. J. *et al.* Quantized hall conductance in a two-dimensional periodic potential. **Physical Review Letters**, v. 49, p. 405–408, Aug. 1982. DOI: 10.1103/PhysRevLett.49.405.

75 BERRY, M. V. Quantal phase factors accompanying adiabatic changes. **Proceedings of the Royal Society of London A**: mathematical and physical sciences, v. 392, n. 1802, p. 45–57, 1984.

76 NAKAHARA, M. **Geometry, topology and physics**. Boca Raton: CRC Press, 2018.

77 HASAN, M. Z.; KANE, C. L. Colloquium: topological insulators. **Reviews of Modern Physics**, v. 82, n. 4, p. 3045, 2010. DOI: 10.1103/RevModPhys.82.3045.

78 MOTOME, Y.; NASU, J. Hunting majorana fermions in kitaev magnets. **Journal of the Physical Society of Japan**, v. 89, n. 1, p. 012002, 2020. DOI: 10.7566/JPSJ.89.012002.

79 ALICEA, J. New directions in the pursuit of majorana fermions in solid state systems. **Reports on Progress in Physics**,v. 75, n. 7, p. 076501, 2012. DOI: 10.1088/0034-4885/75/7/076501/meta.

80 NAYAK, C. *et al.* Non-abelian anyons and topological quantum computation. **Reviews of Modern Physics**, v. 80, n. 3, p. 1083, 2008. DOI: 10.1103/RevModPhys.80.1083.

81 KUGEL, K. I.; KHOMSKII. The Jahn-Teller effect and magnetism: transition metal compounds. **Soviet Physics Uspekhi**, v. 25, n. 4, p. 231, 1982.

82 KHOMSKII, D. **Transition metal compounds**. Cambridge: Cambridge University Press, 2014.

83 TAKAYAMA, T. *et al.* Hyperhoneycomb iridate $\beta-Li_2IrO_3$ as a platform for Kitaev magnetism. **Physical Review Letters**, v. 114, n. 7, p. 077202, 2015. DOI: 10.1103/PhysRevLett.114.077202.

84 RAU, J. G.; LEE, E. K.-H.; KEE, H.-Y. Generic spin model for the honeycomb iridates beyond the Kitaev limit. **Physical Review Letters**, v. 112, p. 077204, Feb. 2014. DOI: 10.1103/PhysRevLett.112.077204.

85 RAU, J. G.; KEE, H.-Y. **Trigonal distortion in the honeycomb iridates:** proximity of zigzag and spiral phases in Na_2IrO_3. Available from: https://arxiv.org/pdf/1408.4811.pdf. Accessible at: 23 Jan. 2021.

86 GOTFRYD, D. *et al.* Phase diagram and spin correlations of the Kitaev-Heisenberg model: importance of quantum effects. **Physical Review B**, v. 95, p. 024426, Jan. 2017. DOI: 10.1103/PhysRevB.95.024426.

87 GOHLKE, M.; MOESSNER, R.; POLLMANN, F. Dynamical and topological properties of the Kitaev model in a [111] magnetic field. **Physical Review B**, v. 98, p. 014418, July 2018. DOI: 10.1103/PhysRevB.98.014418.

88 JOHNSON, R. D. *et al.* Monoclinic crystal structure of α-$RuCl_3$ and the zigzag antiferromagnetic ground state. **Physical Review B**, v. 92, p. 235119, Dec. 2015. DOI: 10.1103/PhysRevB.92.235119.

89 SINGH, Y.; GEGENWART, P. Antiferromagnetic Mott insulating state in single crystals of the honeycomb lattice material na_2iro_3. **Physical Review B**, v. 82, p. 064412, Aug. 2010. DOI: 10.1103/PhysRevB.82.064412.

90 BANERJEE, A. *et al.* Excitations in the field-induced quantum spin liquid state of $\alpha-RuCl_3$. **npj Quantum Materials**, v. 3, n. 1, p. 1–7, 2018.

91 WANG, Z. *et al.* Magnetic excitations and continuum of a possibly field-induced quantum spin liquid in $\alpha-RuCl_3$. **Physical Review Letters**, v. 119, n. 22, p. 227202, 2017. DOI: 10.1103/PhysRevLett.119.227202.

92 KAO, W.-H.; PERKINS, N. B. Disorder upon disorder: localization effects in the kitaev spin liquid. **Annals of Physics**, v. 435, p. 168506, 2021. DOI: 10.1016/j.aop.2021.168506.

93 SLAGLE, K. *et al.* Theory of a quantum spin liquid in the hydrogen-intercalated honeycomb iridate $H_3LiIr_2O_6$. **Physical Review B**, v. 97, n. 11, p. 115159, 2018. DOI: 10.1103/PhysRevB.97.115159.

94 LI, Y.; WINTER, S. M.; VALENTÍ, R. Role of hydrogen in the spin-orbital-entangled quantum liquid candidate $H_3LiIr_2O_6$. **Physical Review Letters**, v. 121, n. 24, p. 247202, 2018. DOI: 10.1103/PhysRevLett.121.247202.

95 RONQUILLO, D. C.; VENGAL, A.; TRIVEDI, N. Signatures of magnetic-field-driven quantum phase transitions in the entanglement entropy and spin dynamics of the Kitaev honeycomb model. **Physical Review B**, v. 99, p. 140413, Apr. 2019. DOI: 10.1103/PhysRevB.99.140413.

96 GOHLKE, M. *et al.* Dynamics of the Kitaev-Heisenberg Model. **Physical Review Letters**, v. 119, p. 157203, Oct. 2017. DOI: 10.1103/PhysRevLett.119.157203.

97 SHINJO, K.; SOTA, S.; TOHYAMA, T. Density-matrix renormalization group study of the extended kitaev-Heisenberg model. **Physical Review B**, v. 91, n. 5, p. 054401, 2015. DOI: 10.1103/PhysRevB.91.054401.

98 IREGUI, J. O.; CORBOZ, P.; TROYER, M. Probing the stability of the spin-liquid phases in the Kitaev-Heisenberg model using tensor network algorithms. **Physical Review B**, v. 90, p. 195102, Nov. 2014. DOI: 10.1103/PhysRevB.90.195102.

99 LEE, H.-Y. *et al.* Magnetic field induced quantum phases in a tensor network study of Kitaev magnets. **Nature Communications**, v. 11, n. 1, p. 1–7, 2020. DOI: 10.1038/s41467-020-15320-x.

100 LIU, K. *et al.* Revealing the phase diagram of Kitaev materials by machine learning: cooperation and competition between spin liquids. **Physical Review Research**, v. 3, n. 2, p. 023016, 2021. DOI: 10.1103/PhysRevResearch.3.023016.

101 RAO, N. *et al.* Machine-learned phase diagrams of generalized Kitaev honeycomb magnets. **Physical Review Research**, v. 3, n. 3, p. 033223, 2021. DOI: 10.1103/PhysRevResearch.3.033223.

102 YOSHITAKE, J. *et al.* Majorana dynamical mean-field study of spin dynamics at finite temperatures in the honeycomb kitaev model. **Physical Review B**, v. 96, n. 2, p. 024438, 2017. DOI: 10.1103/PhysRevB.96.024438.

103 WANG, J. *et al.* Multinode quantum spin liquids on the honeycomb lattice. **Physical Review B**, v. 102, n. 14, p. 144427, 2020. DOI: 10.1103/PhysRevB.102.144427.

104 SONG, X.-Y.; YOU, Y.-Z.; BALENTS, L. Low-energy spin dynamics of the honeycomb spin liquid beyond the Kitaev limit. **Physical Review Letters**, v. 117, p. 037209, July 2016. DOI: 10.1103/PhysRevLett.117.037209.

105 ZHANG, S.-S. *et al.* Vison crystals in an extended Kitaev model on the honeycomb lattice. **Physical Review Letters**, v. 123, p. 057201, July 2019. DOI: 10.1103/PhysRevLett.123.057201.

106 TAKIKAWA, D.; FUJIMOTO, S. Topological phase transition to Abelian Anyon phases due to off-diagonal exchange interaction in the Kitaev spin liquid state. **Physical Review B**, v. 102, p. 174414, Nov. 2020. DOI: 10.1103/PhysRevB.102.174414.

107 BLAIZOT, J.; RIPKA, G. **Quantum theory of finite systems**. Cambridge: MIT Press, 1986.

108 WILLANS, A. J.; CHALKER, J. T.; MOESSNER, R. Disorder in a quantum spin liquid: flux binding and local moment formation. **Physical Review Letters**, v. 104, n. 23, p. 237203, June 2010. DOI: 10.1103/PhysRevLett.104.237203.

109 KOGA, A.; MURAKAMI, Y.; NASU, J. Majorana correlations in the kitaev model with ordered-flux structures. **Physical Review B**, v. 103, p. 214421, June 2021. DOI: 10.1103/PhysRevB.103.214421.

110 LOVESEY, S. W. **Theory of neutron scattering from condensed matter**. Oxford: Clarendon Press, 1984.

111 NOZIÈRES, P.; DOMINICIS, C. T. D. Singularities in the x-ray absorption and emission of metals. III. one-body theory exact solution. **Physical Review**, v. 178, p. 1097–1107, Feb. 1969. DOI: 10.1103/PhysRev.178.1097.

112 OHTAKA, K.; TANABE, Y. Theory of the soft-x-ray edge problem in simple metals: historical survey and recent developments. **Reviews of Modern Physics**, v. 62, p. 929–991, Oct. 1990. DOI: 10.1103/RevModPhys.62.929.

113 ZSCHOCKE, F.; VOJTA, M. Physical states and finite-size effects in Kitaev's honeycomb model: Bond disorder, spin excitations, and NMR line shape. **Physical Review B**, v. 92, p. 014403, July 2015. DOI: 10.1103/PhysRevB.92.014403.

114 CARRETTA, P.; KEREN, A. NMR and μSR in highly frustrated magnets. *In*: LACROIX, C.; MENDELS, P.; MILA, F. (ed.). **Introduction to frustrated magnetism**. Heidelberg: Springer, 2011. p. 79–105.

115 WALSTEDT, R. E. **The NMR probe of high-Tc materials and correlated electron systems**. Berlin: Springer, 2018.

116 WHITE, R. M.; WHITE, R. M.; BAYNE, B. **Quantum theory of magnetism**. Berlin: Springer, 1983. v. 1.

117 HASTINGS, M. B.; LORING, T. A. Topological insulators and C*-algebras: theory and numerical practice. **Annals of Physics**, v. 326, n. 7, p. 1699–1759, 2011. DOI: 10.1016/j.aop.2010.12.013.

118 TONIOLO, D. Time-dependent topological systems: a study of the Bott index. **Physical Review B**, v. 98, p. 235425, Dec. 2018. DOI: 10.1103/PhysRevB.98.235425.

119 GE, Y.; RIGOL, M. Topological phase transitions in finite-size periodically driven translationally invariant systems. **Physical Review A**, v. 96, p. 023610, Aug. 2017. DOI: 10.1103/PhysRevA.96.023610.

120 AGARWALA, A.; SHENOY, V. B. Topological insulators in amorphous systems. **Physical Review Letters**, v. 118, p. 236402, June 2017. DOI: 10.1103/PhysRevLett.118.236402.

121 HUANG, H.; LIU, F. Quantum spin hall effect and spin Bott index in a quasicrystal lattice. **Physical Review Letters**, v. 121, p. 126401, Sept. 2018. DOI: 10.1103/PhysRevLett.121.126401.

122 HASTINGS, M. B.; LORING, T. A. Almost commuting matrices, localized Wannier functions, and the quantum hall effect. **Journal of Mathematical Physics**, v 51, n. 1, p. 015214, 2010.

123 BROUDER, C. *et al.* Exponential localization of Wannier functions in insulators. **Physical Review Letters**, v. 98, p. 046402, Jan. 2007. DOI: 10.1103/PhysRevLett.98.046402.

124 FUCHS, J.-N.; PATIL, S.; VIDAL, J. Parity of Chern numbers in the Kitaev honeycomb model and the sixteen fold way. **Physical Review B**, v. 102, p. 115130, Sept. 2020. DOI: 10.1103/PhysRevB.102.115130.

125 PRODAN, E.; HUGHES, T. L.; BERNEVIG, B. A. Entanglement spectrum of a disordered topological Chern insulator. **Physical Review Letters**, v. 105, p. 115501, Sept. 2010. DOI: 10.1103/ PhysRevLett.105.115501.

126 OGANESYAN, V.; HUSE, D. A. Localization of interacting fermions at high temperature. **Physical Review B**, v. 75, p. 155111, Apr. 2007. DOI: 10.1103/PhysRevB.75.155111.

127 PAL, A.; HUSE, D. A. Many-body localization phase transition. **Physical Review B**, v. 82, p. 174411, Nov. 2010. DOI: 10.1103/PhysRevB.82.174411.

128 CUEVAS, E. *et al.* Level statistics of disordered spin-1/2 systems and materials with localized cooper pairs. **Nature Communications**, v. 3, n. 1, p. 1–7, 2012.

129 CASTRO, E. V.; LÓPEZ-SANCHO, M. P.; VOZMEDIANO, M. A. H. Anderson localization and topological transition in Chern insulators. **Physical Review B**, v. 92, p. 085410, Aug. 2015. DOI: 10.1103/PhysRevB.92.085410.

130 CASTRO, E. V. *et al.* Absence of localization in a class of topological systems. **Physical Review B**, v. 93, p. 245414, June 2016. DOI: 10.1103/PhysRevB.93.245414.

131 ATAS, Y. Y. *et al.* Distribution of the ratio of consecutive level spacings in Random matrix ensembles. **Physical Review Letters**, v. 110, p. 084101, Feb. 2013. DOI: 10.1103/PhysRevLett.110.084101.

132 NASU, J.; MOTOME, Y. Thermodynamic and transport properties in disordered Kitaev models. **Physical Review B**, v. 102, p. 054437, Aug. 2020. DOI: 10.1103/PhysRevB.102.054437.

133 NASU, J.; MOTOME, Y. Spin dynamics in the Kitaev model with disorder: quantum Monte Carlo study of dynamical spin structure factor, magnetic susceptibility, and NMR relaxation rate. **Physical Review B**, v. 104, p. 035116, July 2021. DOI: 10.1103/PhysRevB.104.035116.

134 GADE, R. Anderson localization for sublattice models. **Nuclear Physics B**, v. 398, n. 3, p. 499–515, 1993.

135 MUDRY, C.; RYU, S.; FURUSAKI, A. Density of states for the π-flux state with bipartite real random hopping only: a weak disorder approach. **Physical Review B**, v. 67, p. 064202, Feb. 2003. DOI: 10.1103/PhysRevB.67.064202.

136 KÖNIG, E. *et al.* Metal-insulator transition in two-dimensional Random Fermion systems of chiral symmetry classes. **Physical Review B**, v. 85, n. 19, p. 195130, 2012. DOI: 10.1103/PhysRevB.85.195130.

137 YAMADA, M. G. Anderson–Kitaev spin liquid. **npj Quantum Materials**, v. 5, n. 1, p. 82, 2020. DOI: 10.1038/s41535-020-00285-3.

138 GRIFFITHS, R. B. Nonanalytic behavior above the critical point in a Random ising ferromagnet. **Physical Review Letters**, v. 23, p. 17–19, July 1969. DOI: 10.1103/PhysRevLett.23.17.

139 MCCOY, B. M. Incompleteness of the critical exponent description for ferromagnetic systems containing random impurities. **Physical Review Letters**, v. 23, p. 383–386, Aug. 1969. DOI: 10.1103/PhysRevLett.23.383.

140 ONODA, M.; AVISHAI, Y.; NAGAOSA, N. Localization in a quantum spin hall system. **Physical Review Letters**, v. 98, p. 076802, Feb. 2007. DOI: 10.1103/PhysRevLett.98.076802.

141 GARCÍA, J. H.; COVACI, L.; RAPPOPORT, T. G. Real-space calculation of the conductivity tensor for disordered topological matter. **Physical Review Letters**, v. 114, p. 116602, Mar. 2015. DOI: 10.1103/PhysRevLett.114.116602.

142 SANYAL, S.; DAMLE, K.; MOTRUNICH, O. I. Vacancy-induced low-energy states in undoped graphene. **Physical Review Letters**, v. 117, p. 116806, Sept. 2016. DOI: 10.1103/PhysRevLett.117.116806.

143 PEREIRA, V. M. *et al.* Disorder induced localized states in graphene. **Physical Review Letters**, v. 96, p. 036801, Jan. 2006. DOI: 10.1103/PhysRevLett.96.036801.

144 PEREIRA, V. M.; SANTOS, J. M. B. Lopes dos; NETO, A. H. C. Modeling disorder in graphene. **Physical Review B**, v. 77, p. 115109, Mar. 2008. DOI: 10.1103/PhysRevB.77.115109.

145 HÄFNER, V. *et al.* Density of states in graphene with vacancies: midgap power law and frozen multifractality. **Physical Review Letters**, v. 113, p. 186802, Oct. 2014. DOI: 10.1103/PhysRevLett.113.186802.

146 OSTROVSKY, P. *et al.* Density of states in a two-dimensional chiral metal with vacancies. **Physical Review Letters**, v. 113, n. 18, p. 186803, 2014. DOI: 10.1103/PhysRevLett.113.186803.

147 BHOLA, R. *et al.* Dulmage-Mendelsohn percolation: geometry of maximally-packed dimer models and topologically-protected zero modes on diluted bipartite lattices. 2020. Available from: https://arxiv.org/pdf/2007.04974.pdf. Accessible at: 23 Jan. 2021.

148 CZAJKA, P. *et al.* Oscillations of the thermal conductivity in the spin-liquid state of α-$RuCl_3$. **Nature Physics**, v. 17, n. 8, p. 915–919, 2021. DOI: 10.1038/s41567-021-01243-x.

149 BAEK, S.-H. *et al.* Observation of a random singlet state in a diluted Kitaev honeycomb material. **Physical Review B**, v. 102, p. 094407, Sept. 2020. DOI: 10.1103/PhysRevB.102.094407.

150 VOJTA, M. Frustration and quantum criticality. **Reports on Progress in Physics**, v. 81, n. 6, p. 064501, May 2018. DOI: 10.1088/1361-6633/aab6be.

151 MAJUMDER, M. *et al.* Breakdown of magnetic order in the pressurized Kitaev iridate $\beta-Li_2IrO_3$. **Physical Review Letters**, v. 120, p. 237202, June 2018. DOI: 10.1103/PhysRevLett.120.237202.

152 MANNI, S.; TOKIWA, Y.; GEGENWART, P. Effect of nonmagnetic dilution in the honeycomb-lattice iridates Na_2IrO_3 and Li_2IrO_3. **Physical Review B**, v. 89, p. 241102, June 2014. DOI: 10.1103/PhysRevB.89.241102.

153 ANDRADE, E. C.; VOJTA, M. Magnetism in spin models for depleted honeycomb-lattice iridates: spin-glass order towards percolation. **Physical Review B**, v. 90, p. 205112, Nov. 2014. DOI: 10.1103/PhysRevB.90.205112.

154 ZHANG, S.-S. *et al.* Variational study of the kitaev-Heisenberg-gamma model. **Physical Review B**, v. 104, n. 1, p. 014411, 2021. DOI: 10.1103/PhysRevB.104.014411.

155 ZHANG, S.-S.; HALÁSZ, G. B.; BATISTA, C. D. Theory of the kitaev model in a [111] magnetic field. **Nature Communications**, v. 13, n. 1, p. 1–7, 2022.

156 YE, M.; FERNANDES, R. M.; PERKINS, N. B. Phonon dynamics in the kitaev spin liquid. **Physical Review Research**, v. 2, n. 3, p. 033180, 2020. DOI: 10.1103/PhysRevResearch.2.033180.

157 METAVITSIADIS, A.; BRENIG, W. Phonon renormalization in the kitaev quantum spin liquid. **Physical Review B**, v. 101, n. 3, p. 035103, 2020. DOI: 10.1103/PhysRevB.101.035103.

158 FENG, K.; YE, M.; PERKINS, N. B. Temperature evolution of the phonon dynamics in the kitaev spin liquid. **Physical Review B**, v. 103, n. 21, p. 214416, 2021. DOI: 10.1103/PhysRevB.103.214416.

159 FENG, K.; SWARUP, S.; PERKINS, N. B. Footprints of kitaev spin liquid in the fano lineshape of Raman-active optical phonons. **Physical Review B**, v. 105, n. 12, p. L121108, 2022. DOI: 10.1103/PhysRevB.105.L121108.

160 CLAUSET, A.; SHALIZI, C. R.; NEWMAN, M. E. J. Power-law distributions in empirical data. **SIAM Review**, v. 51, n. 4, p. 661–703, 2009.

Appendix

APPENDIX A – DERIVATION OF THE κ INTERACTION

In this appendix, we present the derivation of effective the 3-spin interaction, (2.30), from a perturbative expansion of the Zeeman term around the 0-flux sector. Such expansion can be obtained by the general method of Green's function. The green function, or resolvent operator, is defined as[58]

$$\hat{\mathcal{G}}(E) = (E - \mathcal{H})^{-1} \tag{A.1}$$

The matrix elements of this operator are conventionally expressed as $(E - E_0 - \Sigma(E))$, where $\Sigma(E)$ is the *self-energy*, and the effective hamiltonian is given by $\mathcal{H}_{\text{eff}} = \mathcal{H}_0 + \Sigma(E)$. Neglecting the dependence of $\Sigma(E)$ on E, we can write down the Dyson series for the self-energy as[58]

$$\Sigma(E_0) = \Pi_0 \left(V + V\mathcal{G}_0'(E_0)V + V\mathcal{G}_0'(E_0)V\mathcal{G}_0'(E_0)V + \dots\right)\Pi_0, \tag{A.2}$$

where Π_0 is the projector to the ground state flux sector, V is the perturbation in (2.29) and $\mathcal{G}_0'(E_0)$ is the Green's function of the excited states of the unperturbed system, given by $(E - \mathcal{H}_0)^{-1}$. Writing this expansion explicitly is a complicated task, and here we use a qualitative argument, in order to avoid lengthy calculations. We assume that all intermediate states involved have an energy $\Delta E \sim \Delta_{2f}$ above the ground state.[13] Then, the unperturbed green function $\mathcal{G}_0'(E_0)$ can be written as

$$\mathcal{G}_0'(E_0) = -\frac{1 - \Pi_0}{\Delta_{2f}}. \tag{A.3}$$

Here the factor $(1 - \Pi_0)$ ensures that $\mathcal{G}_0'(E_0)$ refers only to excited states. With this form of $\mathcal{G}_0'$, we can easily expand the self-energy. The first-order term is

$$H_{\text{eff}}^{(1)} = \Pi_0 V \Pi_0 \tag{A.4}$$

$$= -\Pi_0 \left[\sum_{i,\alpha} h_\alpha \sigma_i^\alpha\right] \Pi_0 = 0. \tag{A.5}$$

This term vanishes since the application of a single spin changes the flux configuration, as discussed in Sec. 2.1.2 (see Fig. 4(b)), and the projector Π_0 is restricted to the 0-flux sector.

The second order term is expanded as

$$H_{\text{eff}}^{(2)} = \Pi_0 V G_0' V \Pi_0 \tag{A.6}$$

$$= -\Pi_0 \left[\sum_{i,\alpha} h_\alpha \sigma_i^\alpha\right] \frac{(1 - \Pi_0)}{\Delta_{2f}} \left[\sum_{j,\beta} h_\beta \sigma_j^\beta\right] \Pi_0 \tag{A.7}$$

$$= -\frac{1}{\Delta_{2f}} \Pi_0 \left[\sum_{i,j;\alpha,\beta} h_\alpha h_\beta \sigma_i^\alpha \sigma_j^\beta\right] \Pi_0 + \frac{1}{\Delta_{2f}} \Pi_0 \left[\sum_{i,\alpha} h_\alpha \sigma_i^\alpha\right] \Pi_0 \left[\sum_{j,\beta} h_\beta \sigma_j^\beta\right] \Pi_0 \tag{A.8}$$

Note that the second term involves the first-order correction, which is zero. Then, the second-order term is proportional to a product of two spins:

$$H_{\text{eff}}^{(2)} = -\frac{1}{\Delta_{2f}}\Pi_0 \left[\sum_{i,j;\alpha,\beta} h_\alpha h_\beta \sigma_i^\alpha \sigma_j^\beta\right] \Pi_0. \tag{A.9}$$

In order to remain in the zero-flux sector, we must destroy the flux pair created by the first spin, by acting with the second one. This situation is only possible if $\alpha = \beta$ and if $i = j$ or i, j are nearest neighbors, as shown in Fig.36.

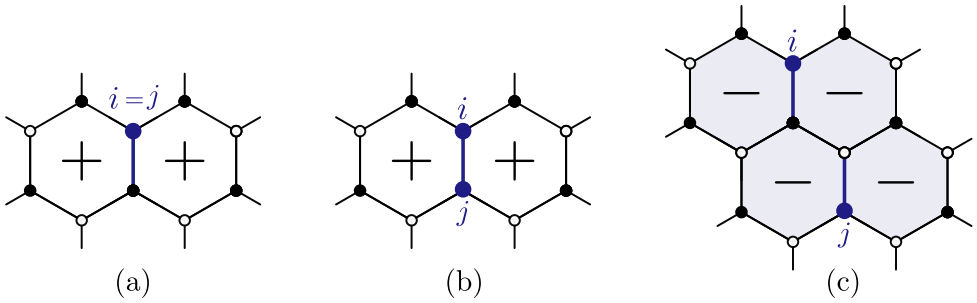

Figure 36 – Three possible contributions from (A.9), with $\alpha = \beta$ (z in this example). In the situations depicted at (a) and (b), the flux pair is created and annihilated right after, preserving the flux configuration. The last case mixes the flux sector and vanishes when we apply the projector Π_0.
Source: By the author.

Thus, the second term is written as

$$H_{\text{eff}}^{(2)} = \frac{1}{\Delta_{2f}} \sum_{\langle i,j\rangle_\alpha} h_\alpha^2 \sigma_i^\alpha \sigma_j^\alpha + \frac{h^2}{\Delta_{2f}} N \tag{A.10}$$

Here $\langle i, j\rangle_\alpha$ indicates nearest neighbors in the α-bond. The second term is originated from the $i = j$ contribution, where we have used $\sigma_i^2 = \mathbb{1}$, and then the sum over the N sites is a constant term. This effective hamiltonian has the exactly same form as the unperturbed Kitaev interaction, and then, its only effect is to renormalize the exchanges, or the hoppings, when working with the Majorana representation, by a factor h_α^2/Δ_{2f}, up to an overall constant.

The first non-trivial term is the third-order one, which is expanded as

$$H_{\text{eff}}^{(3)} = \Pi_0 V \mathcal{G}_0' V \mathcal{G}_0' V \Pi_0 \tag{A.11}$$

$$= \Pi_0 V V V \Pi_0 \tag{A.12}$$

$$= \frac{1}{J^2}\,\Pi_0 \left[\sum_{(\alpha,\beta,\gamma)} \sum_{i,j,k} h_\alpha h_\beta h_\gamma \sigma_i^\alpha \sigma_j^\beta \sigma_k^\gamma\right] \Pi_0, \tag{A.13}$$

where we have ignored all terms involving $\Pi_0 V \Pi_0 = 0$. By applying the first two spins, with $\alpha = \beta$, the possible outcomes are depicted in Fig.36, where we have two pairs of fluxes or no fluxes at all. Then, regardless of the direction γ it is impossible to stay in

the zero-flux sector. The only remaining possibility is $\alpha \neq \beta \neq \gamma$. Finally, we analyze the possible contributions regarding the site indices. After the application of the first two spins, we must have a pair of fluxes to be destroyed by the remaining operator. Therefore, we are left with the two possibilities shown in Fig.5.

APPENDIX B – SOME PROPERTIES OF THE K_3 AND K_3' TERMS

In this appendix, we give some extra details pertaining to the third neighbor hopping terms, K_3 and K_3', introduced in Sec.2.3.3. From Eq.(2.46), the K_3 term is written as the 4-spin Hamiltonian

$$\mathcal{H}_{K_3} = K_3 \sum_{(ijkl)_{\alpha\beta\gamma}} \sigma_i^\alpha \sigma_j^\gamma \sigma_k^\alpha \sigma_l^\gamma, \tag{B.1}$$

with the possible paths $(ijkl)_{\alpha\beta\gamma}$ illustrated in Fig.37(a) . To write the above expression in the Majorana language we follow the exact same steps presented for the K_3' term in Sec.2.3.3, so we get the following form of $\mathcal{H}_{K_3}$

$$\mathcal{H}_{K_3} = iK_3 \sum_{(ijkl)_{\alpha\beta\gamma}} \hat{u}_{ij}^\alpha \hat{u}_{kj}^\beta \hat{u}_{kl}^\gamma c_i c_l. \tag{B.2}$$

A very interesting consequence of the K_3 term is the fact that there are two possible paths for the same hopping, as depicted in Fig. 37(a). These symmetry-related paths give rise to a destructive interference every time we have a flux ($W_p = -1$) passing through a plaquette, as the flux operator depends on the link variables around the plaquette (Eq.(2.15)). Therefore, if we consider the 1-Flux configuration, the spectrum does not depend on the K_3 term. This situation gives rise to a window of K_3 values where the 1-flux sector is energetically favorable in comparison to the zero-flux for the FM Kitaev interaction, as reported in Ref.[105]

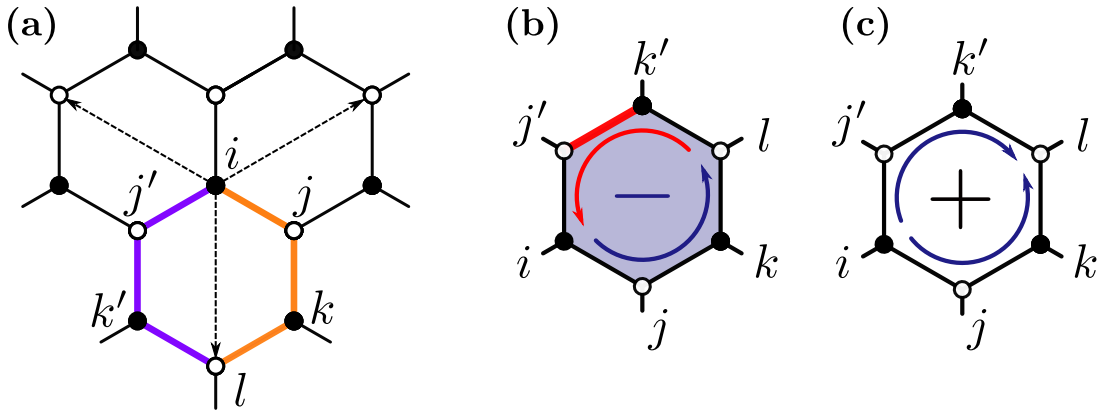

Figure 37 – (a) The structure of the third-neighbor interaction K_3. The arrows indicate the 3 possible neighbors. In orange and purple, we highlight two symmetry-related paths from site i to site l. (b) If a flux is pinned to the hexagon, the two paths cancel each other, and there is no hopping between i and l. (c) For a 0-flux case, there is no sign difference between the paths, so we have a constructive interference pattern from i to l.
Source: By the author.

Surprisingly, there are no results in the current literature regarding the flux transitions for the extended Kitaev model in Eq.(2.51) for the AFM case. Therefore, we give a

simple variational argument to account for the flux transitions in this case, considering the K_3' and K_3 terms independently. Instead of checking the energy for all the flux configurations in a Monte-Carlo simulation, we simply compute the ground-state energy for the two opposite limits of the 0-flux and 1-flux. Because these are ordered flux configurations, we can calculate the energy exactly, and the results are displayed in Fig.38.

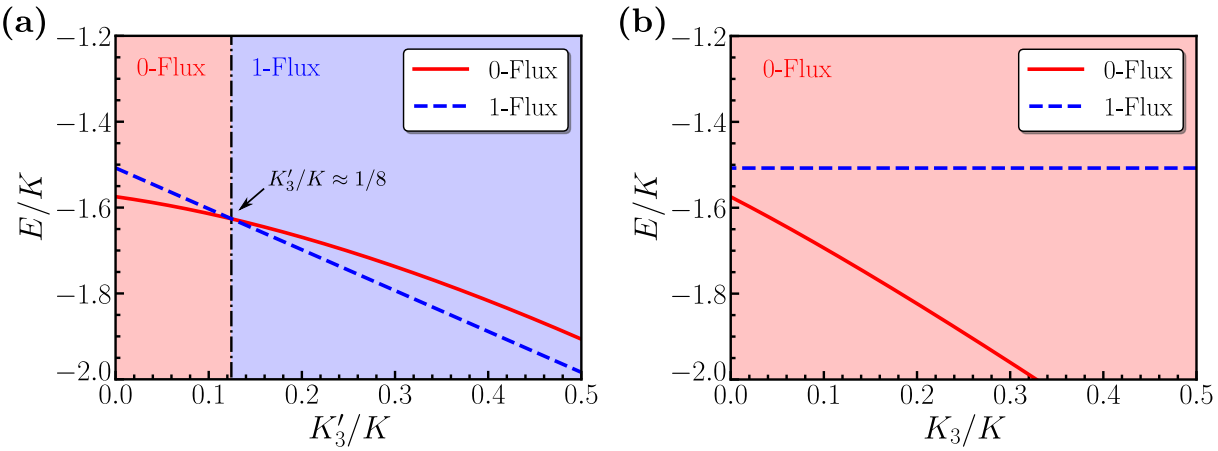

Figure 38 – The ground state energy as a function of K_3'(a) and K_3(b) for the 0-flux and 1-flux. In (a), we see a transition between the flux sectors for $K_3' \gtrsim K/8$, while in (b) the ground-state remains in the 0-flux sector for all values of K_3. Notice that the 1-flux energy does not change as a function of K_3, due to the destructive interference pattern of hoppings.
Source: By the author.

For the K_3' case, we see a transition around $K_3' \gtrsim K/8$, where the 1-flux sector becomes energetically favorable. On the other hand, we find no transition between the fluxes for the K_3 term alone, and the 0-flux is the true ground-state for all ranges of K_3 values. We point out again that this is a rather simplified analysis, and the true ground-state configuration must be checked via a Monte-Carlo sampling. Notwithstanding, we still expect these results to be true for very small values of K_3 and K_3',

APPENDIX C – THE ADIABATIC APPROXIMATION

In this appendix, we give further details on the adiabatic approximation employed in the dynamical spin structure factor calculations in Sec.3.2.2.

Our starting point is the structure factor, which is given by the following expression:

$$S(\mathbf{q},\omega) = \frac{1}{N}\sum_{i,j}\sum_{\alpha,\beta} e^{-i\mathbf{q}(\mathbf{r}_i-\mathbf{r}_j)} \int_{-\infty}^{\infty} dt e^{i\omega t} \left\langle \sigma_i^{\alpha}(t)\sigma_j^{\beta}(0)\right\rangle , \tag{C.1}$$

where the expected value inside the integral is the usual spin-spin correlation function. As discussed in Sec. 2.1.2, this calculation involves the creation of a flux pair, which changes the Majoranas time evolution. Following Refs.,[64,66] this can be translated into a local quantum quench problem for Majorana fermions. This is explicitly written in terms of an effective potential V_α which is responsible to flip a bond α in the unit cell i. Using the Majorana representation, one can find the following form for the spin correlator:[65]

$$S_{ij}^{\alpha\beta}(t) = \langle M_0|\, e^{iH_0 t} c_i\, e^{-i(H_0+V_\alpha)t} c_j\, |M_0\rangle \;\; \delta_{\alpha\beta}\delta_{\langle ij\rangle_\alpha}, \tag{C.2}$$

where H_0 is the Hamiltonian for the system without fluxes, $H_0 + V_\alpha$ is the perturbed Hamiltonian (with a flux pair), and $|M_0\rangle$ is the ground state of the Majorana system. Here we already take into account the flux selection rules, so we restrict the correlator up to NN with the condition $\delta_{\alpha\beta}\delta_{\langle ij\rangle_\alpha}$. Using the translational invariance of the 0-Flux sector, we can see that there are only 4 distinct correlators, two on-site diagonal terms: $S_{AA}^{\alpha\alpha}$, $S_{BB}^{\alpha\alpha}$, and two NN terms: $S_{AB}^{\alpha\alpha}$, $S_{BA}^{\alpha\alpha}$. Following Knolle *et al.*[65] we use the notation $c_{\mu,\mathbf{r}}$ to indicate the majorana operator at the sublattice $\mu = A, B$ on the unit cell $\mathbf{r}$, which is choosen to be $\mathbf{r} = 0$, without loss of generality.

As a first step to calculate Eq.(C.2) it is intructive to look at the Lehmann representation[58] of $S_{ij}^{\alpha\alpha}(t)$. Here we introduce $\{|\tilde{\lambda}\rangle\}$ as the complete basis of many-body eigenstates of the perturbed Hamiltonian $H_\alpha = H_0 + V_\alpha$. By inserting the identity $\sum_{\tilde{\lambda}} |\tilde{\lambda}\rangle\langle\tilde{\lambda}| = \mathbb{1}$ we have the following form for the $S_{AB}^{\alpha\beta}(t)$ term:

$$S_{A0B0}^{\alpha\alpha}(t) = -i\sum_{\tilde{\lambda}} e^{it(E_0-E_{\tilde{\lambda}}^F)} \langle M_0|\, c_{A,0}|\tilde{\lambda}\rangle\langle\tilde{\lambda}|c_{B,0}\, |M_0\rangle\, , \tag{C.3}$$

where $E_{\tilde{\lambda}}^F$ are the many-body eigenenergies corresponding to the perturbed Hamiltonian. By taking the Fourier transform of the above expression, we have:

$$S_{A0B0}^{\alpha\alpha}(\omega) = -2\pi i\sum_{\tilde{\lambda}} \langle M_0|\, c_{A,0}|\tilde{\lambda}\rangle\langle\tilde{\lambda}|c_{B,0}\, |M_0\rangle\, \delta\left(\omega - (E_0 - E_{\tilde{\lambda}}^F)\right) \tag{C.4}$$

From this equation we can calculate the contribution coming from different number of particles. The zero excitation is just the ground state $|M_F\rangle$ for the flipped bond sector,

with energy E_0^F. The single particle excitation is written as $|\lambda\rangle = b_\lambda^\dagger |M_F\rangle$, with energy $E_\lambda^F = E_\lambda^F$. For two particle excitations we have $|\lambda, \lambda'\rangle = b_\lambda^\dagger b_{\lambda'}^\dagger |M_F\rangle$ with $E_{\tilde{\lambda}} = E_\lambda^F + E_{\lambda'}^F$, and so on.

The procedure up to this point is quite general, and although one can calculate explicitly the few-particle contributions, this operation is a bit cumbersome in our numerical calculations, as we have to write the flipped bond ground state $|M_F\rangle$ in terms of our original ground state, $|M_0\rangle$. To avoid these overlap calculations, we consider a situation where the potential V_α is switched on and off *adiabatically*, rather than a quantum quench. In this situation one can show that the $S_{AB}^{\alpha\beta}(t)$ term from (C.2) acquires the more simplified form:[65]

$$S_{A0B0}^{\alpha\alpha,\mathrm{ad}}(t) = -ie^{iE_0 t} \langle M_F| c_i \, e^{-i(H_0+V_\alpha)t} c_j |M_F\rangle . \tag{C.5}$$

This expression is simpler to work with because we now have $|M_F\rangle$ in place of $|M_0\rangle$. Therefore the Lehmann representation for a single excitation is now:

$$S_{A0B0}^{\alpha\alpha,\mathrm{ad}}(\omega) = -2\pi i \sum_\lambda \langle M_F| c_{A,0} b_\lambda^\dagger |M_F\rangle \langle M_F| b_\lambda c_{B,0} |M_F\rangle \, \delta\left(\omega - \Delta_{2f} - E_\lambda^F\right) \tag{C.6}$$

where $\Delta_{2f} \equiv E_0 - E_0^F$ is the pair flux gap. Our work now is reduced to calculate the matrix elements $\langle M_F| c_{A,0} b_\lambda^\dagger |M_F\rangle$ and $\langle M_F| b_\lambda c_{B,0} |M_F\rangle$. Using the complex fermions in (2.5) along with the Bogoliubov transformation in Eq. (3.7), we can write the majorana operators in terms of the operators b and $b^\dagger$:

$$c_{A,0} = \sum_k (X_{0k}^T + Y_{0k}^T) b_k + (X_{0k}^\dagger + Y_{0k}^\dagger) b_k^\dagger \tag{C.7}$$

$$c_{B,0} = i \sum_k (Y_{0k}^T - X_{0k}^T) b_k + (X_{0k}^\dagger - Y_{0k}^\dagger) b_k^\dagger \tag{C.8}$$

Using the above expressions, the first matrix element in Eq.(C.6) is now written as

$$\langle M_F| c_{A,0} \, b_\lambda^\dagger |M_F\rangle = \sum_k (X_{0k}^T + Y_{0k}^T) \langle M_F| b_k b_\lambda^\dagger |M_F\rangle \tag{C.9}$$

$$= (X_{\lambda 0} + Y_{\lambda 0}) \tag{C.10}$$

In the same way, we have the following expression for the second expected value in Eq.(C.6):

$$\langle M_F| b_\lambda c_{B,0} |M_F\rangle = \sum_k (X_{0k}^\dagger - Y_{0k}^\dagger) \langle M_F| b_\lambda b_k^\dagger |M_F\rangle \tag{C.11}$$

$$= (X_{\lambda 0}^* - Y_{\lambda 0}^*) \tag{C.12}$$

Using these results, the expression in Eq.(C.6) is finally reduced to

$$S_{A0B0}^{\alpha\alpha}(\omega) = 2\pi \sum_\lambda (X_{\lambda 0} + Y_{\lambda 0})(X_{\lambda 0}^* - Y_{\lambda 0}^*) \, \delta\left(\omega - \Delta_{2f} - E_\lambda^F\right) \tag{C.13}$$

In order to write the $\mathbf{q} = 0$ component of the spin structure factor, we must consider the other contributions, $S^{\alpha\alpha}_{AA}$, $S^{\alpha\alpha}_{BB}$ and $S^{\alpha\alpha}_{BA}$. These can be computed with the same procedure, leading to the following expressions:

$$S^{\alpha\alpha}_{A0A0}(\omega) = 2\pi \sum_{\lambda} (X_{\lambda 0} + Y_{\lambda 0})(X^*_{\lambda 0} + Y^*_{\lambda 0})\, \delta\left(\omega - \Delta_{2f} - E^F_\lambda\right) \tag{C.14}$$

$$S^{\alpha\alpha}_{B0B0}(\omega) = 2\pi \sum_{\lambda} (X_{\lambda 0} - Y_{\lambda 0})(X^*_{\lambda 0} - Y^*_{\lambda 0})\, \delta\left(\omega - \Delta_{2f} - E^F_\lambda\right) \tag{C.15}$$

$$S^{\alpha\alpha}_{B0A0}(\omega) = 2\pi \sum_{\lambda} (X_{\lambda 0} - Y_{\lambda 0})(X^*_{\lambda 0} + Y^*_{\lambda 0})\, \delta\left(\omega - \Delta_{2f} - E^F_\lambda\right) \tag{C.16}$$

Finally, by adding all contributions, all the crossed terms cancels out, along with the contributions proportional to $|Y_{\lambda 0}|^2$. The only remaining contributions are the $|X_{\lambda 0}|^2$ terms, so we can write the final expression of the spin structure factor as:

$$S^{\alpha\alpha}(\mathbf{q} = 0, \omega) = 8\pi \sum_{\lambda} |X_{\lambda 0}|^2 \delta\left(\omega - \Delta_{2f} - E^F_\lambda\right). \tag{C.17}$$

This expression can be easily generalized at finite temperature, as presented in Eq.(3.16). As a final note, we drop the 8π normalization, for the sake of simplicity.

APPENDIX D – DETAILS ON THE POWER LAW EXTRACTION

A key result of the current work is the presence of a power-law DOS at low-energies. To extract the power-law exponent, we employ two complementary methods. First, we plot the curves $\rho(E) \sim E^{-\alpha}$ on a log-log scale and get α as the slope of the linear regression to the DOS curve. As an alternative approach, we extract α directly from the spectrum.[160]

We assume that the energy histogram, DOS, displays a power-law form in the interval $0 < E < E_{\max}$, with $E_{\max}$ the upper cutoff energy below which the power-law holds. Given a data set containing $N_{\rm ob}$ observations $E \leq E_{\max}$, we would like to know the value of α for the power-law model that is most likely to have generated this data:[160]

$$\alpha = 1 - \left\langle \ln\left(\frac{E_{\max}}{E}\right)\right\rangle^{-1}_{E\leq E_{\max}}, \tag{D.1}$$

with the statistical error given by $\sigma_\alpha = \alpha/\sqrt{N_{\rm ob}}$. However, the greatest source of uncertainty is the definition of $E_{\max}$. A simple way to find its optimal value is to plot $\alpha \times E_{\max}$, picking $E_{\max}$ within an energy range where α is reasonably stable.

This method has proved to be quite satisfactory for our data. As an example, we show the exponent extraction for the random-flux sector with bond disorder, Fig.39(a). The values of α obtained from Eq. (D.1) fit well the DOS at low energy as shown in Fig. 39(b).

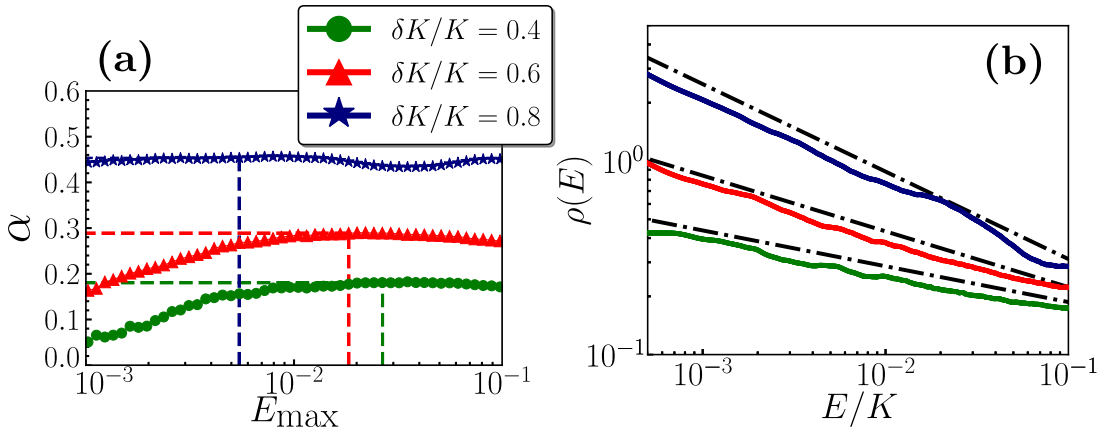

Figure 39 – (a) Power-law exponent α as function of the upper cutoff energy below which the power-law holds $E_{\max}$. We consider the random-flux sector and bond disorder with $\kappa = K_3' = 0$. The dashed lines indicate the optimal values of α and $E_{\max}$. (b) DOS in a log-log scale at low energies. The dot-dashed lines are power-law fits, $\rho(E) \sim E^{-\alpha}$, to the data with the exponent α extracted in (a). The fits are shifted with respect to the DOS curves for the sake of clarity. We considered $L = 30$ and 3×10^3 realizations of disorder.

Source: By the author.